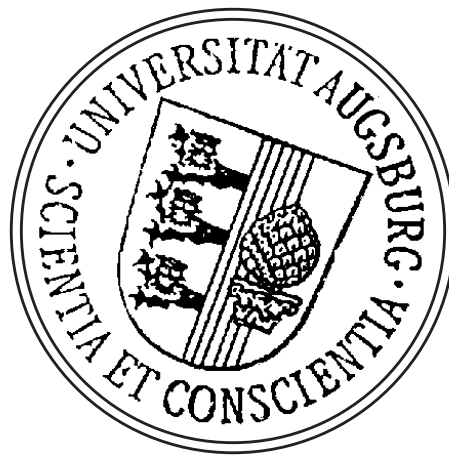


Polymeric hole injection layers for Perovskite-based Light-Emitting Diodes

**Thesis Prepared for the Degree:
Master of Science
in
Physics**

Tassilo Naujoks

Augsburg, October 26th 2018



Erstprüfer: Prof. Dr. Wolfgang Brütting
Zweitprüfer: Prof. Dr. Henning Höppe

“Software is like sex: it’s better when it’s free.”

— *Linus Torvalds*

Contents

1	Introduction	3
2	Basic Principles of Organic Light-Emitting Diodes	4
2.1	Setup and Principles	4
2.2	External Quantum Efficiency (EQE)	7
3	Application of Perovskites as Emitter in Organic Light-Emitting Diodes	8
3.1	Properties of Perovskites	8
3.2	Hole transporting Polymers	11
3.3	Quantum Dots	12
4	Materials and Sample Preparation Procedure	13
4.1	Materials	13
4.1.1	Perovskites	13
4.1.2	Polymers	14
4.1.3	Alternate (evaporated) hole transporting materials	16
4.1.4	Alternative emitters	18
4.1.5	Electron transport materials	18
4.2	Stack Design	20
4.3	Fabrication Process	21
5	Methods of Characterisation	24
5.1	Profilometry	24
5.2	Atomic Force Microscopy (AFM)	25
5.3	Scanning Electron Microscopy (SEM)	26
5.4	Electrical and Optical Characterisation of OLEDs	27
5.4.1	j-V-L Characteristic curve	27
5.4.2	Emission Spectra	27
5.4.3	Estimation of the External Quantum Efficiency (EQE)	29
6	Experimental Results	32
6.1	Polymeric Hole Injection Layers	32
6.1.1	Polymer-film properties	32
6.1.2	Performance in OLEDs	36
6.2	Methylammonium lead iodide-, (MA)PbI ₃ -perovskite	42
6.2.1	Properties of (MA)PbI ₃ -films	42
6.2.2	Properties of (MA)PbI ₃ -based LEDs	46

6.3	Caesium lead bromide-, CsPbBr ₃ -perovskite based quantum dots	48
6.3.1	Properties of CsPbBr ₃ -films	48
6.3.2	Properties of CsPbBr ₃ -based LEDs	51
7	Outlook and Summary	59
8	Appendix	61
8.1	Additional Figures	61
8.2	Photometric Calculations	69
8.2.1	Calibration of the Photodiode	69
8.2.2	Photo-current to Lumen Dependence	69
8.2.3	Luminous Flux to Luminance Dependence	70
8.2.4	Radiance from Energy Distribution and Spectral Radiance	71
8.2.5	Calculation for the present OLED-Measurement-Box	72
8.2.6	Estimation of Errors	72
8.2.7	Wavelength to Energy Scale Conversion	75
9	References	77
10	Software References	85

1 Introduction

In recent years, organic light emitting diodes (OLEDs) have emerged in the consumer market. They impressed with their vibrant colours, so that many modern smartphones and television displays are based on OLEDs. While efficiencies are as high as the inorganic counterparts, the lifetimes of OLEDs are still not as long. However, since the electronic consumer market is evolving very rapidly, leading to electronic devices being replaced by newer ones frequently, the lifetimes are no longer the main concern of the industry. In order to maximise the profits, a reduction of production cost is focused by manufacturing companies. A very energy efficient way to create OLEDs is to deposit layers from solutions. With appropriate solutions, printable OLEDs are thinkable and currently researched. Printing LEDs will reduce production costs, as well as environmental costs, tremendously. This arises by the circumstance, that the printing process is a deposition procedure where nearly no material is wasted. Additionally, the deposition takes place under ambient pressure and temperature, so that energy thirsty vacuum or heater systems are avoided. In order to create solution-processed OLEDs, the materials which are typically evaporated have to be replaced. Therefore, there are new challenges arising: Evaporated layers can be combined in a sequence, determined by the materials properties (e.g. energy levels, film growth properties). When depositing solution-processed: the solution-processed layers may dissolve other layers during deposition, which is an additional property to consider. One way to avoid this dissolution of layers is using polymers, which become insoluble when deposited.

The poly-TPD is such a polymeric material. This polymer is characterised in this thesis; its issues and its opportunities are discussed. Solution-processed emitting layers are tested as overlying layers. Very promising candidates for such emitting materials are the trihalide perovskites. The application of such materials in LEDs is just recently discovered. With high internal quantum efficiencies, and narrow emission bands, the perovskite emitters are promising for application in displays to get an even broader colour range, while still having high efficiencies.¹ The perovskites show their own challenges upon incorporation into an OLED stack. In this thesis two different perovskite based LEDs are shown. The concept of light emission by a perovskite in an OLED stack is examined. The efficiencies of these LEDs with different deposition strategies are measured and compared. Therefore the arising issues are investigated and approaches of an efficiency increase are held out in prospect.

2 Basic Principles of Organic Light-Emitting Diodes

This section will give an insight on basic processes and properties of organic light-emitting diodes, that are necessary for understanding the challenges and chances that arise, when creating perovskite based LEDs. Initially, a brief overview over the setup and the working principles of an organic light emitting diode (OLED) will be given. At that, an important quantity to benchmark its performance, the external quantum efficiency (EQE) will be introduced.

An OLED is a diode, where focus lies on the emission of photons by an all-organic thin film system. The advantages of thin film physics, as well as the density of states distribution of organic materials, has led to a common OLED setup. This setup and its principles will be explained in this section, before modifying the setup to apply new, alien materials such as perovskites. Note that this section is a short introduction based on references 2–4. For further information refer to these documents.

2.1 Setup and Principles

The most straightforward OLED consists of an anode, a cathode and an organic layer in-between. One of the electrodes has to be transparent, because through this layer the light will leave the device. The emitted photons are generated in the organic layer. For easier understanding, the concept of holes, known from inorganic semiconductors, is used to describe processes in organic ones as well. A hole is a imagined particle, which represents the properties of a lack of electron in valenceband or its highest-occupied-molecular-orbital state (HOMO). It behaves just like a electron, but with a positive charge and effective mass. Hence, the anode is not considered to be only electron attracting, but also hole delivering. As shown in Fig. 1, the holes are injected from the anode into the organic layer's valence band, respectively its HOMO. Analogously for the cathode, where electrons are injected into the conduction band, respectively its lowest-unoccupied-molecular-orbital state (LUMO). Consequently, the organic semiconductor fills with charge carriers. Due to electrostatic attraction of the both oppositely charged carriers, a bound state between electron-hole pairs can be formed, which is called an exciton. This exciton is not stable, and will spontaneously decay, that is, the charge carriers will recombine with the emission of its energy, that arises from the attractive coulomb force between hole and electron. With a suitable choice of material the exciton's energy is in the energy range of visible photons and consequently visible light can be emitted. However, as exciton lifetimes increase, the probability for it to diffuse to one of the electrodes increases too. The electrodes, with their

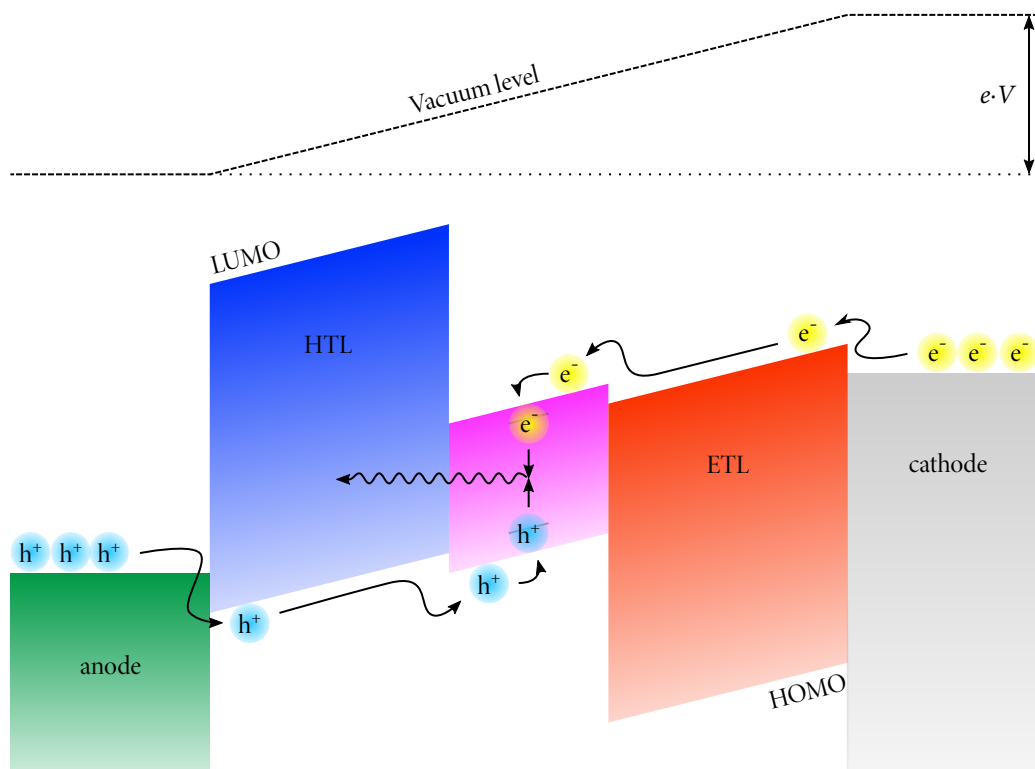


Figure 1: Simplified illustration of processes, leading to light emission, in OLEDs.^{S.1}

high density of states, provide decay paths, which result in a thermal recombination. The single carriers can also reach the opposite electrode without forming excitons. In order to prevent such quenching processes, two charge carrier blocking layers are added to the very basic OLED design (see Fig. 1). These layer's LUMO, in case of the electron transport layer (ETL), for letting electrons pass, respectively HOMO, in case of hole transport layer (HTL), for letting holes pass, have to match neighbouring layers.

The charge carrier injection into organics is mostly a thermionic emission process. So the conductivity decreases exponentially with the energy gap between the molecular orbital states (LUMO/CBM^a resp. HOMO/VBM^b or workfunction). To bridge high energy differences, a cascade of layers may be used. At the same time, for blocking holes the HOMO of the layer has to be very deep, so that for holes to get into this layer a huge amount of energy is required. Accordingly, the LUMO of the electron blocking layer has to be very high, making it improbable for electrons to get injected. There is one blocking layer for

^aCBM: Conduction Band Minimum

^bVBM: Valence Band Maximum

each charge carrier, so that ideally the same amount of electrons and holes are accumulated in the emitting layer. In that case the charge carrier balance is optimal, which is an important factor, determining the External Quantum Efficiency (EQE), which will be introduced in the next section.

2.2 External Quantum Efficiency (EQE)

$$\eta_{\text{EQE}} = \underbrace{\gamma \cdot \eta_{\text{rad}} \cdot q_{\text{eff}}}_{\eta_{\text{int}}} \cdot \eta_{\text{out}} \quad (1)$$

Charge Carrier Balance: γ The first factor, γ , is the just mentioned charge carrier balance, which is defined by the ratio of formed excitons per injected charge carriers. A value of 1 is the optimal case. At that, the all injected charge carriers form excitons. If $\gamma < 1$, then one or both charge carriers reach the respective target electrode without forming excitons.

Radiative Exciton Fraction: η_{rad} The second factor η_{rad} represents the radiative exciton fraction. Due to quantum-mechanical properties of a photon, for systems based on fluorescent emitter materials it takes the value $\frac{1}{4}$, because only the singlet state of an exciton can decay radiatively. But there are several processes which allows to access the three residual triplet states, so that a value of 1 is thinkable. Radiation enabled by the triplet state is called phosphorescence, since its emission is usually time delayed compared to the fluorescence. In many heavy metal ions the strong spin-orbit coupling ensures a radiative exciton fraction near unity.

Radiative Quantum Efficiency (RQE): q_{eff} The third factor, q_{eff} , also known as the radiative quantum efficiency, is defined by the ratio of radiative decaying per non-radiative decaying excitons. The excitons may quench without emitting visible photons, that is, recombine through various interactions or at impurities. For very pure and well designed materials and stacks, this factor can also be approached to unity. So overall the internal quantum efficiency, η_{int} , can be optimal, but the external quantum efficiency has a theoretical threshold:

Optical Outcoupling Efficiency: η_{out} The fourth factor, η_{out} , the optical outcoupling efficiency, is limited by optical properties of the system's layers. Photons may quench with surface plasmons on metallic cathodes, they may be caged inside wave-guided modes between layers or by total reflection of the substrate. For bottom-emitting devices, used for experiments in this work, this factor is around 15 - 20 %. By tuning the emission orientation the theoretical maximum is estimated around 40 %.^{4,5} So for high efficiencies, new materials with a preferred orientation and a high internal quantum yield are needed. Such material could be of perovskite structure.

3 Application of Perovskites as Emitter in Organic Light-Emitting Diodes

This section will explain the opportunities and challenges of the application of perovskite structured materials as emitter in OLEDs. At first, the materials are introduced and described in detail regarding structural, optical and electrical properties. At that, the need of special hole injection layers will become clear. This thesis focuses on specific polymers, which will be showed consequently. Finally, the concept of quantum dots and its application for perovskites are briefly shown.

3.1 Properties of Perovskites

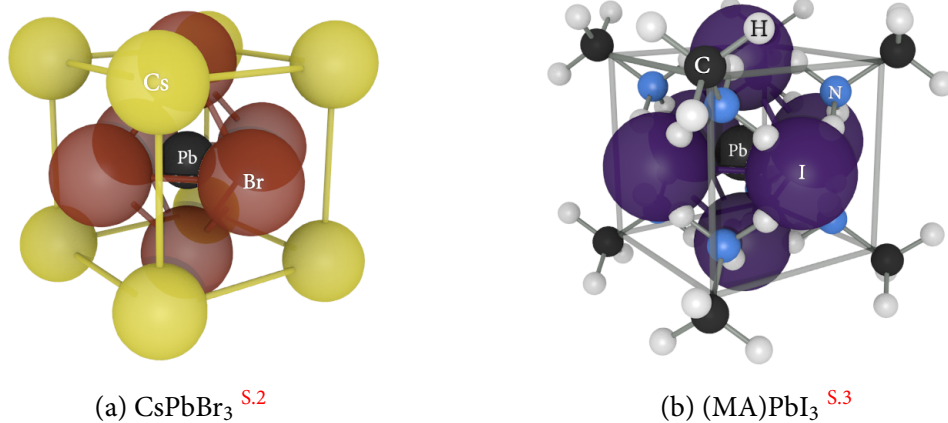


Figure 2: Crystal structure of the considered perovskites.

Perovskite is the retained name for the mineral with the chemical formula: CaTiO_3 . However when speaking of the plural, perovskites, it is referred to materials with the same crystal structure as the perovskite. For example, the first high temperature super conductive material $\text{La}_{5-x}\text{Ba}_x\text{Cu}_5\text{O}_{5(3-y)}$, discovered 1986 by J. G. Bednorz and K. A. Müller, had a perovskite structure.⁶ The related crystal structure system is orthorhombic (bipyramidal) or cubic (hexoctahedral), depending on the ions sizes. The base of such a perovskite structure has the stoichiometry: ABX_3 , where A has to be a big cation, B a smaller cation and X is a appropriate anion. In Fig 2a the cubic perovskite structure is shown. Cs, Pb and Br are representing the respective ions A, B and X. Most perovskites are in orthorhombic

state due to distortions caused by mismatching ions sizes. A tolerance factor t , to measure the extent of these deviations at room temperature was introduced by Goldschmidt⁷:

$$t = \frac{r_A + r_X}{\sqrt{2} \cdot (r_B + r_X)}. \quad (2)$$

The empirical radius of the respective ion is denoted by r_{\square} , where $\square = A, B$ or X . For example, for the perovskite shown in Fig 2a the radii are $r_{Cs} = 181$ pm, $r_{Pb} = 133$ pm and $r_{Br} = 182$ pm.⁸ Resulting in a tolerance factor of approximately 0.81. An ideal cubic perovskite yields a tolerance factor of 1. Yet the orthorhombic perovskite structure at room temperature is maintained for tolerance factors as low as 0.75.⁷

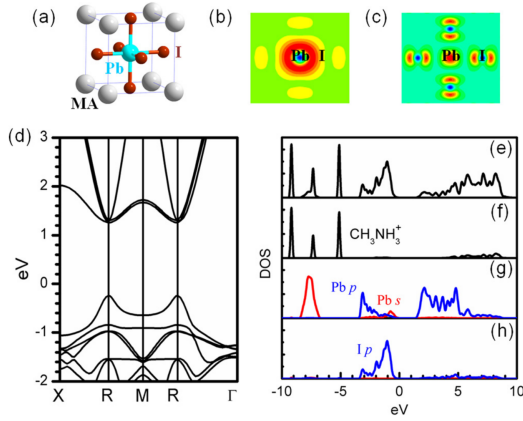


Figure 3: (a): Structure of a (MA)PbI₃-perovskite. (b): Partial charge density at CBM and (c): VBM. (d): Band structure of the (MA)PbI₃ crystal. Density of states of (e): the whole (MA)PbI₃ crystal, (f): MA⁺ (partially), (g): Pb²⁺, (h): I⁻. The scales have been adjusted for better illustration; 0 eV is normalised to be the VBM.⁹ ((b)-(h) Determined with VASP code¹⁰)

Electrical Properties The application of a material class as a superconductor suggests some unique and interesting electrical properties, even at room temperature. Figure 3 shows the density of states distribution of (MA)PbI₃^a as an exemplary perovskite (depicted in Fig. 2b). The charge density at the conduction band minimum (CBM), that is the analogon to the LUMO, is located in proximity of the lead ion (see Fig. 3 (b)). Figure 3 (g) implies that the CBM is built from lead's 6 p orbitals. On the other side, the valence band maximum (VBM), that is the analogon to the HOMO, is distributed between the halogen ions in dumbbell-shape, and in the centre of the lead ions. So the VBM consists mostly of the halogen's p orbitals and the lead's 4 s orbitals.¹¹

Figure 3 (d) shows the band structure of such perovskites. At the R point, there is a direct bandgap. A direct bandgap is a feature where the VBM and the CBM are vertically aligned at the same wavevector (\vec{k}). When comparing with other direct bandgap semiconductors like for example GaAs: It is remarkable, that the curvature, that is, the dispersion of electrons and the dispersion of holes are about equal in the perovskites.¹² Therefore the effective masses m_e^* , m_h^* are, with $\frac{\partial^2 E}{\partial k^2} = \frac{\hbar}{m^*}$, approximately equal, too. Furthermore, when

^aMA: Methylammonium

considering a drude-like conductivity, with $\mu = \frac{e\tau}{m^*}$, the mobility for holes and electrons are about equal as well. An ambipolar conductivity is of high interest for solar cells, since both carriers have to be extracted equally. For the application in solar cells the material should have a high absorbance as well.

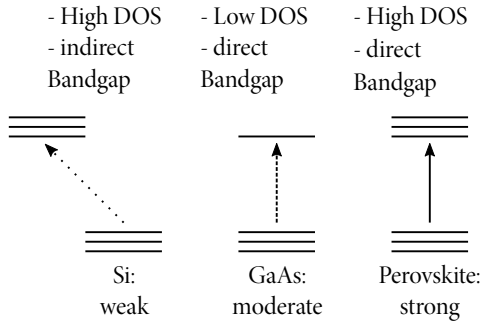


Figure 4: Sketch to illustrate the difference in absorption between different types of semiconductors. The silicon has a weak absorption, because the indirect bandgap is a major disadvantage, which is indicated by the horizontal offset of the states. The GaAs does have a direct bandgap; still the density of states (DOS) in the conduction band is relatively low. The perovskite combines a direct bandgap with high DOS in valence and conduction band.^{13, S.4}

Optical Properties As a matter of fact, perovskites absorb photons quite well. Due to their electronic structure they even exceed the absorption capabilities of GaAs.¹³ Figure 4 illustrates, how the absorption is correlated to the band structure and the density of states (DOS) of the material. For instance, silicon, used in solar cells, has to be deposited in rather thick layers. The reason for the weak absorption of silicon is undoubtedly its indirect bandgap.¹⁴ The absorption and emission of photons results in a negligibly small momentum change of the related electron, because of the low momentum of a photon ($\vec{p} = \hbar\vec{k}$). Then, the wavevector should be about constant during a transition. For an indirect bandgap transition, the momentum change has to be compensated via interaction with the environment e.g. nearby particles. The occurrence of two processes at once renders the whole procedure rather improbable.¹³ So the optical transition between these states is improbable as well.

For GaAs the transition is allowed as a single-process procedure. Though, the conduction band of GaAs has a rather low DOS around the CBM compared to the perovskites. With that, the transition probability in semiconductors is determined by two factors: the transition dipole matrix and the joint density of states (JDOS). The first returns the probability for a state transition to occur and the latter gives the multiplicity of the respective transition, that is, combination of states in VBM and CBM. So overall, the optical transition in perovskites is even more probable than in semiconductors like GaAs.¹³

A good transition rate is also very favourable for OLEDs, as it is an important factor controlling the RQE. When considering the EQE, the assumed ambipolarity is not that relevant for charge carrier balance, since emission layers in OLEDs are usually very thin in

order to optimise the optical outcoupling.

However, the radiative exciton fraction is not yet considered for perovskites. Actually, the singlet states of perovskites are optically passive; there is a vanishing probability for a optical transition to the groundstate. That is rather counter-intuitive, but as Becker et al. showed in reference 11, the three triplet states are optically active. The group showed, that in CsPbBr₃-perovskites the total angular momentum is only changed during a triplet to groundstate transition, while the singlet to groundstate transition yields no total angular momentum change. Still, as the photon has a total angular momentum the emission of one has also to involve a momentum change of the material. So on the first guess, η_{rad} would be $\frac{3}{4}$, because three out of four states are optically active. Nevertheless, the singlet state has higher energy and that's why an intersystem-crossing process to an triplet state is easily achieved. As a consequence, similar to a thermally activated delayed fluorescence process this "delayed" emission will increase this factor up to 1, since finally all the excitons are accessible for radiative decay. Having an actual allowed triplet to groundstate transition, results in very low exciton lifetimes (nanoseconds).¹¹ Along with photoluminescence quantum yields near unity (CsPbBr₃ quantum dots incorporated in a PMMA layer, measured at a temperature of 5 K), the exciton lifetimes can be directly related to the radiative lifetimes.¹¹ Low radiative lifetimes are good for application in displays with high image-buildup frequencies.

The exchange of the halides in the perovskites stoichiometry, leads to a emission colour change. This property is very convenient, since it allows a colour tuning, of the resulting LED. When exchanging upwards the periodic table, that is, from iodine via bromide to chloride, a blue shift in photoluminescent emission has been observed by several groups (published in Ref. 1, 11, 13, 15).

3.2 Hole transporting Polymers

To make use of the outstanding properties of the perovskites in solar cell- and light-emitting devices, the materials have to be applied appropriately. Since the optical properties of the perovskites are the most interesting for OLEDs, they are promising candidates for the application as emission layer. The emissive layer is sandwiched between two charge carrier transport layers. The HOMO of the hole transporting layer (HTL) has to be adapted to the VBM of the perovskite and accordingly the LUMO of the electron transporting layer (ETL) has to match the CBM of the perovskite. Another challenge is the deposition of a thin film onto the HTL or ETL. Perovskites can be crystallised from solution directly onto the the respective layer. Still, the solution at least partly dissolves the layers beneath in many cases. So one of the charge carrier transport layers should be solid, resistant to solvents used for the perovskites, and have the right HOMO level, while having a high LUMO to block electrons.

There is a variety of polymers which are, when cross-linked accordingly, solid and have potential to be resistant to many solvents. The polymers are processed from solution as

well. After deposition the respective polymers are hardened. This process can be done thermally, where the chemical groups of the polymers build new bonds between its own chains, making it insoluble in its original solvent.¹⁶

When creating bottom emitter devices, the polymers are used as hole transporting layer. But, there are restrictions to the polymers concerning its conductivity. The structure of an OLED is built by for example the indium tin oxide (ITO) anode and the metallic cathode. So if the polymer is well conductive, a non-negligible current can reach the opposite electrode via in plane paths. On the other side, a badly conductive polymer decreases the current and consequently the light emission.

If the perovskite has a low VBM, a cascade of polymers may be used to bridge the high discrepancy between electrodes workfunction and the perovskite's VBM. The focus of this thesis is on the polymers PEDOT:PSS and poly-TPD, which will be described in detail in section 4.1.2.

3.3 Quantum Dots

For some perovskites, the fabrication is very challenging. Many steps with different temperatures, devices (e.g. centrifuge) and solvents may be necessary. These perovskites can't be synthesised directly on the polymer. So in some cases the perovskites are pre-fabricated and dispersed in a solvent.¹⁷ This solution can then be deposited onto the polymer.

To get sufficiently thin layers or in order to use the quantum-mechanical confinement properties, the sizes of the particles are chosen to be very small, resulting in quantum dots. To avoid surface states and agglomeration or even recrystallisation of the quantum dots, the surface is passivated with ligands. Problematic with these ligands, is the fact, that they are mostly badly conductive, which impairs the injection of charge carriers into the perovskite-quantum dot. When reducing the amount of ligands, the injection of charge carriers is eased, but the chemical stability of the quantum dots decreases.¹⁵

4 Materials and Sample Preparation Procedure

This section will give detailed information about the fabrication of all samples that are referred to in this thesis. An insight on the exact OLED design of the used bottom emitting OLEDs will be given. The used materials will be introduced in detail. Furthermore the deposition techniques will be shown briefly.

4.1 Materials

4.1.1 Perovskites

(MA)PbI₃ (CH₃NH₃PbI₃) methylammonium lead (tri) iodide (see Fig. 2b) is a black¹⁸ perovskite mainly used for solar cells. It shows outstanding features like high exciton diffusion length,^{19, 20} high carrier mobility, while having high absorbance and low trap density.²¹ While exciton diffusion lengths and high absorbances are not key features for building OLEDs, the other properties are promising for light-emitting devices as well. (MA)PbI₃ is expected to yield light in the red visible or near infrared range and having VBM at about -5.3 to -5.5 eV and CBM at about -3.8 to -3.9 eV.²²⁻²⁴ The Goldschmidt's tolerance factor, is not easily applicable, since the methylammonium ion is not spherical. In fact the ammonium ion is only slightly smaller as than the caesium ion.²⁵ So along with the methyl group the MA ion should be bigger than the Cs ion and the iodine ion is also bigger than the bromide ion. So when considering Eq. 2, the formation of a perovskite is at least plausible. Nevertheless, a perovskite formation can be easily validated, due to its black colour. An issue with this perovskite is its stability: It is highly susceptible to water and there is an irreversible migration of iodine ions.^{26, 27}

CsPbBr₃ Caesium lead (tri) bromide (see Fig. 2a) is a perovskite with better thermal stability than (MA)PbI₃ though the CsPbBr₃ itself is as susceptible to water.²⁸ On the one hand its compounds are less soluble in common solvents (compared to (MA)PbI₃), which is a major shortcoming for the solution processed film deposition. But on the other hand, this feature can be used for the synthesis of nanocrystals or quantum dots (QDs).²⁹ CsPbBr₃ is expected to emit light in the cyan-green range and having VBM at about -5.9 to -6.2 eV and CBM at about -3.4 to -3.8 eV.^{30, 31} With a stokes shift smaller than 100 meV,³² the light-emission maximum can be estimated around 510 nm. CsPbBr₃ QDs showed photoluminescence quantum yields as high as 90 % in solution,³³ which implies potentially high internal quantum yields in perovskite light emitting diodes (PeLEDs).

4.1.2 Polymers

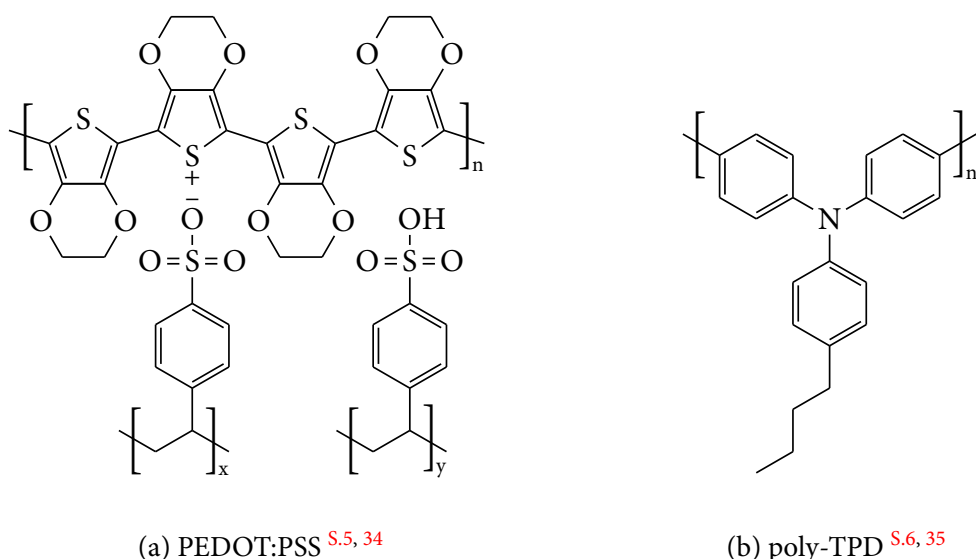


Figure 5: Lewis structure formulae of the polymers used in devices fabricated for this thesis.

PEDOT:PSS poly(3,4-ethylenedioxythiophene)-poly(styrenesulfonate)

(PEDOT:PSS, see Fig. 5a) is a mixed polymer, consisting of two different ionomers. Poly(3,4-ethylenedioxythiophene) (PEDOT) is positively charged and the poly(styrenesulfonate) (PSS) neutralises the charges. However, not every site is positively charged, thus not every PSS is ionised. The respective PSS will be protonised to poly(4-styrenesulfonic acid)(PSSH) (the “y”-denoted polymer in Fig. 5a).³⁴

Furthermore thanks to the sulfonic group the whole polymer is dispersible in water, while showing, when hardened, a tremendously worsened dispersibility. The HOMO level of PEDOT:PSS is around -5.0 eV to -5.2 eV.^{36, 37} Apparently a LUMO is not easy to determine as the density of states distribution does not allow a fixed LUMO (see Fig. A.1).³⁸

A problematic property of the PSS is its acidity, induced by the sulfonate.^{39, 40} This acidity erodes the underlying ITO layer,⁴¹ and it has been shown that there are also major impacts on the overlying layers.⁴² PEDOT:PSS is usually microdispersed in water.

Additionally PEDOT:PSS's susceptibility to solvents is an issue when spin coating on top. Solvents will eventually drastically improve conductivity.⁴³ As PEDOT:PSS is a very well-known polymer for hole injection, there are many different types. On the one hand, the ratio of PEDOT to PSS is altered. When considering Fig. 5a: the hole mobility is ensured by the positive charge on the PEDOT polymer. So an increase of PSS ratio results on a lower concentration of PEDOT strands, thus lowers conductivity. The PEDOT:PSS

PH1000 type, with a PEDOT:PSS ratio of 1:2.5 specifies resistivities that are close to reaching that of metals, that is $\approx 10^{-5} \Omega\text{m}$.³⁶ While other types like AI4083, with a ratio of 1:6, are orders of magnitudes higher, $\approx 5 - 50 \Omega\text{m}$.³⁶ The most resistive is the CH8000 type with a PEDOT:PSS ratio of 1:20, and a resistivity of $\approx 100 - 3000 \Omega\text{m}$.⁴⁴ On the other hand, there are some solutions where the solvent is not pure water but either with some additives or solved in toluene for improved processability. That is the HIL1.3 or HIL1.3N. The first one is an optimised PEDOT based HIL with medium conductivity (about as high as AI4083), as is the second but additionally the second claims to be pH- neutral.⁴⁵ The PH1000 type has turned out to be completely useless for the proposed OLED design, since the conductivity completely overrides the ITO structure. So the AI4083 and CH8000 types are used for further investigation.

poly-TPD poly[N,N'-bis(4-butylphenyl)-N,N'-bis(phenyl)benzidine]
(poly-TPD, see Fig. 5b) is a polymer where the structure of two repeating units are similar to TPD's^a.³⁵ Therefore similar properties are to expect. The advantage of the polymer is, that it is crosslinkable and after the thermal crosslinking it won't be washed away by most solvents of a solution processed film which may be deposited on top. It has about the same or slightly deeper HOMO at -5.2 eV, and a well defined LUMO at about -2.4 eV compared to PEDOT:PSS.^{46, 47} With the high LUMO, excess electrons from the EML can be blocked quite efficiently. The poly-TPD itself, can be dispersed in chloroform, chlorobenzene or toluol. These solvents are less problematic than water, since any residual water in this layer would cause a fast degradation of the perovskites.

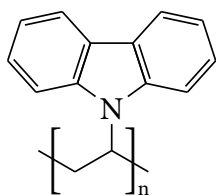
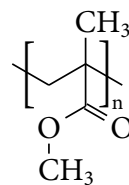
(a) PVK ^{S.7, 48}(b) PMMA ^{S.8, 49}

Figure 6: Lewis structure formulae of the auxiliary polymers used in devices fabricated for this thesis.

PVK Poly(9-vinylcarbazole)⁴⁸

(PVK, see Fig. 6a) is a polymer with deeper HOMO and higher LUMO than poly-TPD, that is -5.8 eV, respectively -2.2 eV. It may facilitate hole injection into perovskites as they have very low VBM levels. It is used to create a HOMO-level-cascade on top of poly-TPD. Additionally it is used as host system for reference devices based on Ir(ppy)₃. Overall it

^a(N,N'-Bis(3-methylphenyl)-N,N'-diphenylbenzidine, see Fig. A.2)

is the corresponding polymer to CBP (see Fig. 8a), since the monomer and therefore the HOMO-LUMO levels are about equal.

PMMA Poly(methyl methacrylate)⁴⁹

(PMMA, see 6b) is a insulating polymer. It is not suitable for carrier injection, since its HOMO (ionisation potential: -10.3 eV) is extremely deep and its LUMO (electron affinity: -0.4 eV) is extremely high.⁵⁰ However it can be used as a spacer, that is, a thin layer to avoid particle diffusion while charge carriers can still travel through by tunnelling.

4.1.3 Alternate (evaporated) hole transporting materials

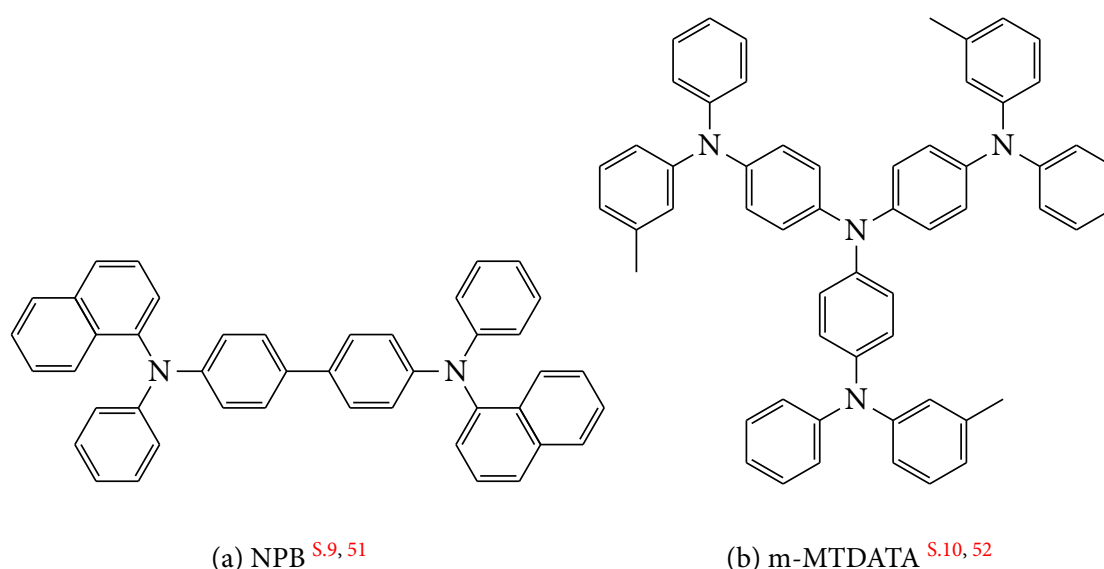
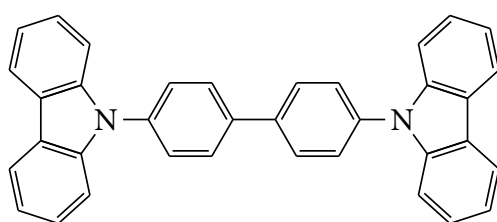


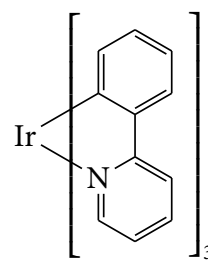
Figure 7: Lewis structure formulae of the additional hole transporting materials used in devices fabricated for this thesis.

In order to compare the polymeric hole injection layers or for creating hole only devices, HTLs are evaporated. NPB (N,N'-Di(1-naphthyl)-N,N'-diphenyl-(1,1'-biphenyl)-4,4'-diamine⁵¹) is used as alternative for poly-TPD since the NPB-Alq₃ devices are well studied at the chair. The HOMO lies at -5.5 eV and the LUMO at -2.4 eV.

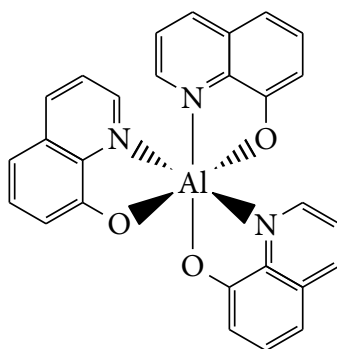
The m-MTDATA (4,4',4''-Tris[phenyl(m-tolyl)amino]triphenylamine⁵²) is used for the hole only devices. The other electrode chosen is gold, to get hole only currents through the device. Thus the m-MTDATA's HOMO is at 5.1 eV matches about the workfunction of gold at 5.3 eV.^{53, 54}



(a) CBP [S.11, 55](#)



(b) Ir(ppy)₃ [S.12, 56](#)



(c) Alq₃ [S.13, 57](#)

Figure 8: Lewis structure formulae of chemicals used as alternatives in emitting layers.

4.1.4 Alternative emitters

For comparison and benchmarking of the polymeric HTLs some alternative well-known emitters have been chosen.

Alq₃^b (in meridional phase⁵⁷, see Fig. 8c), a cheap, widely used and well studied fluorescent emitter, an emitter with radiative exciton fraction of $\frac{1}{4}$, is taken.⁵⁸ It is a metallo-organic complex where the aluminium is bound to three 8-hydroxyquinoline ligands. Its HOMO is located at -5.8 eV and its LUMO at -3.1 eV.⁵⁹ Alq₃ emits green light isotropically with an internal quantum efficiency of approximately 20-32 %.^{60, 61} When considering the maximum outcoupling factor of 20 % (for isotropic emitters),^{62, 63} the maximum EQE of a device based on Alq₃ as emitter should be (considering Eq. 1 and $\gamma = 1: 1 \cdot \frac{1}{4} \cdot 0.2 \cdot 0.32 = 0.016$) less than 1.6 %.

Moreover, Alq₃ is often used as ETL. Though, the use of Alq₃ as ETL has a disadvantage, because its HOMO is rather high, which may lead to a loss of holes. To use an additional hole blocking layer (HBL) is recommended, when using low VBM/HOMO emitters such as the perovskite emitters as shown earlier.

For further benchmarking a phosphorescent emitter with internal quantum efficiency near unity is chosen ($\approx 90\%$). Such is the CBP:Ir(ppy)₃ emitter system (see Fig. 8a and 8b). Ir(ppy)₃^c is also a metallo-organic complex where the iridium atom is bound to three 2-Phenylpyridine ligands. Devices based on this emitter reach EQEs up to 18 % ($= 1 \cdot 1 \cdot 90\% \cdot 20\%$).⁶⁴ CBP^d as the host system has a wide bandgap with a HOMO of -6 eV and a LUMO at -2.9 eV.⁵⁵ The Ir(ppy)₃'s HOMO is at -5.6 eV and its LUMO at -3.0 eV,⁵⁶ so that the Ir(ppy)₃ acts as a trap for excitons on the CBP Host.

4.1.5 Electron transport materials

Different materials are tested as an electron transport material. TPBi^e and BPhen^f (see Fig. 9a and 9b) have higher electron mobilities than Alq₃.^{68, 69} Both have also a lower HOMO, that is -6.2 eV for TPBi and -6.4 eV for BPhen.^{65, 66} The deep HOMO is required for PeLEDs, since the perovskites tend to have low VBMs. Even deeper HOMO is granted by OXD-7^g (see Fig. 9c) with 6.5 eV.⁷⁰ The LUMO is located at -3.0 eV for all mentioned electron transport materials, except TPBi with a higher LUMO of -2.7 eV.

^bTris-(8-hydroxyquinoline)aluminum

^cTris[2-phenylpyridinato-C2,N]iridium(III)

^d4,4'-Bis(N-carbazolyl)-1,1'-biphenyl

^e2,2',2''-(1,3,5-Benzinetriyl)-tris(1-phenyl-1-H-benzimidazole)

^fBathophenanthroline

^g1,3-Bis[5-(4-tert-butylphenyl)-2-[1,3,4]oxadiazolyl]benzene

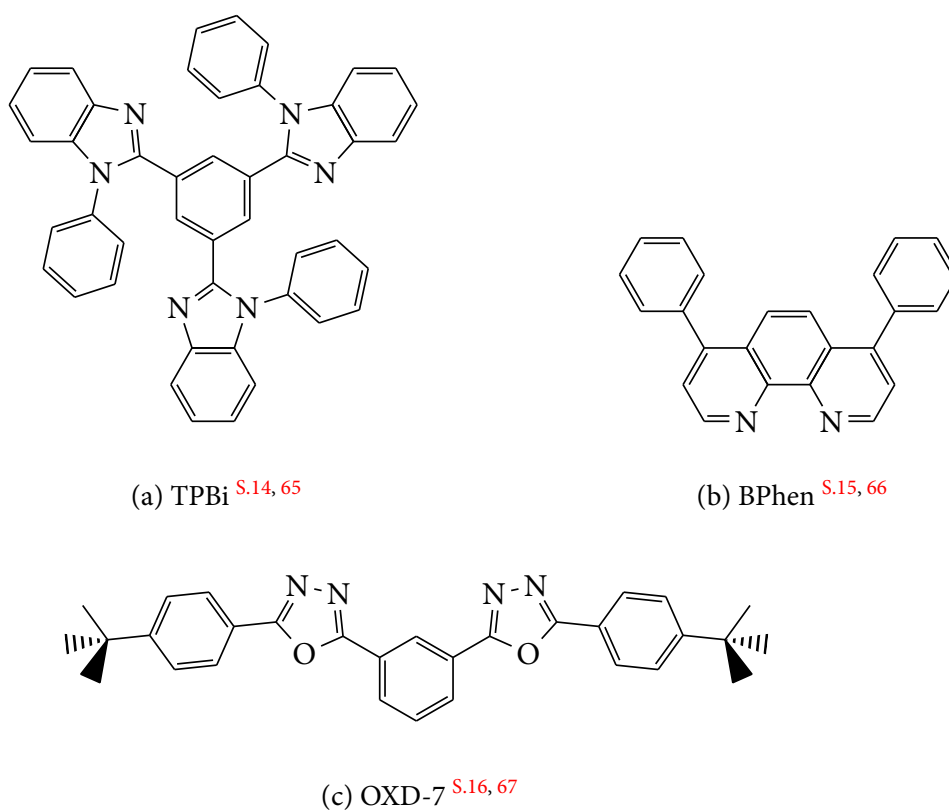
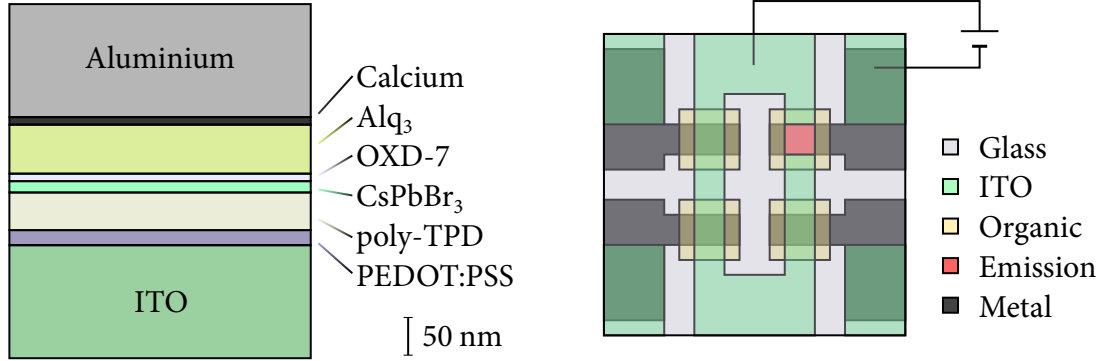


Figure 9: Lewis structure formulae of chemicals used electron transporting layers (ETLs).

4.2 Stack Design



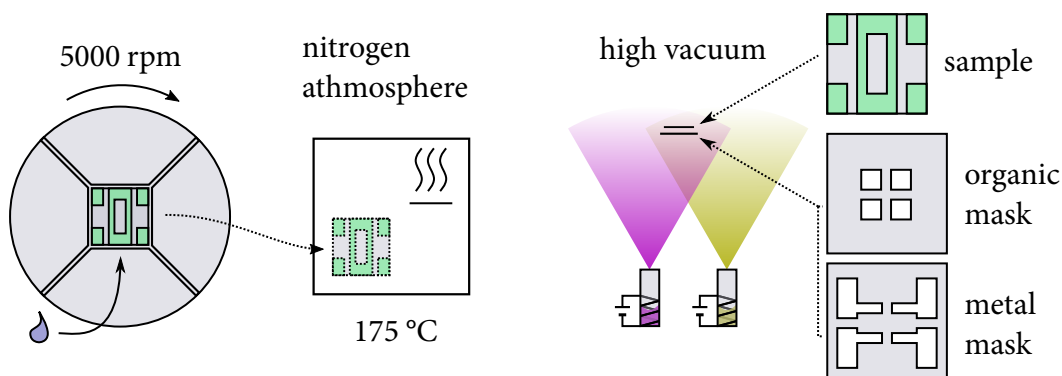
(a) Schematic stack design of an exemplary OLED, which is characterised in this thesis.^{S.17} (b) Schematic bottom view of a bottom-emitting OLED.^{S.18}

Figure 10: Sketches to demonstrate the composition of the fabricated OLEDs' device layout.

An OLED needs to have at least one transparent electrode, which consists of ITO (Indium Tin Oxide, $(\text{In}_2\text{O}_3)_{0.9}(\text{SnO}_2)_{0.1}$).⁷¹ On top of the structuring ITO the polymers are spin-coated. The crosslinked polymers are ground to the perovskites or perovskite quantum dots. All overlying layers are evaporated. That includes the metallic cathode. The vertical alignment of layers in an OLED, which is investigated in this thesis is shown in Fig. 10a. The structure of the ITO avoids any anode-cathode direct contacts. It is illustrated in Fig. 10b; in this image the polymers are not shown. The polymers are applied over the whole sample, since the spin-coating process allows no deposition of structured films. When using highly conductive polymers, like some derivatives of PEDOT:PSS, the structuring of the ITO gets lost. As a result the charge carriers will travel in plane from ITO to the metal. The PEDOT:PSS types used in this thesis exhibit negligible planar conductivity. Though the cross-plane conductivity is similarly low, the dissipating current is non-negligible because of the small distance the current has to flow. The in-plane leakage currents can be verified by measuring the j - V behaviour in reverse mode, that is applying positive potential at the metal and negative at the ITO.

On top of the polymers, the EML is either spin-coated or evaporated (for the Alq_3 and $\text{CBP}:\text{Ir}(\text{ppy})_3$ devices). The ETLs are evaporated only around the pixel to avoid leakage currents. The pixels have an area of $2 \times 2 \text{ mm}^2$, which is defined by the crossing of the ITO pattern and the evaporated metal. The Metals are evaporated in a "L"-shape. Like that, the resulting contacts in the corners are cathodes, while the area at the edges touched by the ITO "O" are the anode contacts. The glass substrate is 0.7 mm thick.

4.3 Fabrication Process



(a) Illustration of the spin coating procedure.^{S.19} (b) Illustration of the evaporation process of organics and metals.^{S.20}

Figure 11: Sketches to demonstrate the deposition of the layers of the fabricated OLEDs.

The ITO structured glass substrates are bought, so the ITO is sputtered externally. The stated thickness of 150 nm was verified by a profilometer. The substrates are cleaned by ultrasonic baths in solvents: Firstly, 10 minutes in acetone (grade: technical), followed by 10 minutes in acetone (grade: purissimum) and finally 10 minutes in isopropyl alcohol (grade: purissimum). After the solvent cleaning, a cleaning and surface activation by an UV-ozone treatment is done. The activation means a decreased workfunction (from about -4.7 eV to -5.3 eV)⁷² and an decreased contact angle of a water drop, which increases its ability of wetting, which helps depositing PEDOT:PSS, since its water based.⁷³ 15 minutes in the local UVO-cleaner are proven to have sufficiently high effect.^h

Spin Coating The polymers are spin-coated on top of the ITO. If not stated elsewhere, spin coating procedures for samples of this thesis are always: accelerating to 5000 rpm and stay at this rotational speed for 30 seconds. The substrates are placed on a hotplate, having a temperature of 130 °C or 175 °C for better crosslinking, if upper layers are solution processed. The freshly deposited layer will dry, any leftover solvents vaporise, and the polymers start a crosslinking process transforming them to become mostly insoluble in its original solvents. After 30 minutes the samples are removed from the hotplate. The whole spin-coating process is illustrated in Fig. 11a.

The layer thickness can be regulated by the rotation speed or the concentration of the solution. An expression for layer height (h) of an uniform fluid distribution is given by

^hAs studies by colleagues (special credits to M. Sc. Markus Schmid) of the chair showed.

Emslie et. al. in Ref. 74:

$$h = \frac{h_0}{\sqrt{1 + 4Kh_0^2t}}, \quad (3)$$

with:

$$K = \frac{\rho\omega^2}{3\eta}. \quad (4)$$

h_0 is the initial height of the fluid, t denotes the passed time, ρ the density and η the viscosity of the fluid. ω is the angular velocity, respectively the rotational speed. There is a reciprocal correlation between layer thickness and rotational speed, for low viscous fluids. That is because after 30 seconds for low viscous liquids, high rotational speeds (5000 rpm) and non-vanishing initial heights and densities: $4Kh_0^2t \gg 1$. So Eq. 3 simplifies to:

$$h = \frac{h_0}{\sqrt{4Kh_0^2t}} = \frac{1}{2\sqrt{\frac{\rho}{3\eta} \cdot t}} \cdot \frac{1}{\omega}. \quad (5)$$

However, there is evaporation of the solvent to consider, which alters the density as well as the viscosity with time. The empirical correlation was tried to be modeled by different groups. The solvent's evaporation has a time dependence as well, so there will be a steady state, which is assumed to be reached after 30 s. As a result the time dependence vanishes. With higher rotational speeds the solvent is evaporated faster, which increases the viscosity, increasing the resulting film thickness, denoted as height. So overall the equation 5 has to have a higher exponent (≥ -1) on omega. With Ref. 75 and 76:

$$h = c \cdot \frac{1}{\omega^x}. \quad (6)$$

Where c is a constant and x is between 0.5 and 1 depending on the evaporation rate of the solvent.⁷⁷ When using highly diluted solutions the change in viscosity, density and evaporation rate is negligibly small. So for controlling the layer thickness, the solution's concentration can be used. The thickness of a dried film is proportional to the thickness of a wet film.⁷⁵ At that, the concentration of solids in the solution is one of the proportionality factors. The wet film thickness won't change under already stated assumptions if rotational speed is held constant. So ideally a linear correlation between concentration and dried film thickness is present. As a linear relation is more intuitive and easier to fit than an inverse (root-) function, the layer thickness are mostly controlled by concentrations in this thesis.

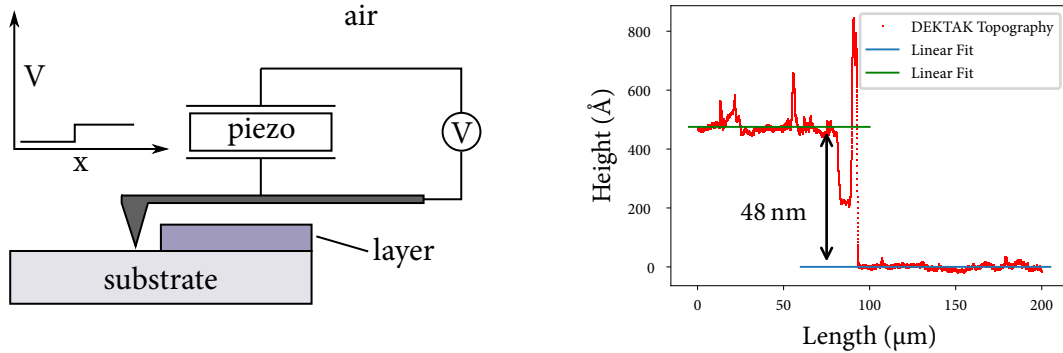
Evaporation Except for the polymers and the perovskites all other materials used in this thesis are evaporated. In a high vacuum the materials are heated until they sublime. The pressure is kept between 30 and 50 μPa during the whole evaporation process. The materials inside the crucibles are heated electrically, until an evaporation starts. The evaporation

rate is determined by a oscillating quartz crystal. The frequency of this quartz will change as material deposits on it. When placing the quartz crystal near the sample, a proportionality between frequency and layer thickness on the sample can be assumed. The respective factor can be determined by depositing a layer of unknown thickness and note the frequency change. The layer's thickness is determined by a profilometer; with that a relation between frequency change and layer thickness is found. The metals are evaporated by the same principle, but due to the high boiling, respectively sublimation points, higher power is necessary. By water-cooling the excess heat is dissipated. As illustrated in Fig. 11b two different materials can be evaporated at the same time. Thus a volumetric dopingⁱ is possible. The appropriate masks ensure the desired structure on the sample; the masks are placed below the sample, into the evaporation stream.

ⁱdoping, where only the volumetric ratio is known.

5 Methods of Characterisation

5.1 Profilometry



(a) Illustration of the functionality of a profilometer.^{S.21} (b) Exemplary plot of a profilometer measurement.^{S.22}

Figure 12: A sketch and plot to demonstrate the measurement of layer thicknesses with a profilometer.

A profilometer is a device, which is able to determine a surface topography. With a needle and piezo electric sensors, it is able to measure the movement of the needle's tip. The piezo electric sensor yields a voltage depending on the stress respectively the force onto the piezo electric crystal. If the piezo electric crystal is attached to the needle, the force (or lack of force) on the needle, exerted by the samples height difference is also applied to the piezo electric crystal (see Fig. 12a). The height change in the piezo electric is proportional to the height change on the sample. So once calibrated, a proportional relation between voltage and height is given.

In this thesis, the profilometer is used to measure layer thicknesses. The layer has to be removed at a certain location where the profilometer measures the edge between removed and present layer. The sharper the edge, the better the result. Steepest gradients were achieved, when using a sharp flat blade (e.g. razor blade). This blade is grinded over the substrate; where the blade touched the sample, all layers are completely removed. At one end of the blade there is a steep gradient between layer and removed layer. Some of the removed material will pollute the gradient. But as shown in Fig. 12b, over the 200 μm measurement range the layer and substrate have a constant height. With linear (constant; slope equals zero) fits the layers height can be calculated. The measurements are performed in

ambient air. All calculations,^a from raw data obtained from DEKTAK 8 Advanced Development Profiler by Veeco Instruments, to the shown plot can be consulted on reference S.22. The used profilometer, DEKTAK 8 by Veeco Digital Instruments, was set up, with a tip force equivalent to 1 mg and driving speeds around 100 μm in 30 seconds ($3\text{-}4 \frac{\mu\text{m}}{\text{s}}$). The profilometer fails to yield representative data, when the layers are too soft and can be skimmed by the measuring needle. The accuracy of this profilometer is depending on the measured material. For the polymers the error was estimated by AFM measurements to be smaller than 5 nm.

5.2 Atomic Force Microscopy (AFM)

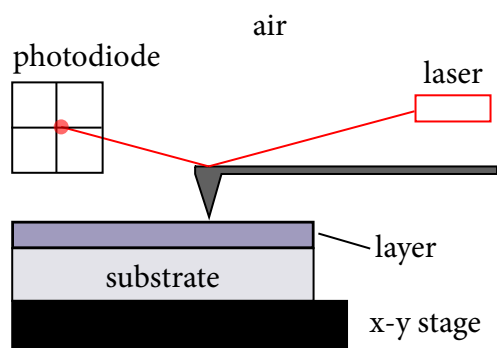


Figure 13: Sketch, illustrating the working principle of an atomic force microscope (AFM). The laser hits the back of a cantilever. Its reflection is registered by a photodiode array. So the slightest change of angle of the laser beam results in a power ratio change between the photodiodes.^{78, S.23}

However, the layer thickness of the perovskites can't be obtained with the present profilometer. The crystalites and quantum dots may be too easily moved on the substrate by the needle. This could be solved by evaporating a hard material, like a metal, on top. But since the atomic force microscopy (AFM) yields higher accuracy and a non-contact mode, the layer thicknesses were estimated by AFM and on-edge scanning electron microscopy (SEM) measurements. An AFM's principle resembles the one of the profilometer. It is using a laser to measure the deflection of the so called cantilever, which is like the needle for the profilometer, but with a very small tip width (smaller than 20 nm). With that, an extremely high accuracy is achieved, low forces as low as femtonewtons (10^{-15} N) can be registered.⁷⁸ With van-der-Waals forces, which can be up to 35 pN ($3.5 \cdot 10^{-11}$ N), a non-contact measurement is still very accurate.⁷⁹ Like that the sample remains undamaged and even soft layers can be precisely analysed. The sample is placed on a x-y movable stage. So with rastering the surface can be scanned in two directions. The topographic information known in two directions leads to a 3D image of the surface. Usually, illustrations are made with pseudo-colours, to enhance visibility of points of interest. The size of the image is limited by the movement speed and operation borders of the stage. The AFM used for all

^adone with python 3.6 in an ipython notebook developing environment

measurements of this thesis is by Park Scientific Instruments: AutoProbe CP Model AP1000 (SN: CP4740).

5.3 Scanning Electron Microscopy (SEM)

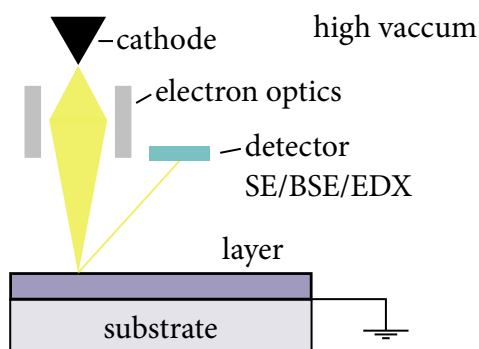


Figure 14: Sketch for understanding the working principle of a scanning electron microscope (SEM). The cathode emits electrons which are focused by electron optics. The focused electron beam hits the sample, emitting Secondary Electrons (SE), Back-scattered Electrons (BSE) and x-ray radiation (used for energy dispersive x-ray spectroscopy, EDX).^{78, S.24}

For scanning electron microscopy (SEM) there is no inherited size restriction. The electron optic and the detector can be zoomed to yield the desired image size. Therefore the SEM is more suitable to screen the whole device. However, the SEM can not yield reliable information about height differences. The data obtained by a SEM resemble data of a top-down photography; no information about the height can be directly extracted. By shadows and blurring the relative heights can be estimated. The SEM yields resolutions down to 1 nm.⁷⁸ This is enabled by the use of electrons instead of light as probing medium. Photons have a resolution threshold ruled by their energy. Same is valid for electrons, but electrons can be accelerated to have de Broglie wavelengths as high as the wavelengths of γ photons, while maintaining a high interaction crosssection. The energies used are up to 100 keV.⁷⁸ Photons of that high energies have low interaction (photoelectric) crosssection,⁸⁰ while electrons have an inherently high crosssection, due to their charge. Another drawback of the SEM is, that it harms the sample. The areas scanned by SEM are damaged by the high energy electrons. Furthermore, the electrons will lead to an electrical charging, so the sample has to be conductive, grounding the excess charges. The polymers show a sufficiently high conductivity, so the edge of the sample, consequently the whole sample, is grounded by conductive tape. There are different types of returning signals after an electron beam interaction with the sample and therefore different detectors are present: Secondary electrons (SE), SE detector. The secondary electrons yield information about the topography, because they are emitted from not very deep in the sample. Back-scattered electrons (BSE), BSE detector. These electrons are elastically scattered by heavy element atoms, the BSE yields information of material contrast. This can be used to spot holes in the perovskite layer, because lead is a relatively heavy atom compared to all organic components of the polymers. So this property should yield a high contrast.

The electrons will also cause the emission of x-ray photons. These can be used to identify elements in the layer, by energy dispersive x-ray spectroscopy. A simplified sketch of the functionality of a SEM is shown in Fig. 14. SEM- images are very useful for applications where large areas have to be screened, for example to get information about the film coverage.

5.4 Electrical and Optical Characterisation of OLEDs

For characterising the OLEDs, the electrical diode properties are measured while at the same time obtaining luminance. Furthermore the colour respectively the spectrum is taken. With the correlation between voltage-current-luminance and the spectrum the EQE can be estimated.

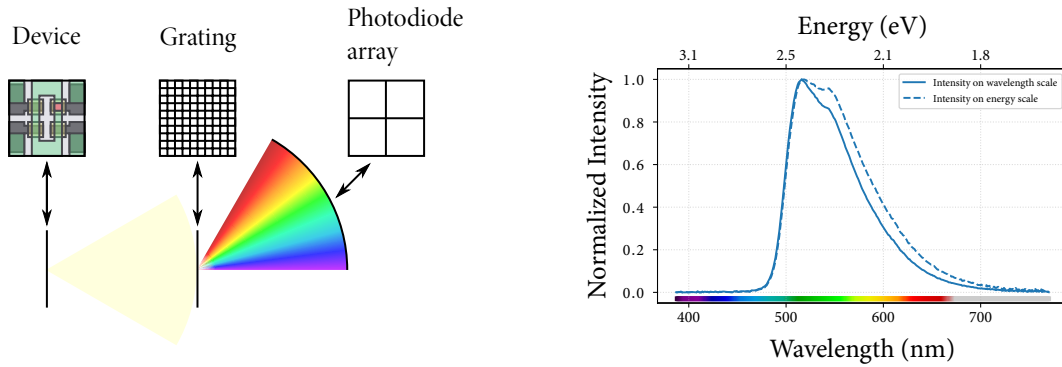
5.4.1 j-V-L Characteristic curve

A fundamental part of the electrical characterisation of OLEDs is the dependence of current density (j) to the applied voltage (V). There are three regions of interest in an OLED's j-V characteristics:⁸¹ The region from negative applied voltage to low positive voltages: In this region ideally no current should be flowing. But as there are some leakage currents present. These currents arise from impurities, holes in the film and non-vanishing in-plane conductivity. Consequently, currents in this region exhibits an ohmic relation ($j \propto V$).

The region starting with an exponential increase of current density: In this region the diode has its working point, luminance should be visible. The relation between j and V should be similar to the Shockley equation^b; thus an exponential relation is expected ($j \propto e^V$).

The last region, the exponential increase is gradually weakening, resulting in injection limited or space charge limited current.⁸³ When there is a space charge limited current ($j \propto V^2$)⁸¹, material parameters like charge carrier mobility can be estimated.

Moreover, the luminance to voltage behaviour give information on the brightness of the device. Along with the j-V behaviour a j-L relation can be created. With that important photometric quantities like luminous efficacy, current efficacy and current efficiency can be obtained. With the known emission spectrum and the response function of the photodiode the EQE can be identified. The photodiode yields only a current depending on the incident radiant power. To obtain photometric quantities like luminance and radiance a calibration is needed (see section 8.2).



(a) Illustration of the functionality of a spectroradiometer.^{S.25} (b) Exemplary plot of a spectrum with energy and wavelength scale.^{S.26}

Figure 15: A sketch and a plot to demonstrate the measurement of layer thicknesses with a profilometer.

5.4.2 Emission Spectra

The emission spectra of the OLEDs are measured with a VIS Spectroradiometer by JETI Technische Instrumente GmbH: specbos 1201focus. The measurement range is the visible spectrum, that is, wavelengths from 380 to 780 nm. The spectral radiance is measured in 1 nm wavelength intervals. This is achieved, by leading the emitted light through a diffraction grating; the light is spatially separated by wavelength. To get the intensity at each wavelength, an array of photodiodes is distributed over the area where the partitioned light arrives. This procedure is depicted in Fig. 15a.

To compare the colours of different devices, the spectral radiance is normalised. Furthermore the spectral radiance (unit: $\frac{\text{W}}{\text{sr} \cdot \text{m}^2 \cdot \text{nm}}$) is proportional to the spectral radiant flux (unit: $\frac{\text{W}}{\text{nm}}$). Note that this quantity is not proportional to the number of photons emitted per wavelength; the measurement software automatically converts it to radiance by multiplying with the respective wavelength and the calibrated factor to obtain Watt per steradian and square meters.

Most spectrometers resolve in wavelength. For characterising the emission, a Gaussian-fit over the curve would be appropriate. However, the Gaussian distribution arises from the Gaussian distribution of the optical transitions. These transitions are normally distributed on energy scale, so the spectrum will be too. So a fit is only valid over spectral radiance in unit $\frac{\text{W}}{\text{sr} \cdot \text{m}^2 \cdot \text{eV}}$ or the like. The conversion between the wavelength scale spectral radiance $L_{e,\lambda}$ and the energy scale spectral radiance $L_{e,E}$ is given by Eq. A.76. A factor of $\frac{\lambda^2}{hc}$ is needed to convert between these two quantities. The difference is illustrated by the plot in Fig. 15b. The solid line is just the unaltered normalised spectral radiance ($[L_{e,\lambda}] = \frac{\text{W}}{\text{sr} \cdot \text{m}^2 \cdot \text{nm}}$), while

^b $I = I_0 \cdot (e^{qV/k_B T} - 1)$ ⁸²

the dashed line is the energy-scale spectral radiance ($[L_{e,E}] = \frac{W}{sr \cdot m^2 \cdot eV}$) with only units converted. For more information on this calculation refer to Ref. S.26. There is a difference which alters the maximum position and FWHM^c of a Gaussian curve by a few nanometers. Note that the Gaussian fits are only symmetrical in the linear energy scale, though Fig. 15b is linear in wavelength.

5.4.3 Estimation of the External Quantum Efficiency (EQE)

An EQE can be determined for comparing devices with each other. An alternative, more intuitive definition of the EQE, beside Eq. 1, is given by the number of photons emitted (N_{ph}) per charge carriers injected (N_{cc}). In a steady state, the generation ratios have to be the same, too:

$$\eta_{EQE} = \frac{N_{ph}}{N_{cc}} = \frac{\dot{N}_{ph}}{\dot{N}_{cc}}. \quad (7)$$

With \dot{N}_{ph} the photon generation rate (measured externally) and \dot{N}_{cc} the charge carrier injection rate:

$$\dot{N}_{ph} = \frac{\text{Total power of emitted photons}}{\text{Average energy per photon}} = \frac{P_{tot}}{\bar{E}_{ph}}. \quad (8)$$

$$\dot{N}_{cc} = \frac{\text{Current}}{\text{Elementary charge}} = \frac{I}{e}. \quad (9)$$

The total power of emitted light is determined via 0° Luminance and the Lambertian law. According to it the radiant intensity I_e (unit: Watt/steradian) and the radiance L_e is correlated:

$$I_e(\theta) = A \cdot L_e \cdot \cos\theta. \quad (10)$$

With A the emitting area (Pixel) and θ the angle to the area's normal. To determine the total radiant flux (Φ_e) which equals the total power of emitted photons, the radiant intensity (I_e) is integrated over the whole steradian:

$$\Phi_e = \int_{\Omega} A \cdot L_e \cdot \cos\theta \, d\Omega. \quad (11)$$

$$\Phi_e = \int_0^{\frac{\pi}{2}} \int_0^{2\pi} A \cdot L_e \cdot \cos\theta \sin\theta \, d\phi \, d\theta. \quad (12)$$

$$\Phi_e = 2\pi \cdot A \cdot L_e \cdot \int_0^{\frac{\pi}{2}} \cos\theta \sin\theta \, d\theta. \quad (13)$$

$$\Phi_e = \pi \cdot A \cdot L_e. \quad (14)$$

^cFull width half maximum

The average energy per photon is:

$$\bar{E}_{\text{ph}} = \frac{\int_0^\infty E(\lambda) \cdot \Psi(\lambda) d\lambda}{\int_0^\infty \Psi(\lambda) d\lambda}. \quad (15)$$

With Ψ being the spectral distribution of the photons and E the energy of a photon with given wavelength according to the Plank-Einstein relation. The spectral distribution can be measured, so that discrete and equidistant data is present. With N being the number of data tuples, the integral has to be rewritten as a Riemann sum over N discrete wavelengths:

$$\bar{E}_{\text{ph}} = \frac{\sum_{i=0}^N E(\lambda_i) \cdot \Psi(\lambda_i) \cdot \Delta\lambda}{\sum_{i=0}^N \Psi(\lambda_i) \cdot \Delta\lambda}. \quad (16)$$

Ψ can be chosen to be normalised:

$$1 = \sum_{i=0}^N \Psi(\lambda_i). \quad (17)$$

$$\bar{E}_{\text{ph}} = \sum_{i=0}^N E(\lambda_i) \cdot \Psi(\lambda_i). \quad (18)$$

With Eq. 14 and Eq. 18:

$$\dot{N}_{\text{ph}} = \frac{\pi \cdot A \cdot L_e}{\sum_{i=0}^N E(\lambda_i) \cdot \Psi(\lambda_i)}. \quad (19)$$

With the candela filter on the OLED-Box Setup the Radiance L_e can not be measured, but the Luminance. With Eq. A.6:

$$\Phi_v = K_m \cdot \int_0^\infty V(\lambda) \frac{\partial \Phi_e}{\partial \lambda} d\lambda. \quad (20)$$

Again lambertian emitter as approximation:

$$L_v = K_m \cdot \int_0^\infty V(\lambda) \frac{\partial L_e(\lambda)}{\partial \lambda} d\lambda. \quad (21)$$

With $L_{e,\lambda}$ the spectral radiance:

$$L_v = K_m \cdot \int_0^\infty V(\lambda) L_{e,\lambda}(\lambda) d\lambda. \quad (22)$$

Riemann sum to apply discrete data:

$$L_v = K_m \cdot \sum_{i=0}^N V(\lambda_i) L_{e,\lambda}(\lambda_i) \Delta\lambda. \quad (23)$$

The spectral radiance can be rewritten as a constant radiance per wavelength times the spectral distribution function (according to Eq. A.30 ff.):

$$L_{e,\lambda}(\lambda_i) = \frac{L_e}{\Delta\lambda} \cdot \Psi(\lambda_i). \quad (24)$$

$$L_v = K_m \cdot \frac{L_e}{\Delta\lambda} \cdot \sum_{i=0}^N V(\lambda_i) \Psi(\lambda_i) \Delta\lambda. \quad (25)$$

This yields an expression for the radiance:

$$L_e = \frac{L_v}{K_m \cdot \sum_{i=0}^N V(\lambda_i) \Psi(\lambda_i)}. \quad (26)$$

So overall:

$$\dot{N}_{ph} = \frac{\pi \cdot A \cdot \frac{L_v}{K_m \cdot \sum_{i=0}^N V(\lambda_i) \Psi(\lambda_i)}}{\sum_{i=0}^N E(\lambda_i) \cdot \Psi(\lambda_i)}. \quad (27)$$

$$\dot{N}_{ph} = \frac{\pi \cdot A \cdot L_v}{K_m \cdot \sum_{i=0}^N V(\lambda_i) \Psi(\lambda_i) \cdot \sum_{i=0}^N E(\lambda_i) \cdot \Psi(\lambda_i)}. \quad (28)$$

With $E = h \frac{c}{\lambda}$:

$$\dot{N}_{ph} = \frac{\pi \cdot A \cdot L_v}{K_m \cdot hc \cdot \sum_{i=0}^N V(\lambda_i) \Psi(\lambda_i) \cdot \sum_{i=0}^N \frac{1}{\lambda_i} \cdot \Psi(\lambda_i)}. \quad (29)$$

together with Eq. 7 and 9

$$\eta_{EQE} = \frac{\pi \cdot A \cdot e \cdot L_v}{K_m \cdot hc \cdot I \cdot \sum_{i=0}^N V(\lambda_i) \Psi(\lambda_i) \cdot \sum_{i=0}^N \frac{1}{\lambda_i} \cdot \Psi(\lambda_i)}. \quad (30)$$

Simpler with current density j :

$$\eta_{EQE} = \frac{\pi \cdot e \cdot L_v}{K_m \cdot hc \cdot j \cdot \sum_{i=0}^N V(\lambda_i) \Psi(\lambda_i) \cdot \sum_{i=0}^N \frac{1}{\lambda_i} \cdot \Psi(\lambda_i)}. \quad (31)$$

The EQE has an error which is inherited by the luminance measurements. But in fact the pixel-size cancels out: compare Eq. 30 with Eq. A.27. So the systematic error of the EQE measurement is with 24.9 % smaller than the systematic error of the luminance measurements of 26.8 % (see section 8.2.6). Note that this error is not included in the error bars of the graphs, since these are only for comparing similar devices, where systematic errors can be neglected.

6 Experimental Results

This section features all obtained and interpretable data. Initially, the two polymers are characterised optically and electrically. At that, the processability is optimised: concentrations and solvents are varied to yield reproducible homogeneous films with reproducible layer thicknesses. Perovskite-free OLEDs are fabricated to proof the concept and to give a rough estimate on the performance of the HTLs. With a working stack design, the emitter material is exchanged with a perovskite. Therefore, the perovskites are introduced. Firstly the processability and the properties of the plain layer is analysed. After that the perovskite is implemented into the already tested OLED stack. While the (MA)PbI₃ perovskite is only investigated briefly, the CsPbBr₃ is further optimised and therefore custom devices are fabricated.

6.1 Polymeric Hole Injection Layers

In section 4.1.2 the two tested polymers are already shown. Now the used polymers are processed and characterised. At first the films are characterised in morphology and optical properties. After that the application of the polymer in OLEDs are tested.

6.1.1 Polymer-film properties

	Concentrations			
Solution	7 mg/ml	10 mg/ml	15 mg/ml	27 mg/ml
PEDOT:PSS (AI4083)	12 nm	18 nm	36 nm	-
PEDOT:PSS (CH8000)	<5 nm	12 nm	13 nm	37 nm

(a) Layer-thicknesses of samples manufactured with different PEDOT:PSS concentrations. ^{S.27}

	Concentrations			
Solution	1.5 mg/ml	3 mg/ml	5 mg/ml	10 mg/ml
poly-TPD in chloroform	22 nm	42 nm	>60 nm	-
poly-TPD in chlorobenzene	-	<5 nm	12 nm	19 nm

(b) Layer-thicknesses of samples manufactured with different poly-TPD concentrations. ^{S.27}

Table 1: Concentration-layer-thickness relation of the polymer solutions

Layer thickness tuned by concentration The AI 4083 solution is diluted to ≈ 10 mg/ml and ≈ 7 mg/ml, when assuming 15 mg/ml concentration in the original solution (Man-

ufacturer states: 13-17 mg/ml).³⁶ The CH8000 is diluted to ≈ 14 mg/ml, ≈ 9 mg/ml and ≈ 6 mg/ml, when assuming 27 mg/ml (Manufacturer states: 24-30 mg/ml).³⁶ The standard fabrication procedure, described in section 4.3 with heating to only 130 °C, is used. Table 1a, suggests a linear correlation between concentration and layer thickness: The PEDOT:PSS (AI4083) shows a nearly linear correlation. PEDOT:PSS (CH8000) is measured over a wider range where it deviates the linear relation. With that the layer thicknesses between 40 nm and 10 nm are tunable.

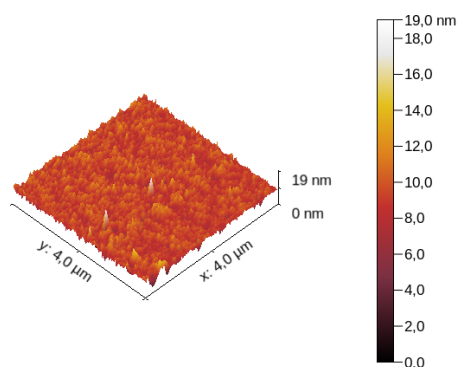
The poly-TPD, is bought from lumtec in a average molecular weight of $\bar{M}_w = 2 \cdot 10^4$.³⁵ The poly-TPD can be dissolved in non-polar solvents with aromatic electronic systems.⁸⁴ For the deposition of poly-TPD solutions based on chloroform and chlorobenzene are fabricated. Solutions with following concentrations were manufactured: 1.5 mg/ml, 3 mg/ml, 5 mg/ml, 7 mg/ml and 15 mg/ml, for chloroform and chlorobenzene respectively. While the chloroform solution is very yielding, the chlorobenzene solution is easier to process. The chloroform evaporates very fast, resulting in some major stains on the sample, additionally its low surface energy leads to having trouble keeping it inside the pipette. The high fertility of the chloroform solution is compensated by the need to use large volumina to counter the high evaporation rate.

Finally, for each polymer thicknesses can be appropriately engineered. However, the combination of the both polymer, that is, stacking poly-TPD on top of PEDOT:PSS, will have a different thickness than just adding the two respective values of table 1. In fact it has been shown, that the stack is about 25 % thicker than the sum of the single values.^{S.27}

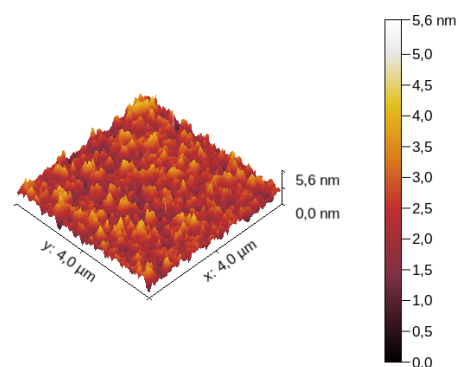
Surface morphology The surface quality of the PEDOT:PSS is determined with samples, where 7 mg/ml PEDOT:PSS (AI4083) and 13 mg/ml PEDOT:PSS (CH8000) is spin-coated onto ITO coated substrates. The AFM images (Fig. 16a and Fig. 16b) show a major difference in structure. Even though the PEDOT:PSS builds very smooth films, the CH8000 has a much smoother surface. This may arise by the fact that the higher ratio of PSS helps building smoother layers. Overall with such smooth layers there is no need to worry about effects which originate from roughness. Rough layers show leakage and bypass paths, if upper layers are not thick enough. Especially when spin coating the upper layers, the tips arising from the polymer's roughness could be higher than the spin coated layer, so that the newly spin coated layer can be bypassed by charge carriers. While most emitting layers can be varied in thickness, the quantum dots should be mono-layered. Typical sizes of quantum dots are bigger than 5 nm so that the roughness of PEDOT:PSS is low enough to avoid any roughness impairments even in mono-layered thickness.

The poly-TPD spin coated on ITO is even smoother than both variations of PEDOT:PSS's (see Fig. 16c). However, when spin coating the poly-TPD on top of PEDOT:PSS the roughness inherits or adds up, resulting in a still smooth layer (see Fig. 16d).

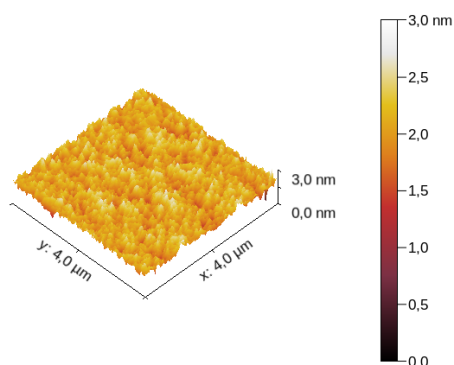
Overall neither the thickness nor the morphology of poly-TPD is altered strongly with solvent treatments of many common solvents. The only solvents showing a tremendous



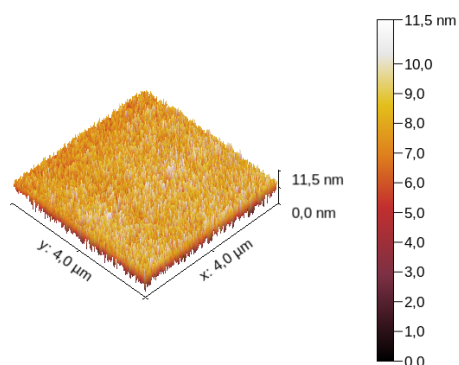
(a) AFM image of a PEDOT:PSS (AI4083) layer. The roughness (by root mean square) was determined to be 1.2 nm. [S.28](#)



(b) AFM image of a PEDOT:PSS (CH8000) layer. The roughness (by root mean square) was determined to be 0.6 nm. [S.29](#)



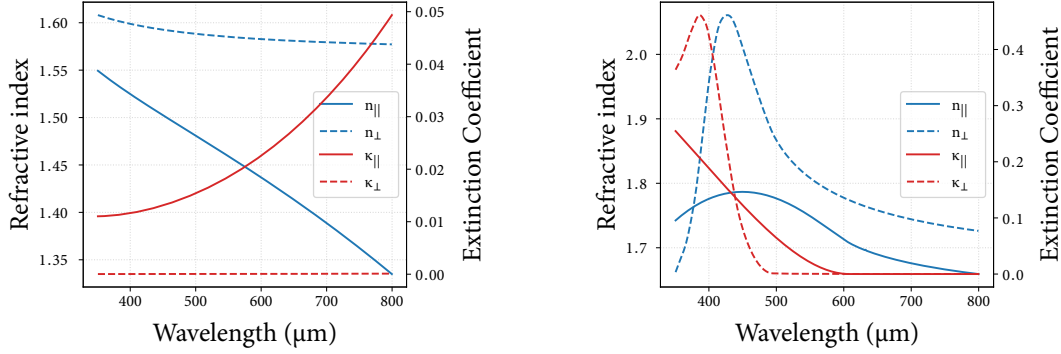
(c) AFM image of a poly-TPD layer processed with chloroform. The roughness (by root mean square) was determined to be 0.2 nm. [S.30](#)



(d) AFM image of a poly-TPD layer spin-coated onto PEDOT:PSS (AI4083). The roughness (by root mean square) was determined to be 1.7 nm. [S.31](#)

Figure 16: AFM measurements to compare surface morphology of the polymer layers.

surface morphology change are DMSO^a and DMF^b. So when processing perovskites such as the (MA)PbI₃ solved in DMF this surface reaction could lead to a major impairment.



(a) PEDOT:PSS absorbs in the IR-regime, which is not of concern for OLEDs and organic solar cells

(b) Poly-TPD absorbs at low wavelengths, which is a disadvantage for building solar cells or blue LEDs

Figure 17: Dispersion relation of the Polymer HIL derived from VASE. “n” denotes the refractive index and “κ” the extinction coefficient. A difference between planar (||) and orthogonal (⊥) optical behaviour can be recognised in both polymers.

Optical Properties Since the LED stack is designed to emit light through the bottom substrate, the optical properties of the HTLs are important for light outcoupling. Hence, the light, crossing the different layers, will be reflected and diffracted, that interference effects become important. To get constructive interference, the emission of the light should have $\lambda/4^c$ distance to the glass plane where it should be extracted. This can be easily understood by the simple image of a standing wave between anode and cathode. The waves knots are forced to be in the electrodes, because planar electric fields vanish in metals. So minimum distance between electrodes is $\lambda/2$. Higher modes, satisfying $(2n + 1) \cdot \lambda/2^d$, are also thinkable, but require bigger devices, which counteracts with the low conductivity of the organic semiconductors. After all, the wave is not propagating in vacuum so that: $\lambda \neq \frac{c}{f}$, the wavelength λ is *not* equal to the fraction of the vacuum-speed-of-light (c) over the frequency (f). Inside of media, the dispersion-relation is to consider. So in order to choose the right thickness, the refractive index is necessary. Furthermore, since the wave has to cross the HIL, its absorbance of the respective wavelength should be very small as well.

^aDimethylsulfoxide

^bDimethylformamide

^cwith λ being the wavelength of the emitted light inside of the device

^d $n \in \{1, 2, 3, \dots\}$

To determine these two values the Variable Angle Spectroscopic Ellipsometry (VASE) is a suitable device: The VASE is a non-destructive tool to determine among others the refractive index as well as the extinction coefficient of a solid material. While plain ellipsometry experiments use and measure the polarisation of incident and reflected light, the VASE measures these values at different wavelengths and different angles. Thus with a suitable model almost all optical constants can be determined. Sample-layers are deposited on a silicon wafer, to guarantee high reflectance. PEDOT:PSS (AI4083) and poly-TPD are measured.

For PEDOT:PSS a model with two Drude-Lorentz oscillators are enough to represent its anisotropic optical properties (see figure 17a). There is an absorption, when the electric field vector (\vec{E}) of the incident photon is in plane with the PEDOT:PSS, in the IR range. This is expected and probably arises from polaron-absorption.^{85, 86} The measured data matches the data previously obtained at the chair see reference 87 and reference 86. Poly-TPD was modelled with a sum of Tauc-Lorentz oscillators (some turned into Gaussian). The data is shown in Fig. 17b and is partly confirmed by data of Ref. 88. It deviates only in quantity, that is the refractive index of them is higher. The refractive index is slightly higher overall than PEDOT:PSS' ($\approx +10\%$). More notably poly-TPD has an absorption maximum in the UV respectively the blue visible regime. This makes poly-TPD less suitable for devices using blue light (solar cells, blue OLEDs). Even wavelengths up to 600 nm are slightly impaired (see Fig. 17b). At that, the parallel part of the extinction coefficient is the most important for judging about light outcoupling, because the perpendicular part impairs the part of light which is directed parallel to the interface (because $\vec{k} \perp \vec{E}$) and wouldn't be able to get out anyway.

6.1.2 Performance in OLEDs

The layer sequence, that is used for initial testing OLEDs, is shown in Fig. 18a. From left to right: The 150 nm ITO is, as already explained, essential for the structuring. On top of ITO, the PEDOT:PSS (CH8000) is applied in concentration of 15 mg/ml and poly-TPD, solved in chlorobenzene with a concentration of 10 mg/ml, is deposited subsequently. NPB is evaporated on the polymers. In some OLEDs, either NPB, poly-TPD, both or none are omitted to investigate the influence of the respective layers. The thickness of the evaporated layers are chosen that way, that there is a standing wave between the electrodes and ideally the waves antinodes are located exactly at the interface between Alq₃ and NPB, where the emission is expected to occur. For further information refer to reference 89.

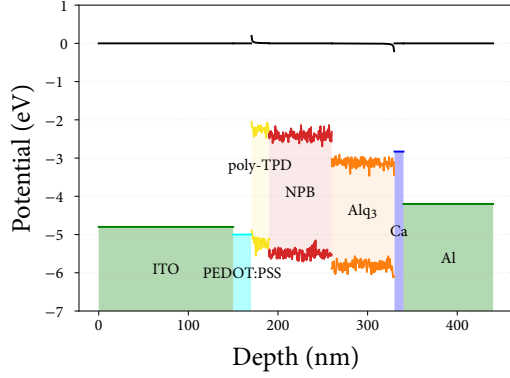
The electroluminescent (EL) spectrum, shown in Fig. 18b, matches with the Alq₃ EL spectra of the literature only below 520 nm,^{90, 91} considering Fig. A.3 the literature EL spectrum matches the partial mono Gaussian fit, with peak position slightly smaller (-10 nm) at 518 nm (2.39 eV) and a tighter (-40 nm) FWHM^e of 0.31 eV that is about 68 nm. But it,

^eFull Width Half Maximum

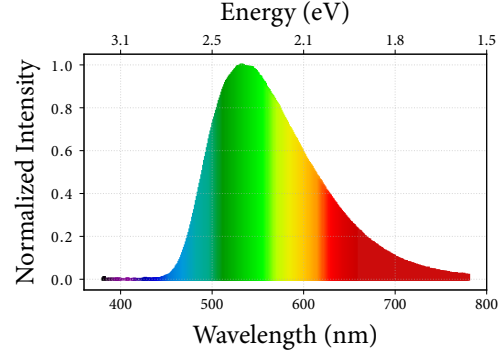
the first mono Gaussian fit, matches the Alq₃'s photoluminescent (PL) spectra of the references quite well. Note that the EL spectrum is often shifted by influences of the device, like cavity or substrate. The spectrum was fitted on energy scale with a double Gaussian fit, that is, the sum of two Gaussian functions. The fit represents the data below 600 nm quite good, while above, there might be a third emission. The second emission is about 0.24 eV lower in energy which is about the same as the difference of the HOMOs of NPB and Alq₃. Hence an exciplex state could be the origin of these additional emission. Apart from that, the OLED's cavity alters the spectrum inhomogeneously, so there may be no second emission, but the spectrum is no longer Gaussian caused by the distortion of this alteration. Anyway, for comparing the hole injection layers this emitter suffices for the beginning.

The j-V-L dependence of the devices are shown in Fig. 18c. At first sight, the trend of fewer layers leading to higher current densities is noticed. That property is true in the ohmic regime (-2 V to 2 V) and also for elevated voltages. Tremendously lower current has only the combination of two HTLs (poly-TPD and NPB), the current was so small that no luminance was observable.

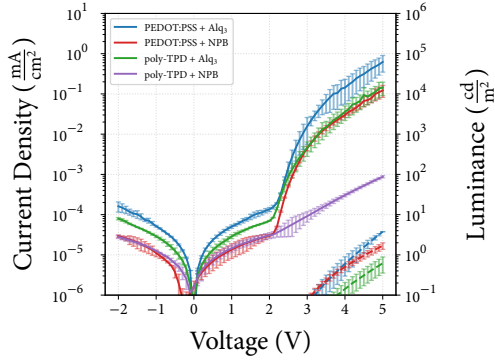
For determination of the EQE the voltages were increased so that every device reached a luminance high enough for a < 25 % error in EQE, that is, $0.5 \frac{\text{cd}}{\text{m}^2}$ (see section 8.2.6). The EQE of the poly-TPD based devices are lower than the EQE of according devices without it (red better than violet and blue better than green; see Fig. 18d). With the present data this could have several reasons: On the one side, there is a worse charge carrier balance of poly-TPD based devices than NPB based. The poly-TPD could have worse hole transport properties or show worse electron blocking abilities, while having a high resistance in general. Another reason could be an optical loss which can be seen when considering the EL spectrum of the poly-TPD -Alq₃ device (see Fig A.4). It is red-shifted with respect to the NPB-Alq₃ spectrum. Thus, the spectrum can no longer be fitted with a double Gaussian, where one of the Gaussian is located at ≈ 518 nm. But as the Alq₃ is still the main emitter, this emission has to be present inside the device. Consequently, there is a considerable amount of photons, that are not out-coupled, lost inside the device. This could be caused by the absorption of poly-TPD (see Fig. 17b), or by destructive interference as the cavity size is altered. These effects can be strong enough to yield the observed difference in EQE. For getting comparable results the poly-TPD should be as thick as the NPB, to minimise the optical outcoupling impairments. Additionally the introduction of a hole blocking material should improve the stack, so that a EQE value near the theoretical maximum can be achieved.



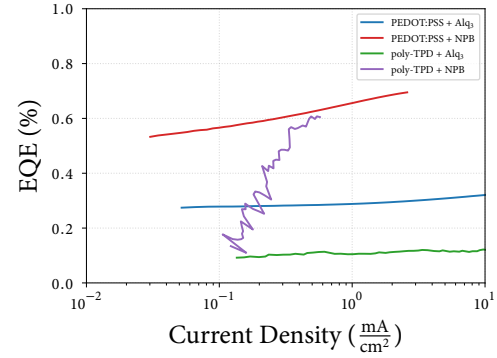
(a) Schematic layer stack design of the investigated OLEDs. [S.32](#)



(b) Electroluminescent emission spectrum of the OLED based on NPB-Alq₃ as emitter. [S.33](#)



(c) Current density and luminance vs voltage plot of the prepared Alq₃ based OLEDs. The dashed lines represent the respective luminance. At that, the purple line is not shown, since its luminance is too low. [S.34](#)

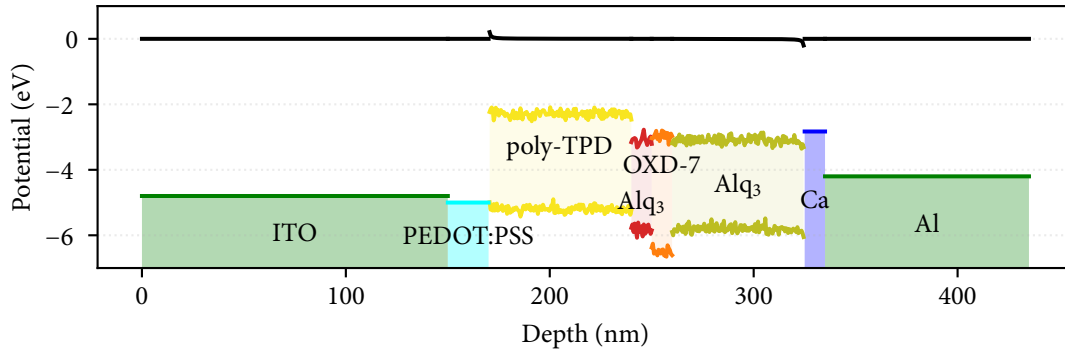


(d) EQE vs current density plot. The EQE is clipped for luminances less than $0.5 \frac{\text{cd}}{\text{m}^2}$ and the luminances were measured at elevated voltages (for more information refer to Ref. [S.34](#)).

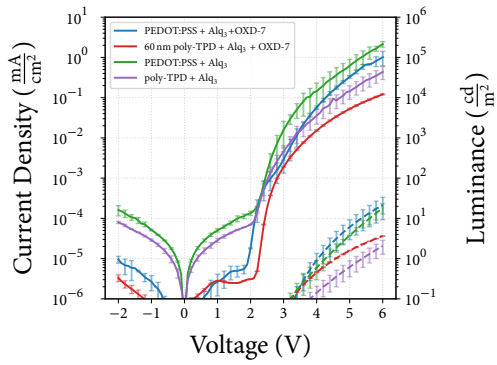
Figure 18: Characterisation of the Alq₃ based OLEDs. Four devices are investigated where the HTLs, NPB and poly-TPD, are partly omitted. Hence, a device as shown in (a) is the “poly-TPD + NPB”. Therefore, the “PEDOT:PSS + Alq₃” device is the same stack design with both HTLs omitted. The red line’s device has only poly-TPD omitted and the green line’s device has only the NPB omitted.

OXD-7 is added to the stack in a way, that the Alq₃ stays emitter while also being electron transporting layer (see Fig. 19a). Additionally, the layer thickness of poly-TPD is increased. With thicker poly-TPD layer the failure rate is significantly decreased. Such failures manifests as high leakage currents, while the luminance stays similar. So overall, on top of PEDOT:PSS, there is 60 nm poly-TPD deposited. 10 nm Alq₃ builds the emitting layer, which is separated from the 65 nm electron transporting Alq₃, by a 10 nm thick OXD-7 layer. The same stack is tested without poly-TPD to compare the charge carrier balance.

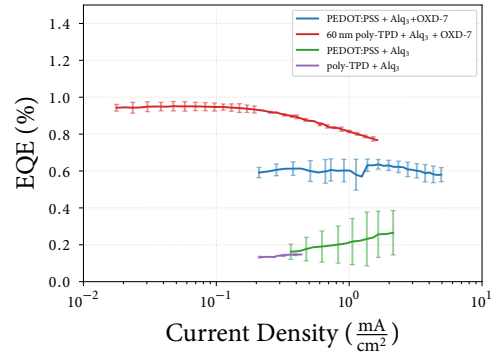
As expected, the current densities are higher for the device without poly-TPD (see Fig. 19c). The poly-TPD free device shows higher errors in luminance as well as in current density. However, the EQE is considerably higher for the device with poly-TPD as HTL. In fact it nearly reaches the maximum possible EQE for an Alq₃ device, which is presented in section 4.1. The EQE increased by a factor of 10, compared to the same device without OXD-7. This effect is weaker for the devices without poly-TPD. A factor of only 2.5 is the increase in EQE between such devices. Consequently, the poly-TPD based device, either profits from a hole blocker even more than PEDOT:PSS based device or the optical out-coupling is increased by a factor of 10. The latter case is improbable as simulations, of e.g. Ref. 92, shows, a factor of about 2 is the maximum difference in light outcoupling, when varying the HTL's thickness. So there is also a high, respectively higher, contribution of the hole-blocking ability of the OXD-7 compared to the poly-TPD free device.



(a) Schematic layer stack design of the hole blocking augmented OLED. ^{S.35}

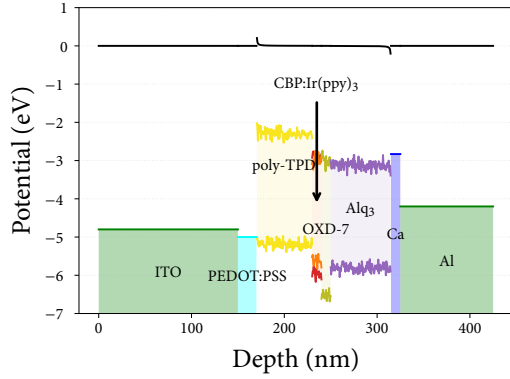


(b) Current density and luminance vs voltage plot of the prepared Alq₃ based, as well as the OXD-7 augmented OLEDs. The dashed lines represent the respective luminance. ^{S.36}

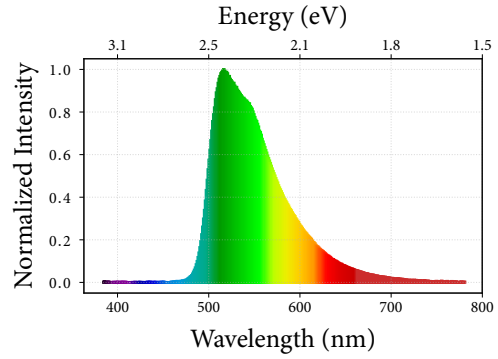


(c) EQE vs current density plot. The EQE is clipped for luminances less than $0.5 \frac{\text{cd}}{\text{m}^2}$. ^{S.36}

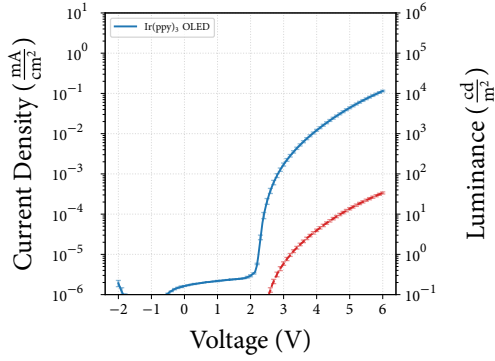
Figure 19: Characterisation of the Alq₃ based and OXD-7 augmented OLEDs. OXD-7 is introduced as a hole blocking layer. A poly-TPD free device, where PEDOT:PSS injects directly into the Alq₃, is compared to a device with an additional, 60 nm thick poly-TPD layer.



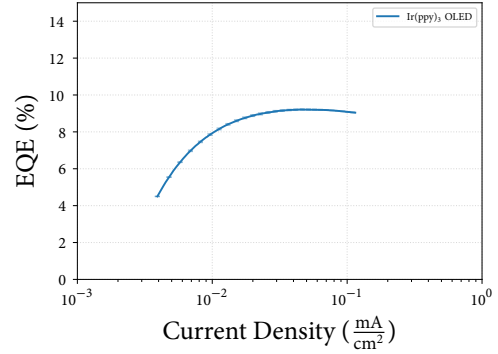
(a) Schematic layer stack design of the investigated OLEDs. [S.37](#)



(b) Electroluminescent emission spectrum of the OLED based on CBP:Ir(ppy)₃ as emitter. [S.38](#)



(c) Current density and luminance vs voltage plot of the prepared CBP:Ir(ppy)₃ based OLED. [S.39](#)



(d) EQE vs current density plot. The EQE is clipped for luminances less than 0.5 $\frac{\text{cd}}{\text{m}^2}$. [S.39](#)

Figure 20: Characterisation of the Ir(ppy)₃ based OLED.

Finally, a well performing stack design based on polymeric hole injection and hole transport layers is designed. However, to exclude any influences of the emitter material, a different emitter material is introduced in the stack. The CBP:Ir(ppy)₃ emitter system builds a high performing emission layer. The stack is shown in Fig. 20a. Considering the HOMO levels of the materials, at this point the introduction of a hole blocking material is essential, since the Alq₃'s HOMO is higher than the one of CBP. Similar cases will be present when using perovskite emitters, since their HOMOs are as low or even lower. The emission is green again, so the optical outcoupling shouldn't be altered much due to interference effects. The emission, shown in Fig. 20b, features a double-peak. This is typical for Ir(ppy)₃

emitters, the peak positions determined by triple Gaussian fits, see Fig. A.5, are located at 510 nm respectively 537 nm. The spectrum's peak positions match with the photoluminescence spectra determined by groups of Ref. 93 and 94. However, the total FWHM is broader. In fact, the sum of the higher energetic two peak partial fits is congruent with the PL spectrum. So the third emission may be again a cavity effect or a charge transfer state (CT state). The main source of emission is undoubtedly the CBP:Ir(ppy)₃ emitter. The current density through this device is comparably low as the current density in the Alq₃ based device for the same applied voltages. Thus, the charge carrier balance is assumed to be about equal for both devices (see Fig. 20c and Fig. 19b). However, the luminance is one order of magnitude higher. Consequently the EQE is one order of magnitude higher (see Fig 20d). It is not as close to the theoretical maximum EQE for the system; 9 % is about half the 18 % which can be achieved with CBP:Ir(ppy)₃-devices. At this point the absorption of the poly-TPD could become more dominant, or the HTLs and ETLs layer thickness may be adjusted for a better optical outcoupling. Both issues are, if relevant, less dominant in Alq₃ based devices, since its emission is at lower energies, where the poly-TPD absorbs fewer and the ETL can be thicker for constructive interference in the OLED cavity. Nevertheless, as a proof of concept, the devices show, that an OLED based on poly-TPD as HTL is performing well enough to test the application of new materials such as perovskites.

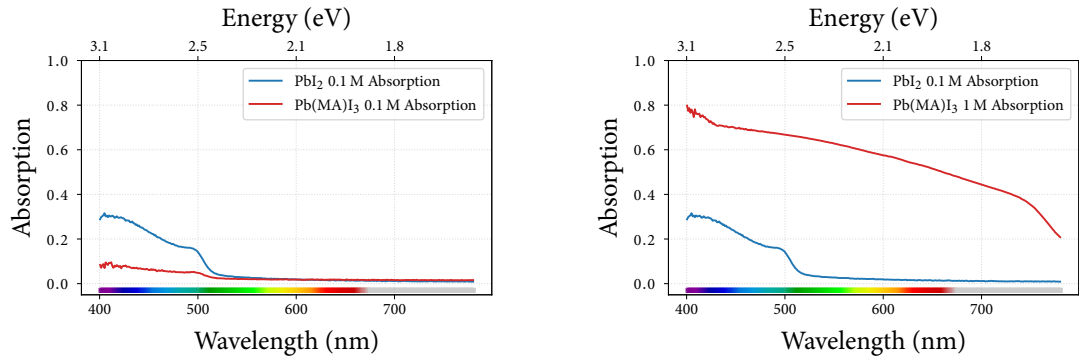
6.2 Methylammonium lead iodide-, (MA)PbI₃-perovskite

In section 3.1 the (MA)PbI₃ perovskite is already presented. In this section the (MA)PbI₃ perovskite is processed and characterised. At first the films are characterised in morphology and optical properties. After that the application of the perovskite in OLEDs is tested.

6.2.1 Properties of (MA)PbI₃-films

A (MA)PbI₃ film can be created by two established strategies. Either the precursors, that is, PbI₂ and (MA)I, are dissolved in a common solvent and the solution is spin-coated directly onto the substrate. Or the precursors are dissolved in different solvents, and spin-coated subsequently. The first is called the one-step-process, the latter the two-step-process. While the one-step-process may yield to fissures in the film due to uncontrolled crystallisation, the two-step-process may not fully crystallise to a perovskite. The two-step-process, uses the structure of the PbI₂ crystal, and the (MA)I molecules diffuse into this crystal. At that, the (MA)I may not diffuse through the whole crystal.⁹⁵

Note that all film characterisations methods are performed in ambient air. The oxygen and the ambient humidity is assumed to have low impact on the perovskite surface structure and the optical properties for the few minutes of measurement.



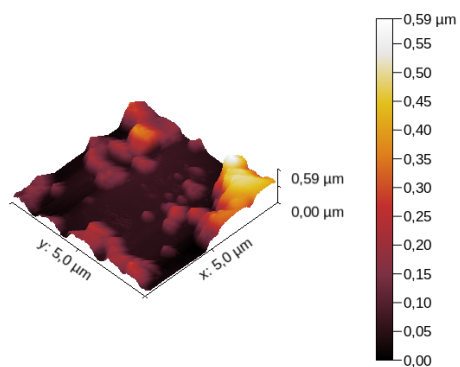
(a) Absorption spectrum a 0.1 M PbI₂: 0.1 M (MA)I in DMF solution.^{S.40} (b) Absorption spectrum a 1 M PbI₂: 1 M (MA)I in DMF solution.^{S.41}

Figure 21: Absorption spectra of PbI₂ -(MA)I solutions spin-coated on a glass substrate.

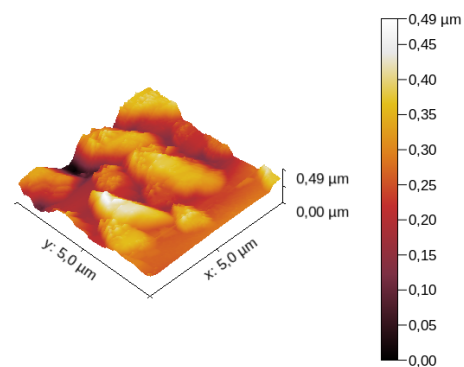
Absorption Spectrum To proof the formation of a (MA)PbI₃ perovskite, the absorption spectrum can be analysed. The (MA)PbI₃ should have a black colour,¹³ while the educts have yellow (PbI₂) and white ((MA)I) colour. So with the absorption spectrum, the formation of a perovskite is indicated by a whole visible spectrum absorption. For the reflectometry measurement the film morphology is negligible so the one-step-process is chosen. The PbI₂ is spin-coated from a 0.1 M DMF solution^f and shows absorption of blue light (see Fig. 21a). This is according to intuitive colour theory; filtering blue light from originally white light yields yellow coloured light. The (MA)PbI₃ perovskite is synthesised out of 0.1 M PbI₂ in DMF and 0.1 M (MA)I in DMF 1:1 mixture. However no additional absorption is visible for this sample. The blue absorption vanishes. The same layer with higher concentrated (MA)PbI₃ 1 M for each precursor, yields a strong absorption in the whole visible spectrum as seen in Fig. 21b. The fact, that the PbI₂ absorption vanishes and a new black absorption is created, proofs the formation of a new structure, which is without doubt the (MA)PbI₃ perovskite.

Surface Morphology The surface morphology of a (MA)PbI₃ perovskite is often very rough and holey. That's why one of the main challenges for building devices based on (MA)PbI₃ is to get smooth and hole-free films. Two important factors, determining the crystal growth tremendously, are the underground and its temperature. The AFM images of Fig. 22a and 22b are taken with a glass substrate as underground. The difference between the two is the temperature. While the glass depicted on the right was heated to 90 °C before spin-coating, the left one was left cold, that is, 20 °C. Overall, the (MA)PbI₃ build very big grains of sizes up to 0.5 micrometers in diameter. The heated sample yield a

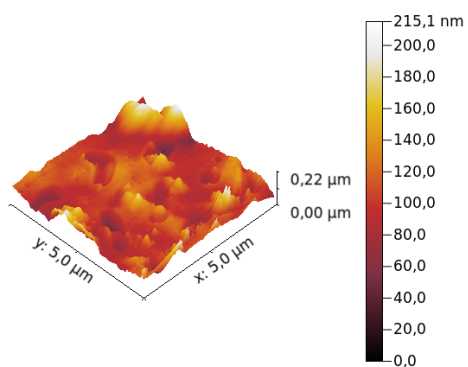
^fall samples for reflectometry measurements are spin-coated at 5000 rpm for 30 seconds on glass substrates



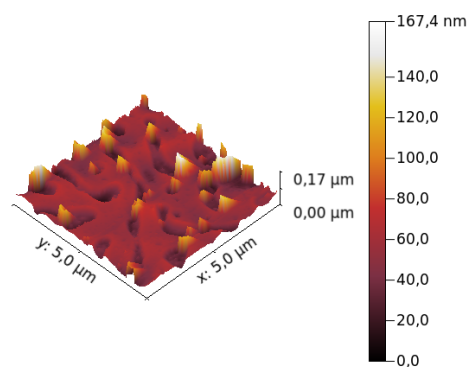
(a) Surface morphology of the spin-coating on a 20 °C warm glass substrate. ^{S.42}



(b) Surface morphology of the spin-coating on a 90 °C warm glass substrate. ^{S.43}



(c) Surface morphology of the spin-coating on a 20 °C warm poly-TPD coated substrate. ^{S.44}



(d) Surface morphology of the spin-coating on a 90 °C warm poly-TPD coated substrate. ^{S.45}

Figure 22: AFM images of 1 M PbI₂ -(MA)I DMF solutions spin-coated on different undergrounds.

much more dense distribution of the (MA)PbI₃ grains. The cold sample shows areas as big as one square micrometer, where no material is deposited. When building OLED which such film properties, high leakage currents and parasitic emissions are to expect. However the (MA)PbI₃ is not planned to be deposited on a blank glass substrate, but on poly-TPD. The already created and characterised poly-TPD layer should be the underground of the (MA)PbI₃ deposit. The (MA)PbI₃ solutions are spin-coated by depositing 50 µl of 1 M (MA)PbI₃ in DMF on the crosslinked poly-TPD and afterwards rotating at already stated standard conditions. One of the substrate is heated to 90 °C before spin-coating. The AFM images of the heated and unheated samples are shown in Fig. 22c and 22d. Grown on poly-TPD the (MA)PbI₃ builds much smoother films than on glass. The structure itself is completely different. On poly-TPD, a proper continuous film is built, just some steep valleys can be seen. While grown on glass the structure is more like big grains aligned. The temperature difference is still influencing the structure, so that the valleys become thinner and less deep when depositing on a pre-heated underground. On another attempt the temperature was even increased, to achieve a completely closed layer. Unfortunately the perovskite structure is irreversibly destroyed at higher temperatures than 100 °C, which can be seen by a dramatic colour change from black to a brownish yellow. When cooling down the black colour does not return, so this has to be more than just a phase transition. At that, probably some perovskite-constituent is evaporated.

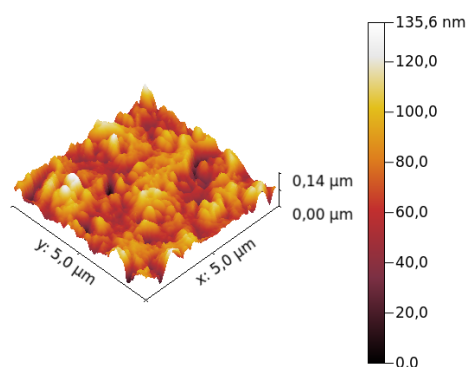


Figure 23: Surface morphology of the spin-coating on a 90 °C warm poly-TPD- PbI₂ coated substrate. Small crystals seems to grow everywhere. Peak and rifts are no longer observable. The PbI₂ doping may provide omnipresent crystallisation germs.^{S.46}

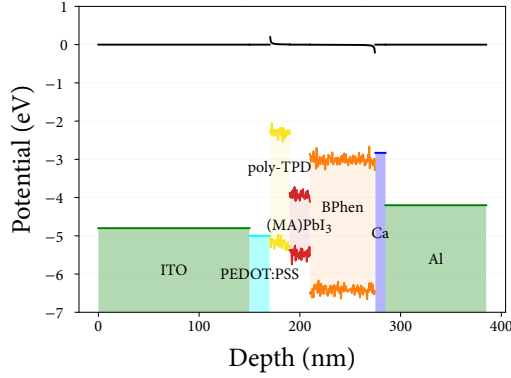
Another sample was created, where on top of the already existing poly-TPD layer a mixture of poly-TPD and PbI₂ was deposited. The purpose of mixing PbI₂ into the polymer is to provide some crystallisation germs, so that the valleys seen in Fig. 22d are closed by newly grown crystals inside. Since the valleys can be seen on a micrometer scale, the concentration of PbI₂ can be very small. With a 1 % wt of PbI₂ in poly-TPD there should be enough crystallisation germ spots inside such a valley. The solution is created by dissolving 1.5 mg poly-TPD in 936 µl chlorobenzene and adding a solution of 0.15 mg PbI₂ in 32 µl DMF. This solution is spin-coated and dried at standard conditions. With the (MA)PbI₃ spin-coated on top the structure changes tremendously (see Fig. 23). The flat areas are gone completely. So are the valleys. However the layer itself has fewer high rising

peaks. Many small grains are visible, so the structure suggests, that the theory of providing crystallisation germs will close the valleys. Additionally, the flat areas are gone. For application in PeLEDs this film may be suitable, but the underground could give rise to high leakage currents. That's because the influence of PbI₂ is unknown, but the lead ions will probably increase the conductivity.

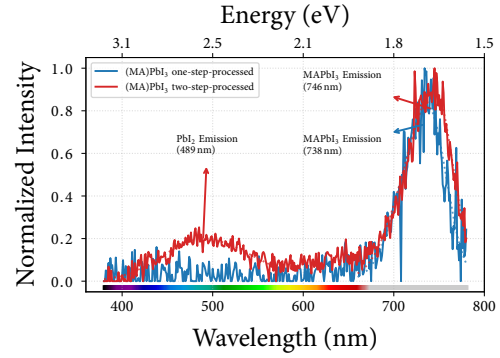
6.2.2 Properties of (MA)PbI₃-based LEDs

For creating OLEDs based on (MA)PbI₃ as emitter, the same hole injection layers as already characterised for previous devices is used. On top of them, the (MA)PbI₃ perovskite is deposited. Since the absorption is not favourable for LEDs the perovskite is deposited thinner. Therefore the 0.1 M solutions are used. The (MA)PbI₃ layer thickness can not be determined, because the surface is too rough and a clear step for thickness determination with profilometer or AFM is not visible. Nevertheless, from AFM images and valleys depths, one can estimate the layer thickness to be smaller than 100 nm for the 1 M solution. For a proof of concept the thickness is not important. There has been a problem with the purity of Alq₃ deposited films during the time of the device fabrication, so BPhen was used as ETL. The whole stack design with an estimated (MA)PbI₃ layer thickness is illustrated in Fig. 24a. The (MA)PbI₃'s VBM and CBM values are taken from Ref. 96. The one-step process is already explained, that is, the spin-coating of 50 µl (MA)PbI₃ solution. For the two-step process 50 µl PbI₂ 0.1 M in DMF is spin-coated at standard conditions. After that the PbI₂ layer is soaked with (MA)I, dissolved in isopropyl alcohol 0.1 M, for 5 seconds and subsequently rotated on the spin coater at standard conditions. The (MA)I is solved in isopropyl alcohol, because isopropyl alcohol is not dissolving the existing PbI₂ layer.

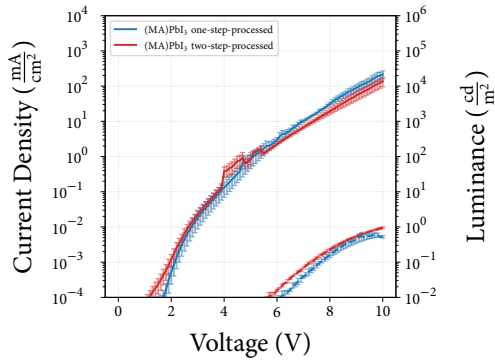
The device emits light, as expected, at wavelengths 734-739 nm (see A.6). A near infrared emission is reported by groups of references 22 and 97. But their reported EL and PL emission is at wavelengths higher than 780 nm; at this wavelength the spectrometer reaches its limit. So the spectrum and consequently the EQE may be flawed. The two step processed device's emission shows an additional broad emission at 508 nm. Considering the absorption of PbI₂ and assuming a mediocre stokes shift this emission could arise from residual PbI₂. Residual PbI₂ is more probable to be present in the two step processed film, as the (MA)I may not have diffused through the whole PbI₂ film to form a perovskite. The current densities are comparable to the already characterised Alq₃ based devices (see Fig. 24c). However, the luminances are orders of magnitude lower. That is not a surprising fact, since the luminance is defined with the photopic luminosity function, which takes very low values in the near infrared. Nevertheless the EQE is very low (see Fig. 24d). The EQE of the one-step-processed device would, like the two-step-processed devices, also be smaller than 10⁻⁴. The noise in the range of 400-600 nm has a higher contribution to the EQE than the actual emission peak. So an adjusted spectrum has been used for calculation of the EQE of the one-step-processed device. This spectrum is composed of zeros



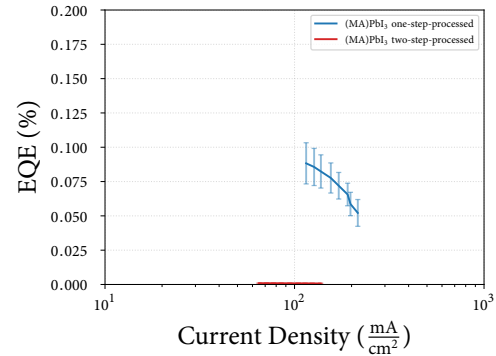
(a) Schematic layer stack design of the proof of concept (MA)PbI₃ OLEDs. ^{S.47}



(b) Electroluminescent emission spectrum of the OLED based on (MA)PbI₃ as emitter. ^{S.48}



(c) Current density and luminance vs voltage plot of the prepared (MA)PbI₃ based OLEDs. The dashed lines represent the respective luminance. Note that luminances are very low as the emission is nearly in the infrared. ^{S.49}



(d) EQE vs current density plot. The EQE is clipped for luminances less than 0.5 $\frac{\text{cd}}{\text{m}^2}$. For the EQE an adjusted spectrum is used (see Ref A.7). ^{S.49}

Figure 24: Characterisation of the (MA)PbI₃ based LEDs. Two devices are investigated where the two different deposition techniques are used. The devices are not optically optimised, furthermore the poly-TPD is not compatible with the solvent DMF. The devices are just a proof of concept.

and the peak data obtained by a fit. The spectrum is shown in Fig. A.7. The two-step-processed EQE is determined by the parasitic emission at 500 nm, the actual emission is unfortunately negligible. So even a noise-cleaned spectrum wouldn't change the EQE to the same extent. At this point it should be remembered that even the adjusted spectrum is flawed, as the spectrum is not obtained properly, because of the spectrometer working at the upper limit. The further the spectrum is in the infrared, the higher the EQE could be. For estimating a lower EQE limit the present data suffices. The data shows proof of concept, that a solution processed (MA)PbI₃ based PeLED can be created with the given precursors. Further investigation on this perovskite would require instruments, characterising IR radiation. When exchanging the halide of the perovskite by using the Bromide instead of Iodine, the emission will be visible (green) and easier to characterise.²²

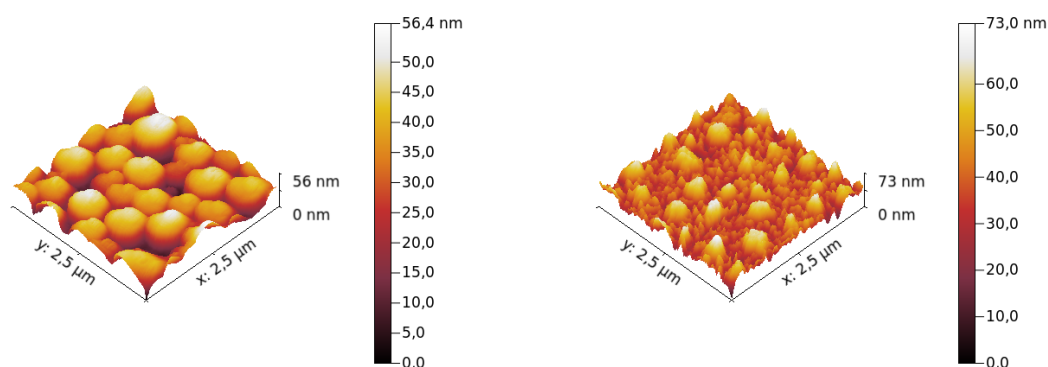
6.3 Caesium lead bromide-, CsPbBr_3 -perovskite based quantum dots

The CsPbBr_3 perovskite is bromide based. Furthermore the organic ion is replaced with a caesium ion. With the according precursors quantum dots can be synthesised. The CsPbBr_3 perovskite quantum dots are not manufactured at the University of Augsburg, but by Matthew Jurow of University of Berkeley.⁸ They are provided in toluene solution for spin-coating. For further reading about the synthesis refer to the supporting information of his paper (Ref. 17).

6.3.1 Properties of CsPbBr_3 -films

The optical properties of the CsPbBr_3 film have already been well investigated by the group of University of Berkeley (also part of Ref. 17). So the structural properties of the film is yet to be investigated. For OLEDs a closed layer of quantum dots is favourable. Ideal for the LEDs is a monolayer-array of CsPbBr_3 quantum dots, since then there are no spots where ETL touches the HTL, leading to possible parasitic emission or non-radiative exciton decay. At that, if there are more than one layers stacked, the conductivity will decrease dramatically. To gain insight on this matter, the layers are investigated with an AFM. Several different rotation speeds for spin coating are tested. The spin coating procedure is again the already introduced standard procedure. Just the heating step is omitted, as the quantum dots are destroyed at elevated temperatures. When spin-coated on glass, the layer consist of big grains, which are several times bigger than the quantum dots. The quantum dots are cubic and about 12 nm wide.¹⁷ On Fig. 25a the visible grains are about ten times bigger. These may be some agglomerated quantum dots. When spin coating faster the big grains gradually vanish. Considering Fig. 25b, there are smaller grains and smaller structures become visible. The images show, that there is more than a monolayer of CsPbBr_3 quantum dots built. The higher spin-coating speed yields a layer with smaller agglomerates. Apart from that, the CsPbBr_3 layer on glass only gave a overview on spin-coating properties. For

⁸particularly: Molecular Foundry at the Lawrence Berkeley National Laboratory

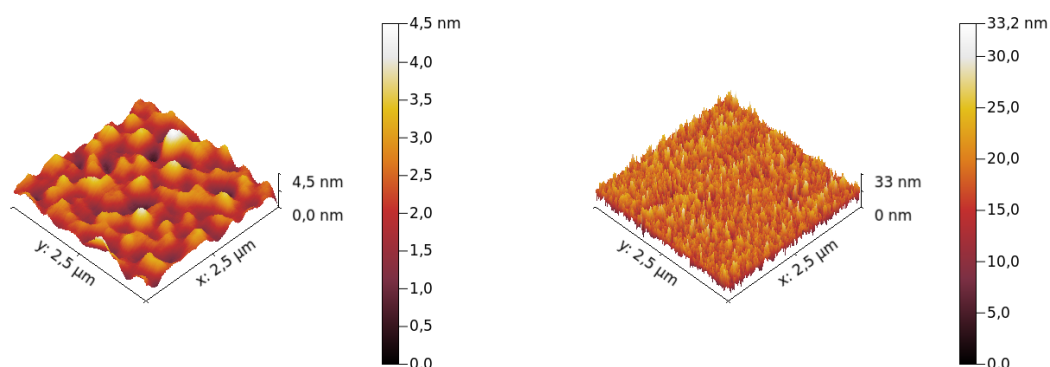


(a) Surface morphology of a CsPbBr_3 quantum dots solution spin-coated at 1500 rpm on a glass substrate. ^{S.50}

(b) Surface morphology of a CsPbBr_3 quantum dots solution spin-coated at 5000 rpm on a glass substrate. ^{S.51}

Figure 25: AFM images of CsPbBr_3 quantum dot solutions spin-coated on glass substrate.

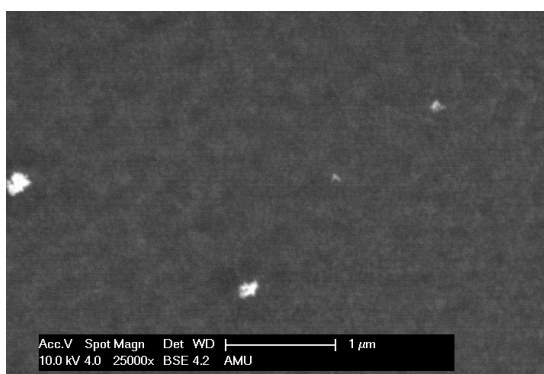
perovskite based quantum dot light emitting diodes (PeQDLEDs), the CsPbBr_3 layer on poly-TPD is of interest. Very surprisingly, the layer looks completely gone in the AFM images (see Fig. 26a). The height of the quantum dots are also about 12 nm, so not a single quantum dot's full height is visible on the image. First thoughts, that the layer was washed away by too high spin-coating speeds, can be immediately abandoned, by the fact, that the film still has a very greenish colour. PeQDLEDs built on exactly that layer show emission of the expected very characteristic wavelengths. Consequently, the quantum dots are still present. The only possibility left is, that the quantum dots are incorporated into the poly-TPD, even though the poly-TPD was cross-linked properly. With that, the toluene has to at least bloat the poly-TPD or modify it in some way, that the quantum dot can diffuse into it somehow. High quality SEM images show that there are fissures formed, and the quantum dots accumulate in these fissures. To verify such behaviour a very solvent resistant layer, the PMMA, is used as underground. On PMMA the quantum dots are again evenly distributed, there are up to a triple layer of quantum dots visible. The SEM (see Fig. 27) images show the same property. However, the back scattered electrons yield a element-wise resolution. The difference between carbon, nitrogen and hydrogen and caesium lead and bromide are quite high. So the white areas, spots are quantum dots, which is another proof, that they are still present on the poly-TPD. Some areas are dark, there are fewer quantum dots incorporated, may be because lower fissure density. Compared with the PMMA layer SEM image, there are more height steps visible. To further investigate the incorporation of the CsPbBr_3 quantum dots into the poly-TPD, it is tried to re-bloat the poly-TPD, respectively it is tried to wash out the Incorporated quantum dots out of the poly-TPD. The idea is, to soak the whole CsPbBr_3 layer in toluene, its original solvent, again. However, this time the wet layer is dried without rotation of the spin-coater. Like that, some incorporated quantum dots should be re-solved in toluene and afterwards de-



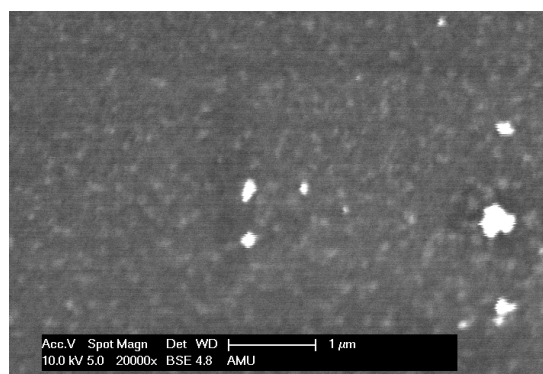
(a) Surface morphology of a CsPbBr_3 quantum dots solution spin-coated at 5000 rpm on a poly-TPD coated substrate. ^{S.52}

(b) Surface morphology of a CsPbBr_3 quantum dots solution spin-coated at 5000 rpm on a PMMA coated substrate. ^{S.53}

Figure 26: AFM images of CsPbBr_3 quantum dot solutions spin-coated on organic layers.



(a) SEM image of a CsPbBr_3 quantum dots solution spin-coated at 5000 rpm on a poly-TPD coated substrate. ^{S.54}



(b) SEM image of a CsPbBr_3 quantum dots solution spin-coated at 5000 rpm on a PMMA coated substrate. ^{S.55}

Figure 27: SEM images of CsPbBr_3 quantum dot solutions spin-coated on organic layers.

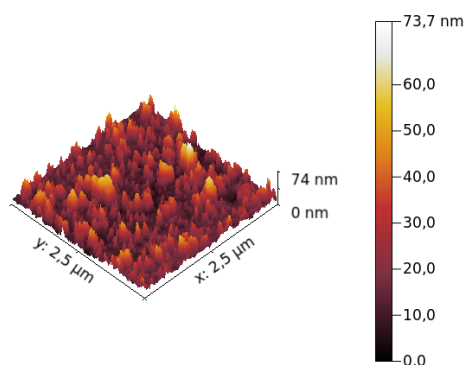


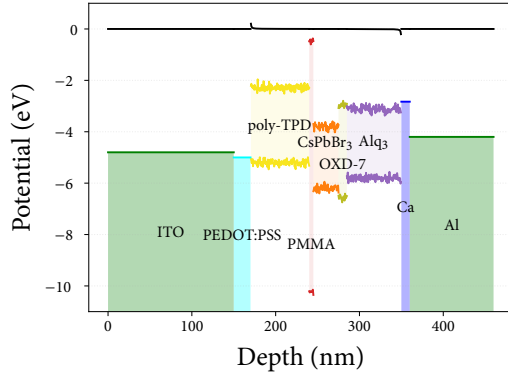
Figure 28: Surface morphology of the sample of Fig. 26a after a 30 second toluene treatment. The structure resembles more the one of the quantum dots deposited on PMMA. The quantum dots seem to be washed out of the poly-TPD.^{S.56}

posited on top of the poly-TPD without incorporation. As shown in Fig. 28, the quantum dots are visible on the poly-TPD layer. In fact the structure resembles that of the PMMA based sample. With additional research it is shown that a toluene treated poly-TPD layer shows neither a significant change in structure or thickness on the AFM images.^h An AFM with higher resolution may give images that are able to detect significant differences. The incorporation of the quantum dots into the HTL can be a significant advantage. That is, that the hole injection is greatly increased and the total layer has become very smooth which prevents short cuts through any sharp peaks. On the other side, if the CsPbBr_3 quantum dots diffuse to deep into the layer, they may reach the PEDOT:PSS or even the ITO. At that point a quenching process can reduce efficiency. Additionally, the PEDOT:PSS may react with the quantum dots, since the acidity and any residual water is no longer shielded appropriately.

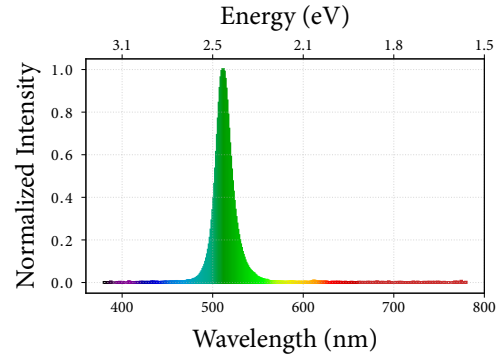
6.3.2 Properties of CsPbBr_3 -based LEDs

For building LEDs based on the CsPbBr_3 perovskite the HTL-ETL system, which has shown an appropriate performance with $\text{CBP}:\text{Ir}(\text{ppy})_3$, is used. So the HIL/HTL is built by PEDOT:PSS and poly-TPD and the electron transport is performed by the Alq_3 -OXD7 combination. With the different film properties of CsPbBr_3 quantum dots on poly-TPD and PMMA in mind, the PeLED is extended with a 5 nm PMMA layer (see Fig. 29a). Like that, the current is slightly impaired, which has to tunnel through the layer, while the CsPbBr_3 quantum dots are hindered from diffusing into the poly-TPD layer. The EL spectrum matches the PL and EL spectra of references 1 and 15 with an error of ± 5 nm. At that, the EL spectrum doesn't change considerably, when using PMMA as interlayer. The peak position at 511 nm is slightly tighter than the peaks of the references, that is, a FWHM of 18 nm (85 meV) while references show FWHMs of about 25 nm. However as shown in Fig. A.8, the peak is fitted with two gaussians, where one has the a FWHM of 14 nm. The second gaussian is broader (FWHM of 32 nm). It may arise from cavity

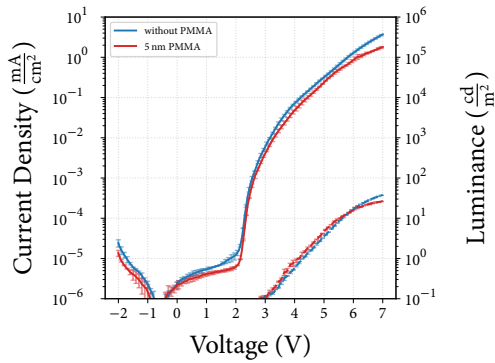
^hThey yield about the same roughness and structure as depicted in Fig. 16c and Fig. 16d; they can be reviewed in Ref. S.57



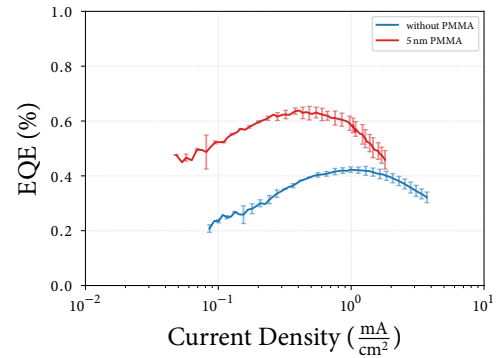
(a) Schematic layer stack design of the CsPbBr_3 OLED. The PMMA is omitted in one device. ^{S.58}



(b) Electroluminescent emission spectrum of the OLED based on CsPbBr_3 as emitter. ^{S.59}

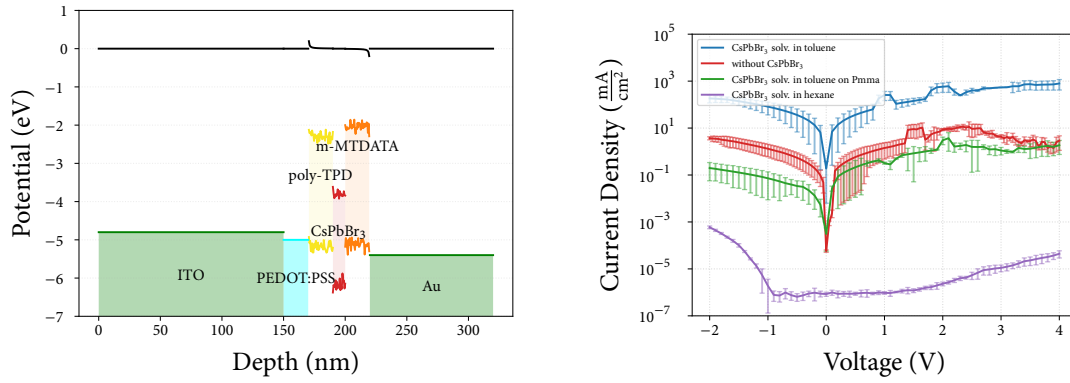


(c) Current density and Luminance vs voltage plot of the prepared CsPbBr_3 based LEDs. The dashed lines represent the respective luminance. ^{S.60}



(d) EQE vs current density plot. The EQE is clipped for luminances less than $0.5 \frac{\text{cd}}{\text{m}^2}$. ^{S.60}

Figure 29: Characterisation of the CsPbBr_3 based OLEDs. Two devices are investigated, where one has 5 nm PMMA on top of the poly-TPD. The devices are under-performing and not even close to reaching their theoretical maximum EQE.

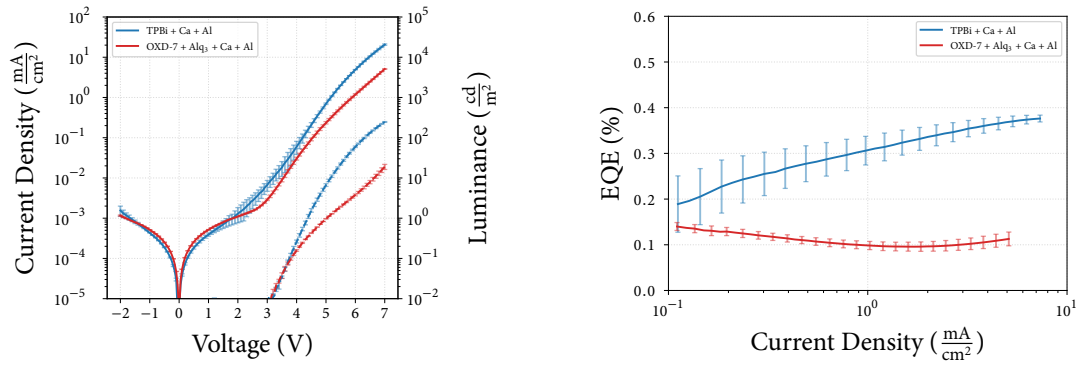


(a) Schematic layer stack design of the CsPbBr_3 based hole-only devices. The PMMA is added in one device.^{S.61} (b) Current density vs voltage plot of the prepared CsPbBr_3 based hole-only devices.^{S.62}

Figure 30: Characterisation of the CsPbBr_3 based hole only devices.

or interference effects. Photoluminescence measurements may give more information on this matter. Despite this small deviances, the spectrum can be indeed identified as a very pure CsPbBr_3 emission spectrum. The other layers are not visible in the EL spectrum. The current densities are decreased, when PMMA is introduced, while the luminances are about the same (see Fig. 29c). Consequently, the EQE is increased. For this OLED the poly-TPD was heated at 175 °C for better crosslinking. CsPbBr_3 LEDs, without PMMA as interlayer, heated only at 130 °C show a maximum EQE of 0.2 %, for example the device shown in Fig. 31. While in Fig. 29d the PMMA-free device shows a maximum EQE of 0.4 %. With PMMA as interlayer the maximum EQE is increased by a factor of 1.5 to 0.6 %. So overall the PMMA improves the device's efficiency. The reason might be, that the CsPbBr_3 quantum dots are better separated from the PEDOT:PSS respectively the ITO anode, where excitons might quench. Devices were created, where the poly-TPD is applied twice, so the device has a thicker poly-TPD layer. The EQE increased as well, but not as strongly, which may be impaired by the counteracting interference effects, as the cavity size increases. However, separating the CsPbBr_3 from anode via thicker layers or insulators as PMMA increases EQE. For understanding the processes of hole transport in the PEDOT:PSS and poly-TPD, a device where the only charge carriers are holes is designed. Such hole-only devices give information on the hole transport properties of the layers. These devices are not emitting light, as there are no electrons to form excitons. In order to turn an OLED into a hole-only device, the electron injection and transport layers are switched with additional hole injecting ones. As the CsPbBr_3 is not crosslinked these layers should not be solution processed, but evaporated. The introduced material m-MTDATA (see Fig. 7b) has an appropriate HOMO for hole transport. Even the cathode has to be switched, since aluminium's workfunktion is too high. Gold is a more noble

metal, so its workfunction is lower (about -5.4 eV).⁵⁴ The stack design is illustrated in Fig. 30a. The devices showed no luminance, if there were one, this wouldn't be real hole-only devices. So the luminance is omitted in Fig. 30b. Four devices are tested. One device is fabricated without spin-coating the CsPbBr_3 quantum dots, and one has an additional PMMA layer as interlayer. Additionally some CsPbBr_3 quantum dots are received and spin coated in a hexane solution. The most astonishing feature of the current density vs voltage plot is, that the device without the CsPbBr_3 quantum dots shows currents two orders of magnitude smaller than the device with toluene based CsPbBr_3 dots spin-coated on top. This is not possible when assuming two completely and cleanly separated layers, because the CsPbBr_3 layer's resistance would be negative in that case. The only possible solution is, that the CsPbBr_3 quantum dots increase the conductivity of the poly-TPD layer. When considering the AFM and SEM image, this scenario is very plausible. The quantum dots, or parts of it, may have diffused into the layer, increasing the conductivity. Additionally, when shielding the poly-TPD layer with PMMA, the conductivity is below the poly-TPD's. This supports the theory of hindering CsPbBr_3 incorporation into the poly-TPD layer. However, when spin-coating the CsPbBr_3 in hexane, this effect is gone completely. Furthermore, the hexane based CsPbBr_3 shows very high resistance. The onset at -1 V shows that hole injection from m-MTDATA is better than it is from poly-TPD. Though, this asymmetry should also be present in the other devices. Maybe the m-MTDATA layer is not closed, so that the currents from gold directly onto CsPbBr_3 or poly-TPD are dominant. With the hole-only devices, the hole injection is identified to be quite good. On the other side the electron injection layer can be altered to get information indirectly.



(a) Current density and luminance vs voltage plot of the prepared CsPbBr_3 based LEDs. The dashed lines represent the respective luminance.^{S.63}

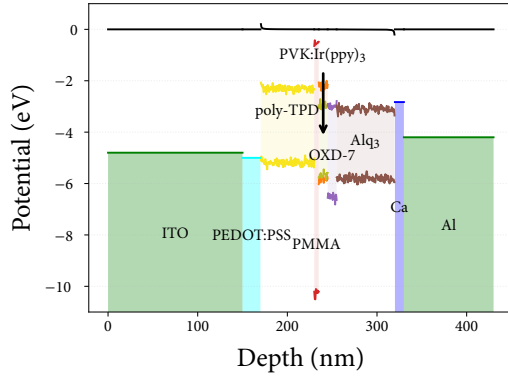
(b) EQE vs current density plot. The EQE is clipped for luminances less than $0.5 \frac{\text{cd}}{\text{m}^2}$.^{S.63}

Figure 31: Characterisation of the CsPbBr_3 based OLEDs.

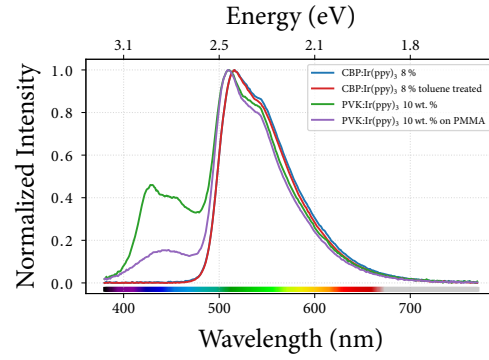
When using a better electron injection material, like TPBi, the EQE is further increased.

The currents are higher than in the OXD-7 based device. Higher currents mean that a higher amount of charge carriers are injected. At the same time the luminance is increased over-proportionally. So there are more radiative excitons built. The only influence of an ETL on the hole injection, is by its dipole moment. A high dipole moment results in facilitated hole injection. However, this dipole moment and interfacial charge is higher for OXD-7 and Alq_3 than it is for TPBi.^{98, 99} So the TPBi should if at all worsen hole injection. The only possibility left is, that an increased electron injection increases EQE. For a device with the same emitter and the same optical outcoupling, only the charge carrier balance is altered. So an increased electron injection improving EQE can only state, that there is an hole abundance. At that, the internal quantum efficiency is assumed to be equal. Concluding, the device is not limited by bad hole injection which is further supporting the theory suggested by the hole only device, that the hole injection is indeed very good, due to the incorporation of the toluene solved CsPbBr_3 quantum dots. The devices shown in Fig. 31, are low on EQE compared to the previous devices because the poly-TPD was only heated at 130 °C. This is because at that state of research the improval of EQE in hotter crosslinked poly-TPD has not yet discovered.

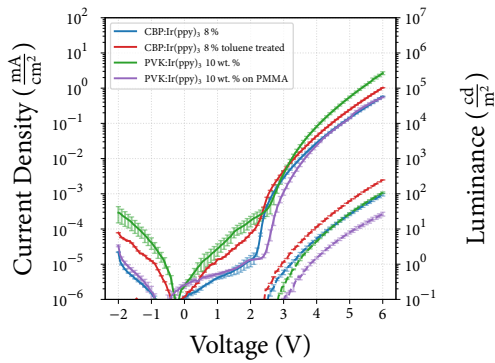
When considering the AFM/SEM images and the LEDs fabricated with toluene based quantum dot solutions, the toluene may be identified as the cause of the issues. That is because the toluene based solutions strongly influence the hole injection and transport layers. With hexane based solution there is no such influence. So the toluene-poly-TPD interaction is tested in absence of the quantum dots. For that, the Ir(ppy)_3 devices are used. One device is created like the previously discussed CBP:Ir(ppy)_3 device (shown in Fig. 20), but with 175 °C heated poly-TPD. The same device is created but prior to evaporation of the CBP:Ir(ppy)_3 the poly-TPD is soaked in toluene for 30 seconds, and residual toluene is removed by spinning the sample at standard conditions. Additionally, solution processed emitter based on PVK:Ir(ppy)_3 is used instead of the CBP:Ir(ppy)_3 . Therefore the PVK and the Ir(ppy)_3 is solved in toluene. A mixed solution of 10 wt. % Ir(ppy)_3 in PVK is created. This is spin-coated at standard conditions. One device is augmented with PMMA to isolate the poly-TPD from toluene, just like in the CsPbBr_3 based devices. The complete stack design of such device is shown in Fig. 32a. The emission spectrum of CBP based devices is as expected the same as in the previous devices. However, with PVK, there is an additional blue emission. Without PMMA there are two additional peaks at 450 nm and 431 nm, while with PMMA only the 450 nm peak is left (see Fig. A.9). So the peak at 431 nm has to originate from poly-TPD somehow, because when isolated it is gone. In fact, the emission matches the photoluminescence of poly-TPD, reported by Ref. 100, very well. So there is a electron injection into the poly-TPD, which has not been observed in any device. Thus, the PVK's LUMO may be too high for performing well with poly-TPD as hole transport layer. The 450 nm peak cannot be identified as PVK, its PL emission peak is at wavelengths lower than 420 nm.¹⁰¹ This may be a OXD-7-PVK exciplex state, since the LUMO-HOMO difference, 2.8 eV, that is 443 nm subtracted by some exciton binding energy, would be fitting. When considering the current densities of the



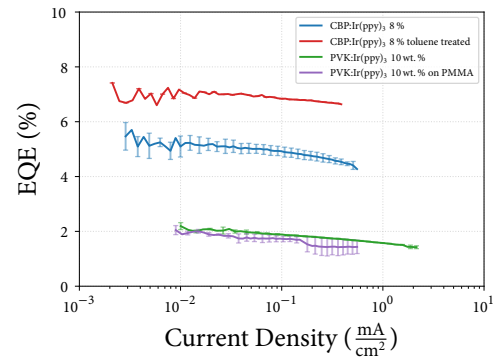
(a) Schematic layer stack design of the PVK:Ir(ppy)₃ OLED. The PMMA is omitted in one device. ^{S.64}



(b) Electroluminescent emission spectrum of the OLED based on Ir(ppy)₃ as emitter. The PVK based device shows an additional emission. ^{S.65}



(c) Current density and luminance vs voltage plot of the prepared Ir(ppy)₃ based OLEDs. The dashed lines represent the respective luminance. ^{S.66}

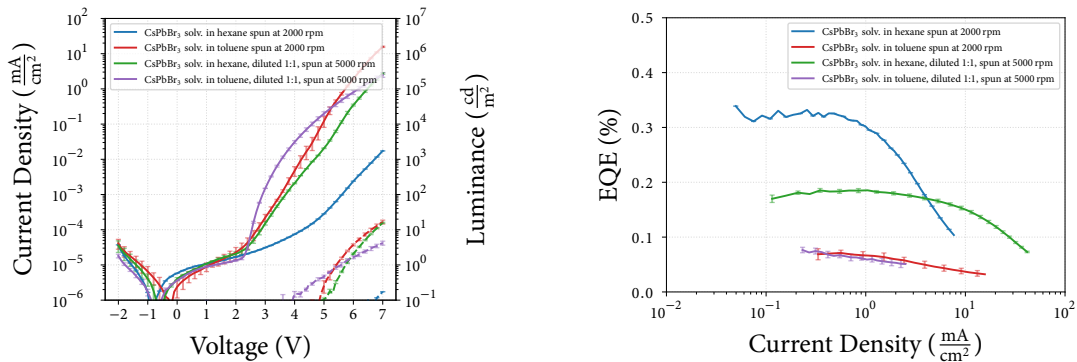


(d) EQE vs current density plot. The EQE is clipped for luminances less than 0.5 $\frac{\text{cd}}{\text{m}^2}$. ^{S.66}

Figure 32: Characterisation of the PVK:Ir(ppy)₃ based OLEDs.

devices (see Fig. 32c), it can be derived, that the devices where the poly-TPD is directly in contact with toluene show increased ones, with respect to their PMMA shielded or non-treated counterpart. So an increased current through poly-TPD is not only caused by the CsPbBr_3 quantum dots, but also by the solvent treatment itself. The respective EQEs show a surprising behaviour (see Fig. 32d). The EQEs are lower than the previously manufactured devices, which may be due to the higher temperature crosslinking, which may alter the molecular orbital state energies (HOMO or LUMO). The interesting point is, that the toluene increases the EQE to be nearly as high as it is for the device with 130 °C heating treatment (see Fig. 20d). So for this device the toluene treatment is not the reason for impaired EQE, quite the contrary, it increased it. The PVK based device show a smaller effect, but this could be due to altered emission spectra. The EQE is very sensitive, so a slightly altered spectra has massive influence on the resulting EQE, so at this point the EQE comparison has little significance. Still, the total EQE of the solution processed devices (PVK:Ir(ppy)₃), is about a order of magnitude higher than for the CsPbBr_3 devices, even though toluene is used as solvents for both. With this devices it is shown, that the problem of low EQE in CsPbBr_3 devices can not arise exclusively from the toluene, but more the combination of CsPbBr_3 dissolved in toluene. Maybe it is CsPbBr_3 itself, and the toluene has little to no influence. Or to the contrary toluene could even increase EQE like it is the case for the Ir(ppy)₃ based devices.

To validate this hypothesis, the hexane based CsPbBr_3 solution is used to create LEDs.



(a) Current density and luminance vs voltage plot of the prepared CsPbBr_3 based LEDs. The dashed lines represent the respective luminance.^{S.67}

(b) EQE vs current density plot. The EQE is clipped for luminances less than 0.5 $\frac{\text{cd}}{\text{m}^2}$.^{S.67}

Figure 33: Characterisation of the CsPbBr_3 based OLEDs.

Small scale test showed that hexane treatment has no influence on poly-TPD at all. This is not a surprising circumstance, because poly-TPD is not even soluble in hexane when not crosslinked. Hence, devices are created in the same stack design as depicted in Fig. 29a,

but without PMMA. To get different layer thicknesses the spin coating procedure and the solutions concentrations has been adjusted, as explained in the labels of the graphs (see Fig. 33). The best hole injection is present in the thinnest toluene based device. This is indicated by the sharp onset. When increasing the thickness it gets worse, but still better than the thin hexane based devices. The same trend is observable among the hexane based devices. However, the EQE of the hexane based LEDs is higher. The spectra are all congruent and equal to the already measured spectra shown in Fig. 29b. The EQE of toluene based reference device (5000 rpm 1:1 diluted) is smaller than the already measured for the same device. This may arise by the circumstance, that for these devices a different batch of solution was used, which may have poorer quality. The poorer solutions quality is observed as a yellowish taint. However, since all solution showed the same slightly visible taint, the relative comparison should still be valid.

7 Outlook and Summary

In this thesis, the use of poly-TPD in organic light emitting diodes is demonstrated. When using appropriate emitter material, the theoretical maximum EQE are nearly reached. One of the drawbacks of poly-TPD is its absorption in blue visible range. Hence the use of poly-TPD in blue OLEDs is problematic, while green and red OLEDs won't be impaired significantly. Another challenge is the solvent's influence on poly-TPD; the reason for introducing this polymeric HTL is to get rid of issues arising from solution processing. However, poly-TPD shows a sensitivity to DMF and toluene solved CsPbBr₃ quantum dots.

Furthermore, in this document the successful synthesis of (MA)PbI₃ perovskite through two different processes has been shown. The incorporation of this perovskite into a prepared OLED stack succeeds, even though it shows poor performance. This issue is ascribed to the proven solvent susceptibility. The further research on (MA)PbI₃ is cancelled, since its emission is at the edge of the visible light to near infrared, where present measurement devices lack effectiveness. A research on the similar perovskite (MA)PbBr₃, should be easier since its emission is expected to be green which is easier to characterise. However, even when using the (MA)PbBr₃ perovskite the solvent DMF has to be exchanged to a non damaging solvent, or the poly-TPD has to be replaced by a tougher polymer, for getting at least mediocre efficiencies. The other group of perovskite, which is present as quantum dots, the CsPbBr₃, turns out to struggle with similar problems. Even though the photoluminescence quantum yields are very high, the expected high EQEs could not be reached yet. However, several ways for improvements has been shown. The EQE has been increased by a factor of 1.5 by using PMMA as shielding layer. It could be further increased by using TPBi by a factor of about 3. And when using the hexane based solution an additional improvement factor of 4 is shown. Assuming these effects stack, there is a potential EQE of $0.4\% \cdot 1.5 \cdot 3 \cdot 4 = 7.2\%$. This EQE is near the maximum possible, when considering the bad optical outcoupling, due to the vertical emitter orientation showed by Jurow et al.¹⁷. With that, the key parameters to improve the CsPbBr₃ quantum dot based LEDs are the solvents influence on the HTL and the emitter orientation. While there may be a suitable material-solvent pair for optimal hole injection, the emitters orientation cannot be changed easily. The orientation turns out to be field dependent, so the present OLED stack design will always yield a bad orientation. To solve this problem a new device design, where the light emission is perpendicular to the applied field would be necessary for optimal optical outcoupling. Nevertheless, the development of a suitable solution processed HTL system for solution processed emitters, appears to be an important matter. With further research, suitable polymer combinations may be able to handle solvents like DMSO, DMF and toluene without impairing the efficiency. On the other side more compatible

solvents can probably used for the deposition of the perovskites.

8 Appendix

8.1 Additional Figures

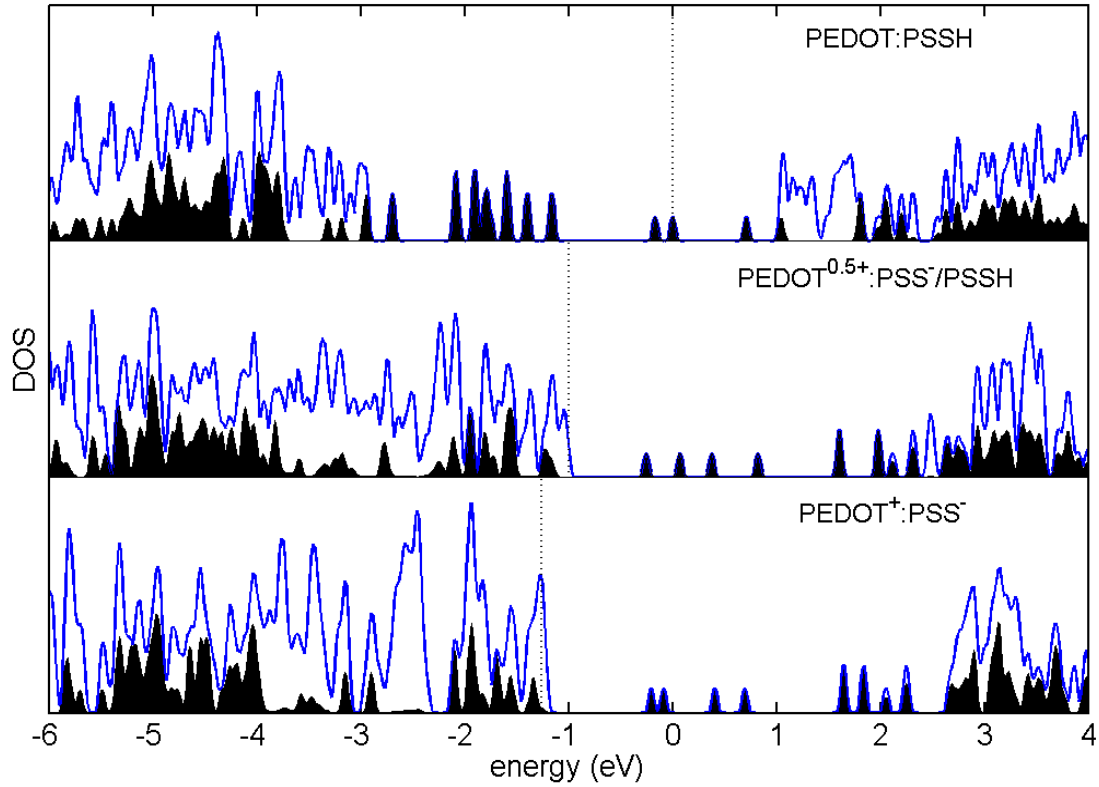


Figure A.1: Density of states of PEDOT:PSS.³⁸ The HOMO is approximately obtainable, but the LUMO is because of the states between -1 eV and 2 eV not certainly determinable. The filled areas represent the partial DOS of PEDOT, while the blue line is the total DOS (with PSS).

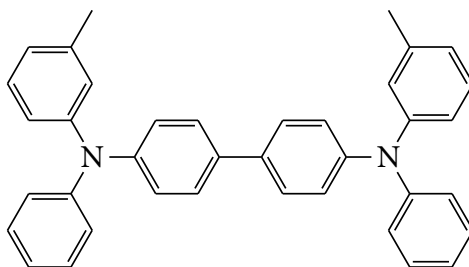
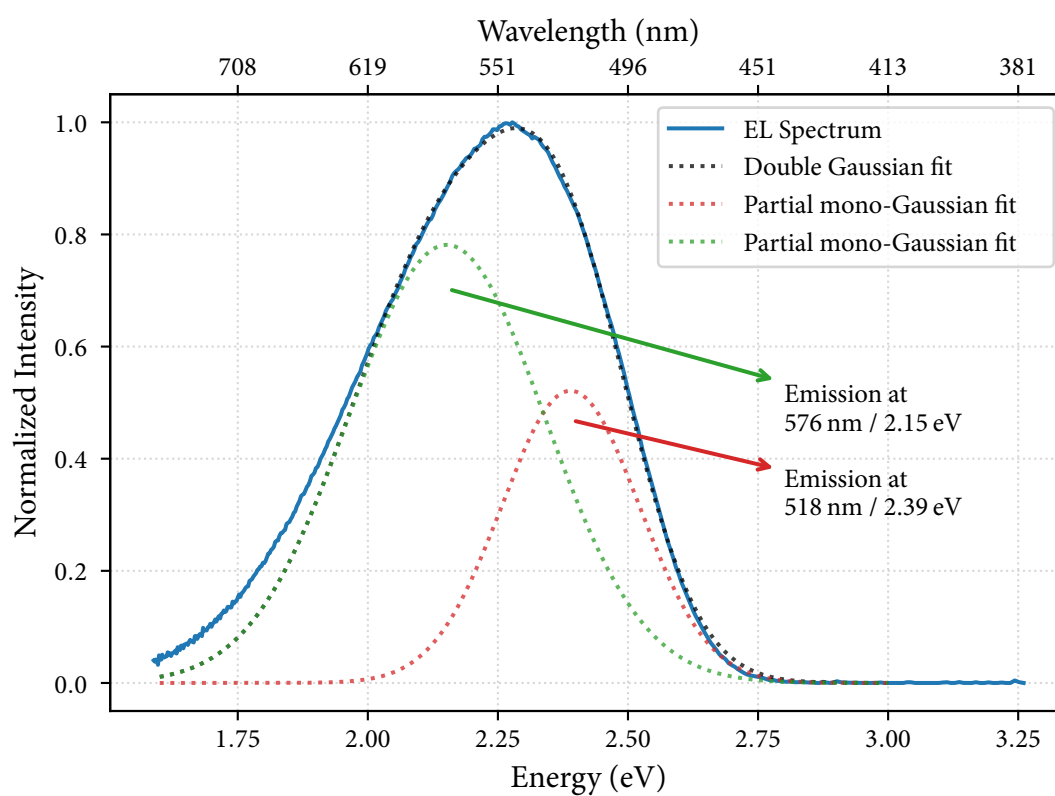
Figure A.2: Lewis structure formula of TPD^{S.68, 102}

Figure A.3: Double Gaussian fit on an Alq₃-NPB based EL spectrum. The red curve is identified to be Alq₃, while the green is probably an exciplex between Alq₃ and NPB. The fits differ from data below 2.0 eV, which may be caused by another additional emission.^{S.33}

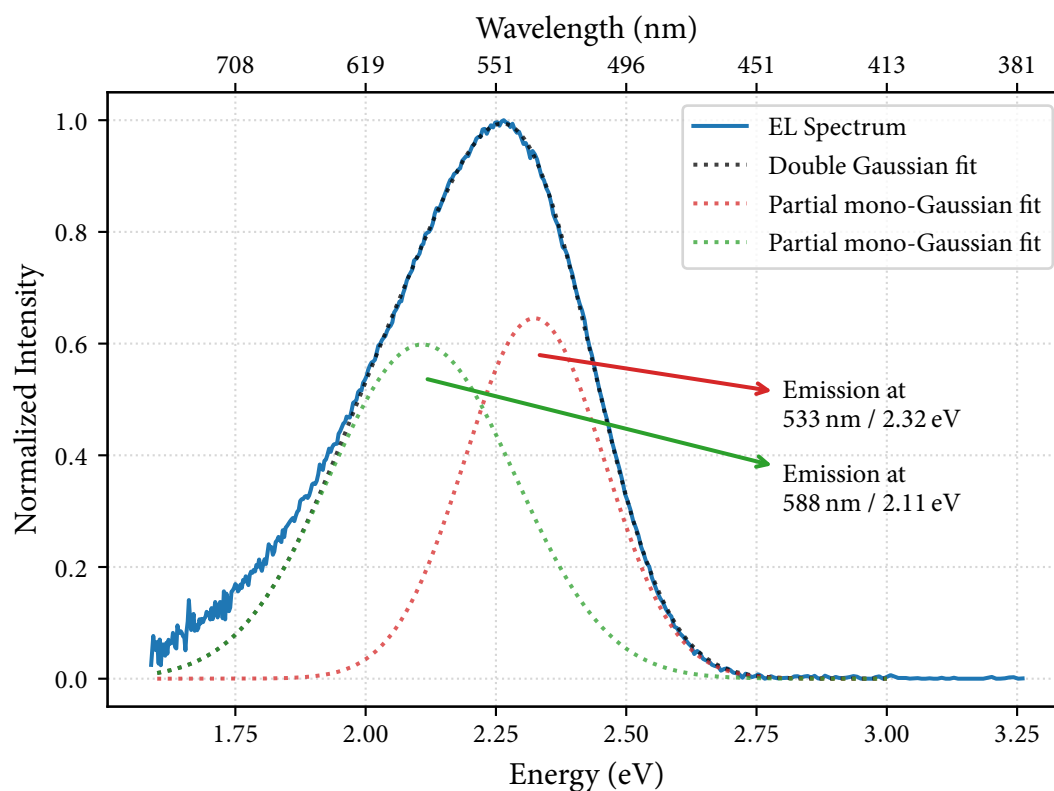


Figure A.4: Double Gaussian fit on an Alq₃-poly-TPD based EL spectrum. The fits no longer represent an Alq₃ Emission. The fits differ from data below 2.0 eV, which may be caused by another additional emission. ^{S.69}

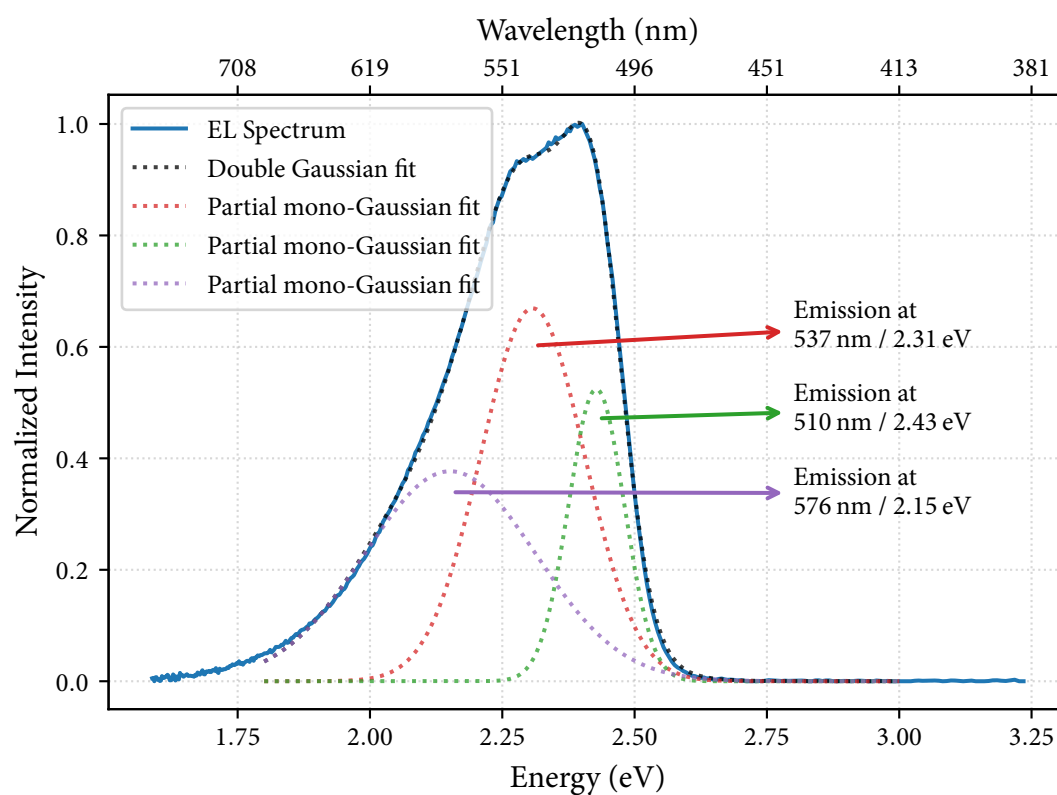


Figure A.5: Triple Gaussian fit on a CBP:Ir(ppy)₃ based EL spectrum. S.38

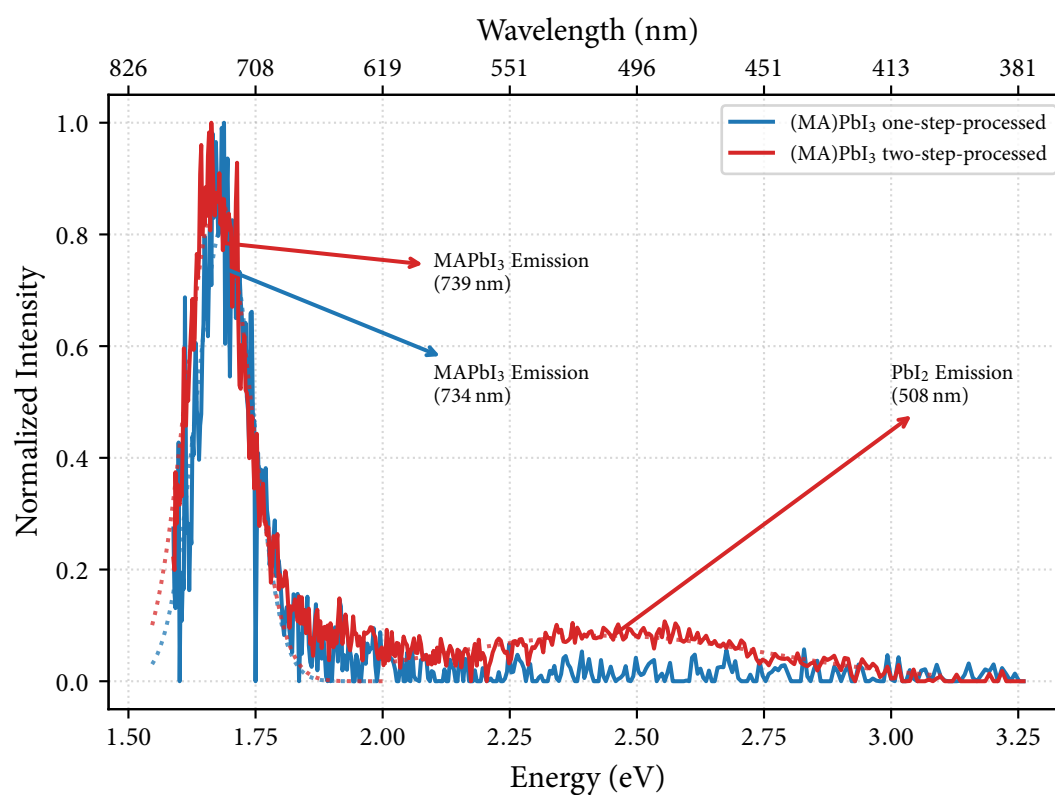


Figure A.6: Fits on the (MA)PbI₃ EL Spectrum. ^{S.48}

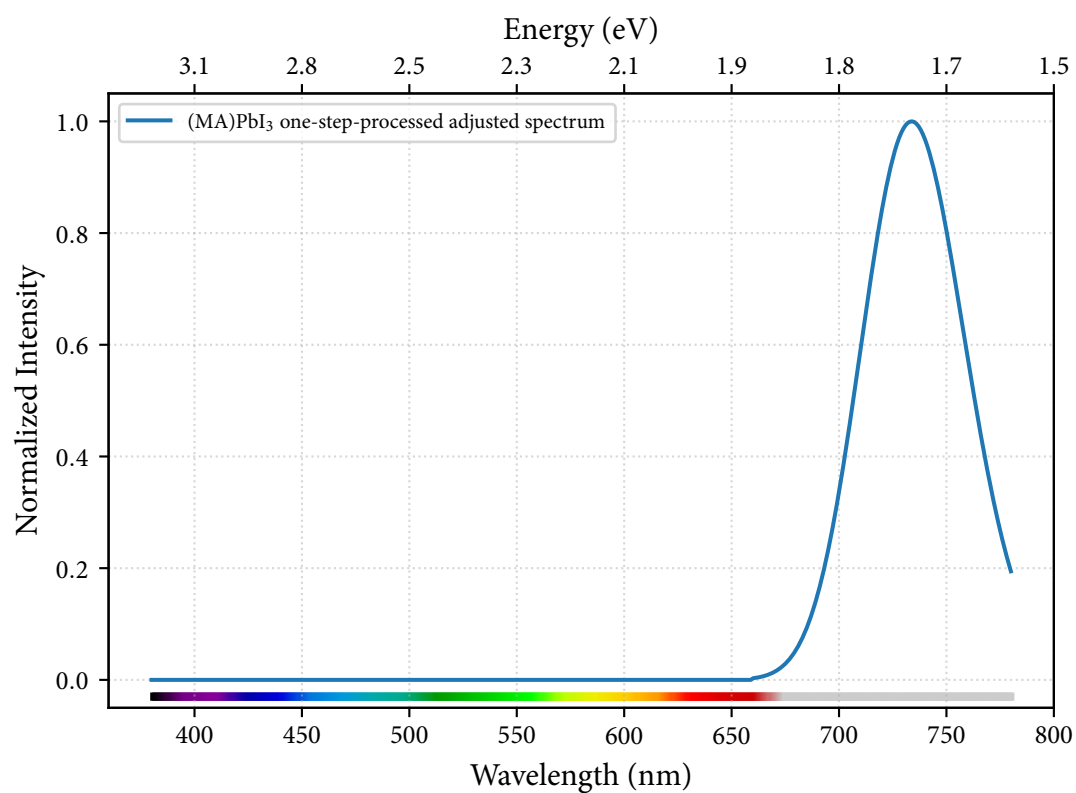


Figure A.7: Adjusted Spectrum created with a fit, to reduce the noise which has high impact on the EQE. [S.48](#), [S.70](#)

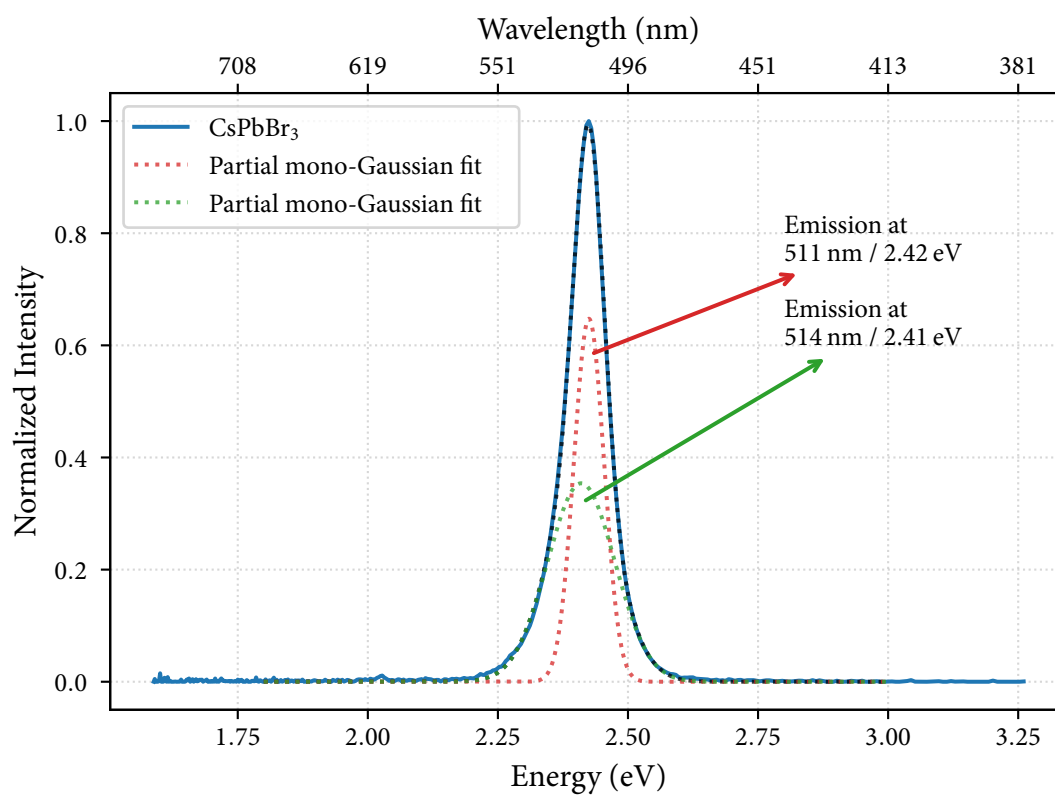


Figure A.8: Fits on the CsPbBr₃ EL spectrum. The CsPbBr₃ peak is actually a double peak; the second peak may also arise from absorption or interference effects.^{S.59}

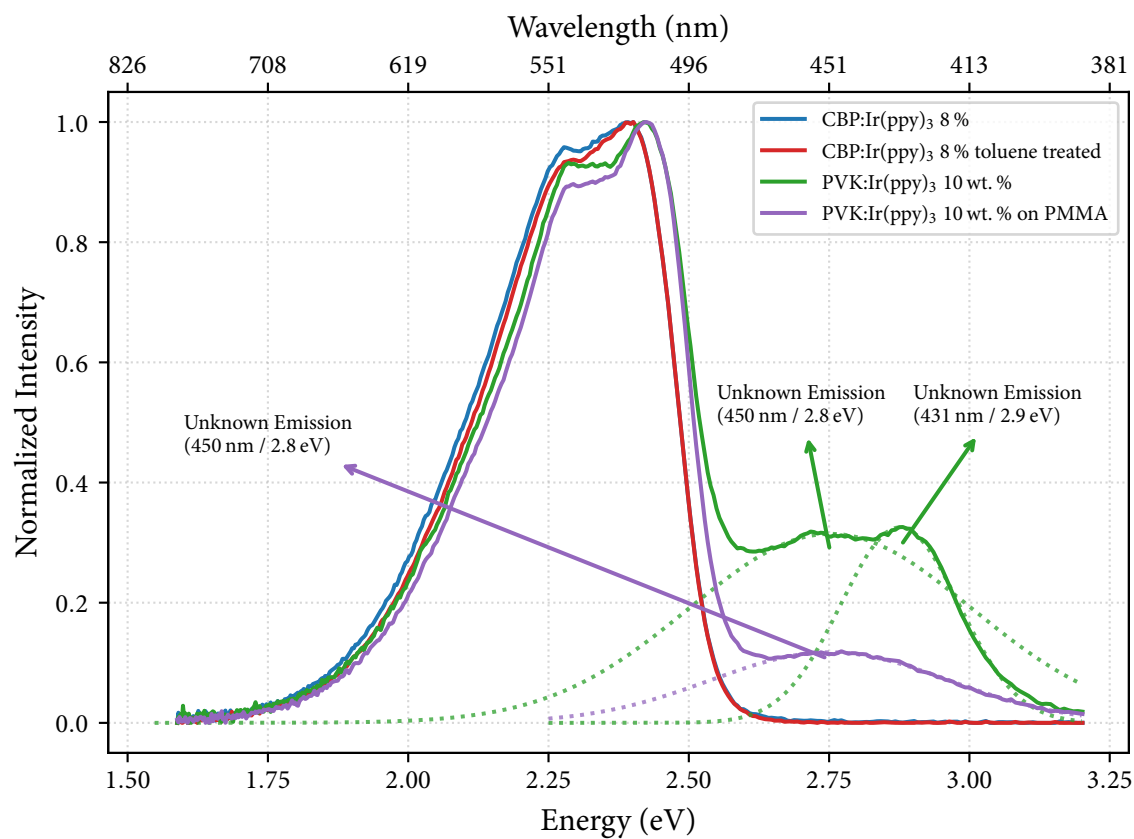


Figure A.9: Fits on the PVK:Ir(ppy)₃ spectrum. The additional blue emission is only visible when PVK is involved. Without PMMA there is another peak which may arise by influences of the poly-TPD.^{S.71}

8.2 Photometric Calculations

8.2.1 Calibration of the Photodiode

The photodiode has different spectral sensibilities $s(\lambda)$. The absolute spectral relation between outgoing photo-current I_p and incoming radiant Power Φ_e (unit: Watt) is calibrated on the pure Silicon chip. On the other hand a relative spectral sensibility is measured through a VL filter. This spectra is mostly congruent with the luminosity function. So it's maxima is at 555 nm and its value is 1.¹⁰³ With the continuity equation at the back of one's mind, one can conclude, that the photo-current at 555 nm is smaller or equal than the value without filter. For now the photo-current at this point it considered equal, so no additional losses at 555 nm. The whole spectral sensibility is equal to the luminous function $V(\lambda)$. Only $s(555 \text{ nm})$ and $s(560 \text{ nm})$ are given by the calibration sheet, so one assumes a linear correlation:

$$s_{\max} = s(555 \text{ nm}) = \frac{s(560 \text{ nm}) + s(550 \text{ nm})}{2} = 0.3216 \frac{\text{A}}{\text{W}}. \quad (\text{A.1})$$

8.2.2 Photo-current to Lumen Dependence

So the photo-current and the incident light power is correlated as follows:

$$I_p = \int_0^\infty \Psi(\lambda) \frac{\partial \Phi_e}{\partial \lambda} d\lambda. \quad (\text{A.2})$$

$$\Psi(\lambda) = s_{\max} \cdot V(\lambda) \quad (\text{A.3})$$

Φ_e is weighted by the (photopic, that is human daylight vision) luminous function $V(\lambda)$.¹⁰⁴

$$I_p = s_{\max} \cdot \int_0^\infty V(\lambda) \frac{\partial \Phi_e}{\partial \lambda} d\lambda. \quad (\text{A.4})$$

$$I_p = s_{\max} \cdot \frac{K_m}{K_m} \cdot \int_0^\infty V(\lambda) \frac{\partial \Phi_e}{\partial \lambda} d\lambda. \quad (\text{A.5})$$

At this point it is important to know, that the luminous flux Φ_v (unit: Lumen) is given by:^{103, 105}

$$\Phi_v = K_m \cdot \int_0^\infty V(\lambda) \frac{\partial \Phi_e}{\partial \lambda} d\lambda. \quad (\text{A.6})$$

With $K_m = 673 \frac{\text{lm}}{\text{W}}$ (photopic). Together with Eq. A.5:

$$I_p = \frac{s_{\max}}{K_m} \cdot \Phi_v. \quad (\text{A.7})$$

8.2.3 Luminous Flux to Luminance Dependence

The luminance L_v is defined as the luminous flux per square meter (Area A) light source into a steradian (Ω) of space¹⁰⁵:

$$L_v = \frac{\partial^2 \Phi_v}{\cos(\theta) \partial A \partial \Omega}. \quad (\text{A.8})$$

$$\Phi_v = \int_{\Omega} \int_A L_v \cos(\theta) d\Omega dA. \quad (\text{A.9})$$

L_v is independent of position (assuming lambertian emission) so it could be taken out of the integral and the equation is rearranged:

$$L_v = \frac{\Phi_v}{\int_{\Omega} \int_A \cos(\theta) d\Omega dA}. \quad (\text{A.10})$$

$$L_v = \frac{\Phi_v}{A \cdot \int_{\Omega} \cos(\theta) d\Omega}. \quad (\text{A.11})$$

$$L_v = \frac{\Phi_v}{A \cdot \int_0^{\theta} \int_0^{2\pi} \cos(\theta) \sin\theta d\theta d\phi}. \quad (\text{A.12})$$

$$L_v = \frac{\Phi_v}{2\pi A \cdot \int_0^{\theta} \cos(\theta) \sin\theta d\theta}. \quad (\text{A.13})$$

$$L_v = \frac{\Phi_v}{2\pi A \cdot \frac{1}{2} \sin^2(\theta)}. \quad (\text{A.14})$$

The considered θ is set to be the opening angle of a cone (So the angle on the 2D projection of the cone of the axial symmetry axis and the edge). See Ref ^{105, 106}.

$$\theta = 2\arccos\left(1 - \frac{\Omega}{2\pi}\right). \quad (\text{A.15})$$

The steradian is equal to the considered sphere cap area divided by the surface of the whole sphere. For long radius and small areas, that is, if the sphere cap area is approximately equal to the circle area:

$$A_{\text{sphere_cap}} = 2\pi r^2 \cdot (1 - \cos(\theta)). \quad (\text{A.16})$$

$$A_{\text{circle}} = \pi a^2 = \pi r^2 \sin^2(\theta). \quad (\text{A.17})$$

For small θ ($\sin(\theta) = \frac{a}{r} \stackrel{a \ll r}{\approx} \theta$)

$$A_{\text{sphere_cap}} = 2\pi r^2 \cdot \left(1 - \left(1 - \frac{1}{2}\theta^2\right)\right). \quad (\text{A.18})$$

$$A_{\text{circle}} = \pi a^2 = \pi r^2 \theta^2. \quad (\text{A.19})$$

$$A_{\text{sphere_cap}} = 2\pi r^2 \cdot \left(\frac{1}{2}\theta^2\right). \quad (\text{A.20})$$

$$A_{\text{sphere_cap}} = \pi r^2 \theta^2 = A_{\text{circle}}. \quad (\text{A.21})$$

At this point the radius is just the distance between measured pixel and photodiode. The spherical cap circle shaped area (not the cap) is the area of the photodiode.

$$A_{\text{circle}} = \pi r^2 \theta^2. \quad (\text{A.22})$$

$$\theta = \sqrt{\frac{A_{\text{circle}}}{\pi r^2}}. \quad (\text{A.23})$$

With Eq. A.14:

$$L_v = \frac{\Phi_v}{\pi A_{\text{Pixel}} \cdot \theta^2}. \quad (\text{A.24})$$

$$L_v = \frac{\Phi_v}{\pi A_{\text{Pixel}} \cdot \frac{A_{\text{Photodiode}}}{\pi r^2}}. \quad (\text{A.25})$$

$$L_v = \frac{\Phi_v \cdot r^2}{A_{\text{Pixel}} \cdot A_{\text{Photodiode}}}. \quad (\text{A.26})$$

With Eq. A.7:

$$L_v = \frac{I_p \cdot K_m \cdot r^2}{s_{\text{max}} \cdot A_{\text{Pixel}} \cdot A_{\text{Photodiode}}}. \quad (\text{A.27})$$

$$L_v = c \cdot I_p. \quad (\text{A.28})$$

$$c = \frac{K_m \cdot r^2}{s_{\text{max}} \cdot A_{\text{Pixel}} \cdot A_{\text{Photodiode}}}. \quad (\text{A.29})$$

8.2.4 Radiance from Energy Distribution and Spectral Radiance

$$L_e = \int_0^\infty L_{e,\lambda}(\lambda) d\lambda. \quad (\text{A.30})$$

$$L_e = \sum_{i=0}^N L_{e,\lambda}(\lambda_i) \cdot \Delta\lambda. \quad (\text{A.31})$$

$$\frac{L_e}{\Delta\lambda} = \sum_{i=0}^N L_{e,\lambda}(\lambda_i). \quad (\text{A.32})$$

The spectral radiance distribution is the same as the distribution of photons of respective energy, which has already been introduced (see Eq. 15 ff.):

$$\frac{L_e}{\Delta\lambda} = \sum_{i=0}^N L_{e,\lambda}^- \cdot \Psi(\lambda_i). \quad (\text{A.33})$$

$$\frac{L_e}{\Delta\lambda} = L_{e,\lambda}^- \cdot \sum_{i=0}^N \Psi(\lambda_i). \quad (\text{A.34})$$

$$\frac{L_e}{\Delta\lambda} = L_{e,\lambda}^-. \quad (\text{A.35})$$

$$L_{e,\lambda}(\lambda_i) = L_{e,\lambda}^- \cdot \Psi(\lambda_i) = \frac{L_e}{\Delta\lambda} \cdot \Psi(\lambda_i). \quad (\text{A.36})$$

8.2.5 Calculation for the present OLED-Measurement-Box

$$A_{\text{Photodiode}} = 10^{-4} \text{ m}^2. \quad (\text{A.37})$$

The devices' pixels can be 1 mm² or 4 mm² big, the calculation is done with 1 and the final result can be divided by 4.

$$A_{\text{Pixel}} = 10^{-6} \text{ m}^2. \quad (\text{A.38})$$

$$r = 45 \cdot 10^{-3} \text{ m}. \quad (\text{A.39})$$

$$K_m = 683 \frac{\text{lm}}{\text{W}}. \quad (\text{A.40})$$

$$s_{\text{max}} = 0.3216 \frac{\text{A}}{\text{W}}. \quad (\text{A.41})$$

Eq. A.29 can be solved:

$$c = \frac{683 \frac{\text{lm}}{\text{W}} \cdot (45 \cdot 10^{-3} \text{ m})^2}{0.3216 \frac{\text{A}}{\text{W}} \cdot 10^{-6} \text{ m}^2 \cdot 10^{-4} \text{ m}^2 \text{ sr}}. \quad (\text{A.42})$$

$$c = 4.3 \cdot 10^{10} \frac{\text{lm}}{\text{A} \cdot \text{m}^2 \cdot \text{sr}} = 4.3 \cdot 10^{10} \frac{\text{cd}}{\text{A} \cdot \text{m}^2}. \quad (\text{A.43})$$

$$L_v = 4.3 \cdot 10^{10} \frac{\text{cd}}{\text{A} \cdot \text{m}^2} \cdot I_p. \quad (\text{A.44})$$

8.2.6 Estimation of Errors

Note that the luminance is generally not independent of the direction, the error by non lambertian emitters can't be approximated in general and has to be considered for each device. This error is not included in the following approximations.

Error of small angle approximation:

$$\frac{a}{r} = \frac{10 \text{ mm}}{45 \text{ mm}} = \frac{2}{9} = \sin(\theta). \quad (\text{A.45})$$

$$\sin(\theta) \stackrel{!}{=} \theta. \quad (\text{A.46})$$

$$\arcsin\left(\frac{2}{9}\right) \approx 0.224 \stackrel{!}{\approx} 0.222 \approx \theta. \quad (\text{A.47})$$

$$\Delta\theta = 0.002 \text{ (radians)} \quad (\text{A.48})$$

$$\frac{\Delta\theta}{\theta} \leq 1 \%. \quad (\text{A.49})$$

$$(\text{A.50})$$

This error is very small, and it will be accounted for by the error in distance r .

Error by different pixel areas, mostly by evaporation size errors:

$$\Delta A_{\text{Pixel}} := 1 \cdot 10^{-7} \text{ m}^2. \quad (\text{A.51})$$

$$\frac{\Delta A_{\text{Pixel}}}{A_{\text{Pixel}}} \leq 10 \%. \quad (\text{A.52})$$

$$(\text{A.53})$$

Error by distance photodiode to sample, given by the measurement-box design:

$$\Delta r := 5 \cdot 10^{-3} \text{ m}. \quad (\text{A.54})$$

$$\frac{\Delta r}{r} \leq 11, 1 \%. \quad (\text{A.55})$$

Error in the photodiodes response function:

It is estimated to yield an error of about 5 %. Which also accounts the difference between the standards of photopic luminance curves. This error is accounted by:

$$\frac{\Delta s_{\text{max}}}{s_{\text{max}}} = 5 \%. \quad (\text{A.56})$$

$$\Delta s_{\text{max}} = 0.3216 \cdot 5 \% = 0.01608. \quad (\text{A.57})$$

Error of the source measure unit (SMU) by Agilent Technologies (Agilent E5291A), from data-sheet and verified by noise signal noise ratio:

$$\Delta I_p = 5 \cdot 10^{-12} \text{ A}. \quad (\text{A.58})$$

for Photo-currents higher than $5 \cdot 10^{-11} \text{ A}$:

$$\frac{\Delta I_p}{I_p} \leq 10 \%. \quad (\text{A.59})$$

Luminance For an ideal lambertian emitter the normally distributed error in luminance is with Eq. A.27:

$$\Delta L_v^2 = \left(\frac{\partial L_v}{\partial I_p} \cdot \Delta I_p \right)^2 + \left(\frac{\partial L_v}{\partial r} \cdot \Delta r \right)^2 + \left(\frac{\partial L_v}{\partial s_{\max}} \cdot \Delta s_{\max} \right)^2 + \left(\frac{\partial L_v}{\partial A_{\text{Pixel}}} \cdot \Delta A_{\text{Pixel}} \right)^2. \quad (\text{A.60})$$

$$\Delta L_v^2 = \left(L_v \cdot \frac{\Delta I_p}{I_p} \right)^2 + \left(2L_v \cdot \frac{\Delta r}{r} \right)^2 + \left(L_v \cdot \frac{\Delta s_{\max}}{s_{\max}} \right)^2 + \left(L_v \cdot \frac{\Delta A_{\text{Pixel}}}{A_{\text{Pixel}}} \right)^2. \quad (\text{A.61})$$

$$\left(\frac{\Delta L_v}{L_v} \right)^2 = \left(\frac{\Delta I_p}{I_p} \right)^2 + \left(2 \frac{\Delta r}{r} \right)^2 + \left(\frac{\Delta s_{\max}}{s_{\max}} \right)^2 + \left(\frac{\Delta A_{\text{Pixel}}}{A_{\text{Pixel}}} \right)^2. \quad (\text{A.62})$$

$$\frac{\Delta L_v}{L_v} \leq \sqrt{(10\%)^2 + (2 \cdot 11.1\%)^2 + (5\%)^2 + (10\%)^2}. \quad (\text{A.63})$$

$$\frac{\Delta L_v}{L_v} \leq 26.8\%. \quad (\text{A.64})$$

However, with better accuracy of the pixel size and for high photo-currents, the error can be reduced to:

$$\frac{\Delta L_v}{L_v} \leq \sqrt{(2 \cdot 11.1\%)^2 + (5\%)^2} = 22.8\%. \quad (\text{A.65})$$

The highest error arises from the distance of the sample to photodiode. This distance can only be further accurately determined, if the experiment is modified: The present installation leaves a tolerance in vertical position of the sample and the photodiode of about 2.5 mm respectively. To reduce errors even further, the response function of the photodiode could be re-calibrated. Photo-currents lower than $5 \cdot 10^{-11}$ A do increase the error even more, hence the values below this threshold are clipped. The calculated luminance values are compared to the ones measured by the spectroradiometer, see table A.1. The “XVI” samples have a higher error than expected. However this error is strictly negative, since the devices degrade during the measurement. And the j-V-L measurement has been done prior to the spectroradiometer measurement. Hence, the higher error can be explained by the degradation. For the samples driven at 6 Volt a degradation is not observed. For these devices, the error fits in the range of expected error. Overall the positive Error, which can’t be explained by degradation, shows a deviation of $< 20\%$ which is still within the estimated error range. So the luminance values are confirmed to be in the range of the estimated errors.

Sample	Luminance calculated	Luminance measured	Difference	relative Deviation
LXI_ A_1 at 6 V	112.3 $\frac{\text{cd}}{\text{m}^2}$	111.1 $\frac{\text{cd}}{\text{m}^2}$	-1.2 $\frac{\text{cd}}{\text{m}^2}$	-1.1 %
LXI_ B_1 at 6 V	300.3 $\frac{\text{cd}}{\text{m}^2}$	369.2 $\frac{\text{cd}}{\text{m}^2}$	+68,9 $\frac{\text{cd}}{\text{m}^2}$	+18.7 %
XVI_ B_1 at 9 V	36.3 $\frac{\text{cd}}{\text{m}^2}$	16.7 $\frac{\text{cd}}{\text{m}^2}$	-19.6 $\frac{\text{cd}}{\text{m}^2}$	-117.4 %
XVI_ C_1 at 15 V	24.3 $\frac{\text{cd}}{\text{m}^2}$	14.7 $\frac{\text{cd}}{\text{m}^2}$	-9.6 $\frac{\text{cd}}{\text{m}^2}$	-65.3 %

Table A.1: Comparison between measured and calculated luminances.

EQE The EQE is less error prone, since the pixel-size cancels; with Eq. 30 and A.27:

$$\eta_{\text{EQE}} = \frac{\pi \cdot A \cdot e \cdot \frac{I_P \cdot K_m \cdot r^2}{s_{\text{max}} \cdot A_{\text{Pixel}} \cdot A_{\text{Photodiode}}}}{K_m \cdot hc \cdot I \cdot \sum_{i=0}^N V(\lambda_i) \Psi(\lambda_i) \cdot \sum_{i=0}^N \frac{1}{\lambda_i} \cdot \Psi(\lambda_i)} \quad (\text{A.66})$$

$$\eta_{\text{EQE}} = \frac{\pi \cdot e \cdot I_P \cdot r^2}{s_{\text{max}} \cdot A_{\text{Photodiode}} \cdot hc \cdot I \cdot \sum_{i=0}^N V(\lambda_i) \Psi(\lambda_i) \cdot \sum_{i=0}^N \frac{1}{\lambda_i} \cdot \Psi(\lambda_i)} \quad (\text{A.67})$$

Analogous reshaping like in Eq. A.60 and the following:

$$\left(\frac{\Delta \eta_{\text{EQE}}}{\eta_{\text{EQE}}} \right)^2 = \left(\frac{\Delta I_P}{I_P} \right)^2 + \left(2 \frac{\Delta r}{r} \right)^2 + \left(\frac{\Delta s_{\text{max}}}{s_{\text{max}}} \right)^2 \quad (\text{A.68})$$

$$\frac{\Delta \eta_{\text{EQE}}}{\eta_{\text{EQE}}} \leq \sqrt{(2 \cdot 11.1 \%)^2 + (5 \%)^2} \leq \sqrt{(10 \%)^2 + (2 \cdot 11.1 \%)^2 + (5 \%)^2} \quad (\text{A.69})$$

$$\frac{\Delta \eta_{\text{EQE}}}{\eta_{\text{EQE}}} \leq 22.8 \% \leq 24.9 \% \quad (\text{A.70})$$

8.2.7 Wavelength to Energy Scale Conversion

Spectra are mostly measured as spectral radiance ($L_{e,\lambda} = \frac{\partial L_e}{\partial \lambda}$) vs wavelength (λ). So generally the value of interest is the spectral intensity (I_λ) which is defined as power per area and wavelength. Consequently the intensity is proportional to the spectral radiant intensity power per steradian and wavelength (watt per steradian nanometer), when measuring the same distance. Furthermore it is even proportional to the spectral radiance (watt per steradian and square-meter and nanometer), when considering same sized emitting areas. However the energy scale spectral intensity (I_E) is not proportional to the wavelength scale spectral intensity (I_λ). See also Ref. 107.

$$I_\lambda \propto L_{e,\lambda} \not\propto L_{e,E} \propto I_E \quad (\text{A.71})$$

With $E = h\frac{c}{\lambda}$ the differential Energy dE is

$$dE = d\left(\frac{hc}{\lambda}\right) = hc \cdot d(1/\lambda) = -hc \cdot \frac{1}{\lambda^2} \cdot d\lambda \quad (\text{A.72})$$

$$d\lambda = dE \cdot \frac{\lambda^2}{hc} \quad (\text{A.73})$$

So the intensity can be plotted with the energy or frequency

$$dL_e = \frac{\partial L_e}{\partial \lambda} d\lambda = \frac{\partial L_e}{\partial \lambda} \cdot \frac{\lambda^2}{hc} \cdot dE \quad (\text{A.74})$$

$$\frac{dL_e}{dE} = \frac{\partial L_e}{\partial E} = \frac{\partial L_e}{\partial \lambda} \cdot \frac{\lambda^2}{hc} \quad (\text{A.75})$$

$$L_{e,E} = L_{e,\lambda} \cdot \frac{\lambda^2}{hc} \quad (\text{A.76})$$

So there is a factor of $\frac{\lambda^2}{hc}$ to convert from wavelength scale to energy scale.

9 References

- ¹ J. Song, J. Li, X. Li, L. Xu, Y. Dong, and H. Zeng, “Quantum Dot Light-Emitting Diodes Based on Inorganic Perovskite Cesium Lead Halides (CsPbX₃)”, *Advanced Materials* **27**, 7162–7167 (2015).
- ² W. Brütting, ed., *Physics of Organic Semiconductors* (Wiley-VCH Verlag GmbH & Co. KGaA, May 2005).
- ³ A. Köhler and H. Bässler, *Electronic Processes in Organic Semiconductors* (Wiley-VCH Verlag GmbH & Co. KGaA, May 2015).
- ⁴ T. D. Schmidt, “Photophysics of organic light-emitting diodes - Device efficiency and degradation process”, PhD thesis (University of Augsburg, 2013).
- ⁵ *Setting up the new efficiency limit of OLEDs*, (2014) <http://ee.princeton.edu/events/setting-new-efficiency-limit-oleds> (visited on 09/19/2018).
- ⁶ J. G. Bednorz and K. A. Müller, “Possible high T_c superconductivity in the BaLaCuO system”, *Zeitschrift für Physik B Condensed Matter* **64**, 189–193 (1986).
- ⁷ M. A. Peña and J. L. G. Fierro, “Chemical Structures and Performance of Perovskite Oxides”, *Chemical Reviews* **101**, 1981–2018 (2001).
- ⁸ R. D. Shannon, “Revised effective ionic radii and systematic studies of interatomic distances in halides and chalcogenides”, *Acta Crystallographica Section A* **32**, 751–767 (1976).
- ⁹ W.-J. Yin, T. Shi, and Y. Yan, “Unusual defect physics in CH₃NH₃PbI₃ perovskite solar cell absorber”, *Applied Physics Letters* **104**, 063903 (2014).
- ¹⁰ G. Kresse and J. Furthmüller, “Efficient iterative schemes for ab initio total-energy calculations using a plane-wave basis set”, *Physical Review B* **54**, 11169–11186 (1996).
- ¹¹ M. A. Becker, R. Vaxenburg, G. Nedelcu, P. C. Serce, A. Shabaev, M. J. Mehl, J. G. Michopoulos, S. G. Lambrakos, N. Bernstein, J. L. Lyons, T. Stöferle, R. F. Mahrt, M. V. Kovalenko, D. J. Norris, G. Rainò, and A. L. Efros, “Bright triplet excitons in caesium lead halide perovskites”, *Nature* **553**, 189–193 (2018).
- ¹² G. Giorgi, J.-I. Fujisawa, H. Segawa, and K. Yamashita, “Small Photocarrier Effective Masses Featuring Ambipolar Transport in Methylammonium Lead Iodide Perovskite: A Density Functional Analysis”, *The Journal of Physical Chemistry Letters* **4**, 4213–4216 (2013).
- ¹³ W.-J. Yin, J.-H. Yang, J. Kang, Y. Yan, and S.-H. Wei, “Halide perovskite materials for solar cells: a theoretical review”, *Journal of Materials Chemistry A* **3**, 8926–8942 (2015).

- ¹⁴ T. Tiedje, E. Yablonovitch, G. D. Cody, and B. G. Brooks, "Limiting efficiency of silicon solar cells", *IEEE Transactions on electron devices* **31**, 711–716 (1984).
- ¹⁵ J. Li, L. Xu, T. Wang, J. Song, J. Chen, J. Xue, Y. Dong, B. Cai, Q. Shan, B. Han, and H. Zeng, "50-Fold EQE Improvement up to 6.27% of Solution-Processed All-Inorganic Perovskite CsPbBr₃QLEDs via Surface Ligand Density Control", *Advanced Materials* **29**, 1603885 (2016).
- ¹⁶ S. K. Jeon, K. S. Yook, and J. Y. Lee, "Surface initiated oxidative crosslinking of a polymeric hole transport material for improved efficiency and lifetime in soluble organic light-emitting diodes", *Organic Electronics* **38**, 278–282 (2016).
- ¹⁷ M. J. Jurow, T. Lampe, E. Penzo, J. Kang, M. A. Koc, T. Zechel, Z. Nett, M. Brady, L.-W. Wang, A. P. Alivisatos, S. Cabrini, W. Brütting, and Y. Liu, "Tunable Anisotropic Photon Emission from Self-Organized CsPbBr₃ Perovskite Nanocrystals", *Nano Letters* **17**, 4534–4540 (2017).
- ¹⁸ D. H. Cao, C. C. Stoumpos, C. D. Malliakas, M. J. Katz, O. K. Farha, J. T. Hupp, and M. G. Kanatzidis, "Remnant PbI₂, an unforeseen necessity in high-efficiency hybrid perovskite-based solar cells?", *APL Materials* **2**, 091101 (2014).
- ¹⁹ G. Xing, N. Mathews, S. Sun, S. S. Lim, Y. M. Lam, M. Gratzel, S. Mhaisalkar, and T. C. Sum, "Long-Range Balanced Electron- and Hole-Transport Lengths in Organic-Inorganic CH₃NH₃PbI₃", *Science* **342**, 344–347 (2013).
- ²⁰ S. D. Stranks, G. E. Eperon, G. Grancini, C. Menelaou, M. J. P. Alcocer, T. Leijtens, L. M. Herz, A. Petrozza, and H. J. Snaith, "Electron-Hole Diffusion Lengths Exceeding 1 Micrometer in an Organometal Trihalide Perovskite Absorber", *Science* **342**, 341–344 (2013).
- ²¹ D. Shi, V. Adinolfi, R. Comin, M. Yuan, E. Alarousu, A. Buin, Y. Chen, S. Hoogland, A. Rothenberger, K. Katsiev, Y. Losovyj, X. Zhang, P. A. Dowben, O. F. Mohammed, E. H. Sargent, and O. M. Bakr, "Low trap-state density and long carrier diffusion in organolead trihalide perovskite single crystals", *Science* **347**, 519–522 (2015).
- ²² B. R. Sutherland and E. H. Sargent, "Perovskite photonic sources", *Nature Photonics* **10**, 295–302 (2016).
- ²³ W. Ming, D. Yang, T. Li, L. Zhang, and M.-H. Du, "Formation and Diffusion of Metal Impurities in Perovskite Solar Cell Material CH₃ NH₃ PbI₃ : Implications on Solar Cell Degradation and Choice of Electrode", *Advanced Science* **5**, 1700662 (2017).
- ²⁴ Z. Xiao, R. A. Kerner, L. Zhao, N. L. Tran, K. M. Lee, T.-W. Koh, G. D. Scholes, and B. P. Rand, "Efficient perovskite light-emitting diodes featuring nanometre-sized crystallites", *Nature Photonics* **11**, 108–115 (2017).
- ²⁵ V. Sidey, "On the effective ionic radii for ammonium", *Acta Crystallographica Section B Structural Science, Crystal Engineering and Materials* **72**, 626–633 (2016).

- ²⁶ E. Mosconi, J. M. Azpiroz, and F. D. Angelis, "Ab Initio Molecular Dynamics Simulations of Methylammonium Lead Iodide Perovskite Degradation by Water", *Chemistry of Materials* **27**, 4885–4892 (2015).
- ²⁷ C. Besleaga, L. E. Abramiuc, V. Stancu, A. G. Tomulescu, M. Sima, L. Trinca, N. Plugaru, L. Pintilie, G. A. Nemnes, M. Iliescu, H. G. Svavarsson, A. Manolescu, and I. Pintilie, "Iodine Migration and Degradation of Perovskite Solar Cells Enhanced by Metallic Electrodes", *The Journal of Physical Chemistry Letters* **7**, 5168–5175 (2016).
- ²⁸ M. Kulbak, D. Cahen, and G. Hodes, "How Important Is the Organic Part of Lead Halide Perovskite Photovoltaic Cells? Efficient CsPbBr₃ Cells", *The Journal of Physical Chemistry Letters* **6**, 2452–2456 (2015).
- ²⁹ L. Protesescu, S. Yakunin, M. I. Bodnarchuk, F. Krieg, R. Caputo, C. H. Hendon, R. X. Yang, A. Walsh, and M. V. Kovalenko, "Nanocrystals of Cesium Lead Halide Perovskites (CsPbX₃, X = Cl, Br, and I): Novel Optoelectronic Materials Showing Bright Emission with Wide Color Gamut", *Nano Letters* **15**, 3692–3696 (2015).
- ³⁰ V. K. Ravi, G. B. Markad, and A. Nag, "Band Edge Energies and Excitonic Transition Probabilities of Colloidal CsPbX₃ (X = Cl, Br, I) Perovskite Nanocrystals", *ACS Energy Letters* **1**, 665–671 (2016).
- ³¹ H. Huang, H. Lin, S. V. Kershaw, A. S. Susha, W. C. H. Choy, and A. L. Rogach, "Polyhedral Oligomeric Silsesquioxane Enhances the Brightness of Perovskite Nanocrystal-Based Green Light-Emitting Devices", *The Journal of Physical Chemistry Letters* **7**, 4398–4404 (2016).
- ³² M. C. Brennan, J. E. Herr, T. S. Nguyen-Beck, J. Zinna, S. Draguta, S. Rouvimov, J. Parkhill, and M. Kuno, "Origin of the Size-Dependent Stokes Shift in CsPbBr₃ Perovskite Nanocrystals", *Journal of the American Chemical Society* **139**, 12201–12208 (2017).
- ³³ A. Swarnkar, R. Chulliyil, V. K. Ravi, M. Irfanullah, A. Chowdhury, and A. Nag, "Colloidal CsPbBr₃ Perovskite Nanocrystals: Luminescence beyond Traditional QDs", *Angewandte Chemie International Edition* **54**, 15424–15428 (2015).
- ³⁴ PEDOT:PSS's website by sigma-aldrich, <https://www.sigmaaldrich.com/catalog/product/aldrich/806781> (visited on 09/19/2018).
- ³⁵ polyTPD's website by lumtec, http://www.lumtec.com.tw/portal_c1_cnt_page.php?owner_num=c1_290785&button_num=c1&folder_id=41516&cnt_id=516363 (visited on 09/19/2018).
- ³⁶ PEDOT:PSS' website by ossila, <https://www.ossila.com/products/pedot-pss> (visited on 09/19/2018).
- ³⁷ Y. Yang, T. Nakamichi, H. Yoshioka, M. Yahiro, M. Era, H. Watanabe, Y. Cui, Y. Oki, and G. Qian, "Spectral-resolving capable and integratable multilayered conductive films via an inkjet method (Supplemental Information)", *Journal of Materials Chemistry C* **1**, 1739 (2013).

- ³⁸ A. Lenz, H. Kariis, A. Pohl, P. Persson, and L. Ojamäe, “The electronic structure and reflectivity of PEDOT:PSS from density functional theory”, *Chemical Physics* **384**, 44–51 (2011).
- ³⁹ T.-C. Tsai, H.-C. Chang, C.-H. Chen, Y.-C. Huang, and W.-T. Whang, “A facile de-doping approach for effectively tuning thermoelectricity and acidity of PEDOT: PSS films”, *Organic Electronics* **15**, 641–645 (2014).
- ⁴⁰ Y. Mochizuki, T. Horii, and H. Okuzaki, “Effect of pH on structure and conductivity of PEDOT/PSS”, *Transactions of the Materials Research Society of Japan* **37**, 307–310 (2012).
- ⁴¹ M. P. de Jong, L. J. van IJzendoorn, and M. J. A. de Voigt, “Stability of the interface between indium-tin-oxide and poly(3,4-ethylenedioxythiophene)/poly(styrenesulfonate) in polymer light-emitting diodes”, *Applied Physics Letters* **77**, 2255–2257 (2000).
- ⁴² A. van Dijken, A. Perro, E. Meulenkamp, and K. Brunner, “The influence of a PEDOT:PSS layer on the efficiency of a polymer light-emitting diode”, *Organic Electronics* **4**, 131–141 (2003).
- ⁴³ S. Jönsson, J. Birgersson, X. Crispin, G. Greczynski, W. Osikowicz, A. D. van der Gon, W. Salaneck, and M. Fahlman, “The effects of solvents on the morphology and sheet resistance in poly(3,4-ethylenedioxythiophene)–polystyrenesulfonic acid (PEDOT–PSS) films”, *Synthetic Metals* **139**, 1–10 (2003).
- ⁴⁴ PEDOT:PSS CH8000’s website by heraeus, https://www.heraeus.com/media/media/group/doc_group/products_1/conductive_polymers_1/p/CLEVIOS_P_VP_CH_8000.pdf (visited on 09/19/2018).
- ⁴⁵ PEDOT:PSS CH8000’s website by heraeus, https://www.heraeus.com/media/media/group/doc_group/products_1/conductive_polymers_1/HPM_FL_OLED_Overview.pdf (visited on 09/19/2018).
- ⁴⁶ polyTPD’s entry by ossila, <https://www.ossila.com/products/polytpd> (visited on 09/19/2018).
- ⁴⁷ polyTPD’s entry by chemicalbook, http://www.chemicalbook.com/ChemicalProductProperty_EN_CB92548172.htm (visited on 09/19/2018).
- ⁴⁸ PVK’s website by sigma-aldrich, <https://www.sigmaaldrich.com/catalog/product/aldrich/182605> (visited on 09/19/2018).
- ⁴⁹ PMMA’s website by sigma-aldrich, <https://www.sigmaaldrich.com/catalog/product/aldrich/182230> (visited on 09/19/2018).
- ⁵⁰ S. M. Sayyah, A. B. Khaliel, and H. Moustafa, “Electronic Structure and Ground State Properties of PMMA Polymer: I. Step-By-Step Formation and Stereo-Regularity of the Polymeric Chain—AM1-MO Treatment”, *International Journal of Polymeric Materials* **54**, 505–518 (2005).

- ⁵¹ NPB's website by sigma-aldrich, <http://www.sigmaaldrich.com/catalog/product/aldrich/734594> (visited on 09/19/2018).
- ⁵² MMTDATA's website by sigma-aldrich, <https://www.sigmaaldrich.com/catalog/product/aldrich/776327> (visited on 09/19/2018).
- ⁵³ MMTDATA's website by ossila, <https://www.ossila.com/products/m-mtdata> (visited on 09/19/2018).
- ⁵⁴ W. Sachtler, G. Dorgelo, and A. Holscher, "The work function of gold", *Surface Science* **5**, 221–229 (1966).
- ⁵⁵ CBP's website by sigma-aldrich, <https://www.sigmaaldrich.com/catalog/product/aldrich/660124> (visited on 09/19/2018).
- ⁵⁶ Irppy's website by sigma-aldrich, <https://www.sigmaaldrich.com/catalog/product/aldrich/694924> (visited on 09/19/2018).
- ⁵⁷ I. Iwakura, H. Ebina, K. Komori-Orisaku, and Y. Koide, "A theoretical and experimental study on meridional–facial isomerization of tris(quinolin-8-olate)aluminum (Alq3)", *Dalton Trans.* **43**, 12824–12827 (2014).
- ⁵⁸ S. Scholz, B. Lüssem, and K. Leo, "Chemical changes on the green emitter tris(8-hydroxy-quinolinato)aluminum during device aging of p-i-n-structured organic light emitting diodes", *Applied Physics Letters* **95**, 183309 (2009).
- ⁵⁹ Alq3's website by sigma-aldrich, <https://www.sigmaaldrich.com/catalog/product/aldrich/697737> (visited on 09/19/2018).
- ⁶⁰ M. Cölle and W. Brütting, "Thermal, structural and photophysical properties of the organic semiconductor Alq3", *physica status solidi (a)* **201**, 1095–1115 (2004).
- ⁶¹ D. Garbuzov, V. Bulović, P. Burrows, and S. Forrest, "Photoluminescence efficiency and absorption of aluminum-tris-quinolate (Alq3) thin films", *Chemical Physics Letters* **249**, 433–437 (1996).
- ⁶² S. Nowy, B. C. Krummacher, J. Frischeisen, N. A. Reinke, and W. Brütting, "Light extraction and optical loss mechanisms in organic light-emitting diodes: Influence of the emitter quantum efficiency", *Journal of Applied Physics* **104**, 123109 (2008).
- ⁶³ S. Nowy, "Understanding losses in OLEDs: optical device simulation and electrical characterization using impedance spectroscopy", PhD thesis (University of Augsburg, Apr. 2010).
- ⁶⁴ P. Liehm, C. Murawski, M. Furno, B. Lüssem, K. Leo, and M. C. Gather, "Comparing the emissive dipole orientation of two similar phosphorescent green emitter molecules in highly efficient organic light-emitting diodes", *Applied Physics Letters* **101**, 253304 (2012).
- ⁶⁵ TPBi's website by sigma-aldrich, <https://www.sigmaaldrich.com/catalog/product/aldrich/806781> (visited on 09/19/2018).

- ⁶⁶ BPhen's website by sigma aldrich, <https://www.sigmaaldrich.com/catalog/product/aldrich/133159> (visited on 09/19/2018).
- ⁶⁷ OXD7's website by lumtec, http://www.lumtec.com.tw/portal_c1_cnt_page.php?owner_num=c1_290785&button_num=c1&folder_id=30649&cnt_id=257676 (visited on 09/19/2018).
- ⁶⁸ TPBi's website by sigma-aldrich, <https://www.ossila.com/products/tpbi> (visited on 09/19/2018).
- ⁶⁹ BPhen's website by ossila, <https://www.ossila.com/products/bphen> (visited on 09/19/2018).
- ⁷⁰ OXD7's website by ossila, <https://www.ossila.com/products/oxd-7> (visited on 09/19/2018).
- ⁷¹ ITO's website by alfa, <https://www.alfa.com/de/catalog/036348/> (visited on 09/19/2018).
- ⁷² J. Wagner, "Electronic properties of interfaces in organic devices studied by Kelvin probe and impedance spectroscopy", MA thesis (University of Augsburg, 2008).
- ⁷³ P. Destruel, H. Bock, I. Séguy, P. Jolinat, M. Oukachmih, and E. Bedel-Pereira, "Influence of indium tin oxide treatment using UV-ozone and argon plasma on the photovoltaic parameters of devices based on organic discotic materials", *Polymer International* **55**, 601–607 (2006).
- ⁷⁴ A. G. Emslie, F. T. Bonner, and L. G. Peck, "Flow of a Viscous Liquid on a Rotating Disk", *Journal of Applied Physics* **29**, 858 (1958).
- ⁷⁵ B. D. Washo, "Rheology and Modeling of the Spin Coating Process", *IBM Journal of Research and Development* **21**, 190–198 (1977).
- ⁷⁶ Spin coating website by ossila, <https://www.ossila.com/pages/spin-coating#spin-coating-thickness-equation> (visited on 09/19/2018).
- ⁷⁷ D. B. Hall, P. Underhill, and J. M. Torkelson, "Spin coating of thin and ultrathin polymer films", *Polymer Engineering & Science* **38**, 2039–2045 (1998).
- ⁷⁸ C. Kittel, *Introduction to Solid State Physics*, edited by P. M. Stuart Johnson (John Wiley & Sons, Inc, 2004).
- ⁷⁹ S. Kawai, A. S. Foster, T. Björkman, S. Nowakowska, J. Björk, F. F. Canova, L. H. Gade, T. A. Jung, and E. Meyer, "Van der Waals interactions and the limits of isolated atom models at interfaces", *Nature Communications* **7**, 11559 (2016).
- ⁸⁰ F. Machali, G. G. Al-Barakati, A. A. El-Sayed, and W. J. Altaf, "The photoelectric cross section of gamma rays in the energy range 43 to 152 keV", *Journal of Physics F: Metal Physics* **17**, 1279–1284 (1987).
- ⁸¹ H. B. Anna Köhler, *Electronic Processes in Organic Semiconductors*, edited by Bässler (Wiley-VCH, 2015).
- ⁸² W. Shockley, "The Theory of p-n Junctions in Semiconductors and p-n Junction Transistors", *Bell System Technical Journal* **28**, 435–489 (1949).
- ⁸³ S. Gun and R. Hattori, "Derivation of Current-Voltage Equation for OLED using Device Simulation", *Researchgate* (2018).

- ⁸⁴ T. W. Christian Reichardt, *Solvents and Solvent Effects in Organic Chemistry (Fourth, Updated and Expanded Edition)*, edited by T. W. Christian Reichardt (Wiley-VCH Verlag GmbH & Co. KGaA, 2010).
- ⁸⁵ K. Fesser, A. R. Bishop, and D. K. Campbell, "Optical absorption from polarons in a model of polyacetylene", *Physical Review B* **27**, 4804–4825 (1983).
- ⁸⁶ M. Reyes-Reyes, I. Cruz-Cruz, and R. Lopez-Sandoval, "Enhancement of the Electrical Conductivity in PEDOT:PSS Films by the Addition of Dimethyl Sulfate", *The Journal of Physical Chemistry C* **114**, 20220–20224 (2010).
- ⁸⁷ J. B. Preinfalk, F. R. Schackmar, T. Lampe, A. Egel, T. D. Schmidt, W. Brütting, G. Gormard, and U. Lemmer, "Tuning the Microcavity of Organic Light Emitting Diodes by Solution Processable Polymer–Nanoparticle Composite Layers", *ACS Applied Materials & Interfaces* **8**, 2666–2672 (2016).
- ⁸⁸ M. Shibata, Y. Sakai, and D. Yokoyama, "Advantages and disadvantages of vacuum-deposited and spin-coated amorphous organic semiconductor films for organic light-emitting diodes", *J. Mater. Chem. C* **3**, 11178–11191 (2015).
- ⁸⁹ J. Frischeisen, "Light extraction in organic light-emitting diodes", PhD thesis (Universität Augsburg, 2011).
- ⁹⁰ B. X. Mi, Z. Q. Gao, M. W. Liu, K. Y. Chan, H. L. Kwong, N. B. Wong, C. S. Lee, L. S. Hung, and S. T. Lee, "New polycyclic aromatic hydrocarbon dopants for red organic electroluminescent devices", *Journal of Materials Chemistry* **12**, 1307–1310 (2002).
- ⁹¹ T. Fukushima and H. Kaji, "Green- and blue-emitting tris(8-hydroxyquinoline) aluminum(III) (Alq3) crystalline polymorphs: Preparation and application to organic light-emitting diodes", *Organic Electronics* **13**, 2985–2990 (2012).
- ⁹² W. Brütting, J. Frischeisen, T. D. Schmidt, B. J. Scholz, and C. Mayr, "Device efficiency of organic light-emitting diodes: Progress by improved light outcoupling", *physica status solidi (a)* **210**, 44–65 (2012).
- ⁹³ M. S. Mehata, Y. Yang, Z.-J. Qu, J.-S. Chen, F.-J. Zhao, and K.-L. Han, "Spin mixed charge transfer states of iridium complex Ir(ppy)₃: transient absorption and time-resolved photoluminescence", *RSC Advances* **5**, 34094–34099 (2015).
- ⁹⁴ B. B. Chen, S. Wang, S. Jiang, Z.-G. Yu, X. Wan, H. F. Ding, and D. Wu, "The role of heavy metal ions on spin transport in organic semiconductors", *New Journal of Physics* **17** (2015).
- ⁹⁵ Y. Zhao and K. Zhu, "Organic–inorganic hybrid lead halide perovskites for optoelectronic and electronic applications", *Chemical Society Reviews* **45**, 655–689 (2016).
- ⁹⁶ B. A. Nejad, S. Gharibzadeh, V. Ahmadi, and H. R. Shahverdi, "Novel Solvent-free Perovskite Deposition in Fabrication of Normal and Inverted Architectures of Perovskite Solar Cells", *Scientific Reports* **6** (2016) 10.1038/srep33649.

-
- ⁹⁷ J. Wang, N. Wang, Y. Jin, J. Si, Z.-K. Tan, H. Du, L. Cheng, X. Dai, S. Bai, H. He, Z. Ye, M. L. Lai, R. H. Friend, and W. Huang, "Interfacial Control Toward Efficient and Low-Voltage Perovskite Light-Emitting Diodes", *Advanced Materials* **27**, 2311–2316 (2015).
- ⁹⁸ Y. Noguchi, Y. Miyazaki, Y. Tanaka, N. Sato, Y. Nakayama, T. D. Schmidt, W. Brütting, and H. Ishii, "Charge accumulation at organic semiconductor interfaces due to a permanent dipole moment and its orientational order in bilayer devices", *Journal of Applied Physics* **111**, 114508 (2012).
- ⁹⁹ L. Jäger, T. D. Schmidt, and W. Brütting, "Manipulation and control of the interfacial polarization in organic light-emitting diodes by dipolar doping", *AIP Advances* **6**, 095220 (2016).
- ¹⁰⁰ X. Zhang, H. Dai, J. Zhao, S. Wang, and X. Sun, "All-solution processed composite hole transport layer for quantum dot light emitting diode", *Thin Solid Films* **603**, 187–192 (2016).
- ¹⁰¹ L. Gao and C. Li, "Preparation and photoluminescence properties of electrospun nanofibers of C60/PVK", *Journal of Luminescence* **130**, 236–239 (2010).
- ¹⁰² TPD's website by sigma-aldrich, <https://www.sigmaaldrich.com/catalog/product/aldrich/443263> (visited on 09/19/2018).
- ¹⁰³ W. R. McCluney, *Introduction to radiometry and photometry*, edited by W. R. McCluney (Artech House, 1994).
- ¹⁰⁴ R. W. Waynant, *Electro-Optics Handbook*, edited by M. N. Ediger (McGraw-Hill, INC, 2000).
- ¹⁰⁵ C. D. Michael Bass, *Handbook of Optics*, edited by E. V. S. Virendra Mahajan, Third, Vol. II Design (Fabricat, 2009).
- ¹⁰⁶ M. S. R. Illuminating Engineering Society of North America, *IESNA Lighting Handbook*, edited by M. S. Rea, 9th ed. (Illuminating Engineering, 2000).
- ¹⁰⁷ J. Mooney and P. Kambhampati, "Get the Basics Right: Jacobian Conversion of Wavelength and Energy Scales for Quantitative Analysis of Emission Spectra", *The Journal of Physical Chemistry Letters* **4**, 3316–3318 (2013).

10 Software References

- S.¹ *Sourcecode of the OLED principle scheme*, (2018) [./data/Other_Sources/BasicOLED/](#).
- S.² *Sourcecode to the CsPbBr₃ crystalstructure*, (2018) [./data/Other_Sources/perov/cspbbr/](#).
- S.³ *Sourcecode to the MaPbI₃ crystalstructure*, (2018) [./data/Other_Sources/perov/mapi/](#).
- S.⁴ *Sourcecode of the absorption comparison scetch*, (2018) [./data/Other_Sources/perovAbsorp/](#).
- S.⁵ *Sourcecode of the PEDOT:PSS chemfig*, (2018) [./data/Other_Sources/chemfig/PEDOTPSSv2.chemfig](#).
- S.⁶ *Sourcecode of the polyTPD chemfig*, (2018) [./data/Other_Sources/chemfig/polyTPD.chemfig](#).
- S.⁷ *Sourcecode of the PVK chemfig*, (2018) [./data/Other_Sources/chemfig/PVK.chemfig](#).
- S.⁸ *Sourcecode of the PMMA chemfig*, (2018) [./data/Other_Sources/chemfig/PMMA.chemfig](#).
- S.⁹ *Sourcecode of the NPB chemfig*, (2018) [./data/Other_Sources/chemfig/NPB.chemfig](#).
- S.¹⁰ *Sourcecode of the mMTDATA chemfig*, (2018) [./data/Other_Sources/chemfig/mMTDATA.chemfig](#).
- S.¹¹ *Sourcecode of the CBP chemfig*, (2018) [./data/Other_Sources/chemfig/CBP.chemfig](#).
- S.¹² *Sourcecode of the Irppy chemfig*, (2018) [./data/Other_Sources/chemfig/Irppy.chemfig](#).
- S.¹³ *Sourcecode of the Alq₃ chemfig*, (2018) [./data/Other_Sources/chemfig/Alq3.chemfig](#).
- S.¹⁴ *Sourcecode of the TPBi chemfig*, (2018) [./data/Other_Sources/chemfig/TPBi.chemfig](#).
- S.¹⁵ *Sourcecode of the BPhen chemfig*, (2018) [./data/Other_Sources/chemfig/BPhen.chemfig](#).
- S.¹⁶ *Sourcecode of the OXD7 chemfig*, (2018) [./data/Other_Sources/chemfig/OXD7.chemfig](#).
- S.¹⁷ *Sourcecode of the OLED Stack Illustration*, (2018) [./data/Other_Sources/Stack/](#).
- S.¹⁸ *Sourcecode of the OLED Bottom View Illustration*, (2018) [./data/Other_Sources/BOTView/](#).
- S.¹⁹ *Sourcecode of the illustration of the Spincoating procedure*, (2018) [./data/Other_Sources/spinCoat/](#).
- S.²⁰ *Sourcecode of the Evaporation process illustration*, (2018) [./data/Other_Sources/evap/](#).
- S.²¹ *Sourcecode of the illustration of the functionality of a profilometer*, (2018) [./data/Other_Sources/profilo/](#).
- S.²² *Sourcecode of the exemplary profilometer plot*, (2018) [./data/20170519_DEKTAK_PEDOT/VII_F_PEDOT_pTPD_40nm-rescale.ipynb](#).
- S.²³ *Sourcecode of the illustration of the functionality of an AFM*, (2018) [./data/Other_Sources/afm/](#).

- S.²⁴ *Sourcecode of the illustration of the functionality of a SEM*, (2018) [./data/Other_Sources/sem/](#).
- S.²⁵ *Sourcecode of the spectroradiometer functionality*, (2018) [./data/Other_Sources/jeti/](#).
- S.²⁶ *Sourcecode of the exemplary spectrum for energy scale wavelength comparison*, (2018) [./data/20180514_LXIII_Irppy/jeti/ShowEnergyScale.ipynb](#).
- S.²⁷ *Chronological Lab Dokumentation*, (2018) [./data/Other_Sources/workingOnPerovskiteOLEDs.pdf](#).
- S.²⁸ *Sourcecode of the PEDOT:PSS AI4083 AFM image gwyddion file*, (2018) [./data/20170906_XXIII_AFM_PEDOT/20170905_XXIII_A_hin.gwy](#).
- S.²⁹ *Sourcecode of the PEDOT:PSS CH8000 AFM image gwyddion file*, (2018) [./data/20170901_XXII_AFM_HIL/20170901_XXII_D_hin.gwy](#).
- S.³⁰ *Sourcecode of the poly TPD AFM image gwyddion file*, (2018) [./data/20170901_XXII_AFM_HIL/20170904_XXII_F_rueck.gwy](#).
- S.³¹ *Sourcecode of the polyTPD on AI4083 AFM image gwyddion file*, (2018) [./data/20170901_XXII_AFM_HIL/20170831_XXII_A_pTPDhin_x_4x4.gwy](#).
- S.³² *Sourcecode of the Alq stack design illustration*, (2018) [./data/20170914_SIMULATION_Alq-NPB/OLEDsSimPlot.ipynb](#).
- S.³³ *Sourcecode of the Alq EL Spectrum*, (2018) [./data/20170630_XVI_JETI_SPECTRA/SpectraPlot.ipynb](#).
- S.³⁴ *Sourcecode of the j-V-L plot of the Alq OLED*, (2018) [./data/20171005_XVII_XV_poly-TPD_compare/OLEDPlot_compare.ipynb](#).
- S.³⁵ *Sourcecode of the OXD7 augmented Alq based stack design illustration*, (2018) [./data/20171116_XXXIV_U-I_OLED/sim/OLEDsSimPlot-alq3emit.ipynb](#).
- S.³⁶ *Sourcecode of the j-V-L plot of the Alq based, OXD7 augmented OLED*, (2018) [./data/20171116_XXXIV_U-I_OLED/OLEDPlot_CustomFileList+compare.ipynb](#).
- S.³⁷ *Sourcecode of the CBP:Irppy3 based stack design illustration*, (2018) [./data/20171204_XXXVIII_I-V_OLED_Irppy/sim/OLEDsSimPlot-Irppy.ipynb](#).
- S.³⁸ *Sourcecode of the Irppy3 EL Spectrum*, (2018) [./data/20171204_XXXVIII_JETI_Irppy/SpectraPlot.ipynb](#).
- S.³⁹ *Sourcecode of the j-V-L plot of the Irppy3 OLED*, (2018) [./data/20171204_XXXVIII_I-V_OLED_Irppy/OLEDPlot_CustomFileList.ipynb](#).
- S.⁴⁰ *Sourcecode of the low concentration MAPbI₃ absorption Spectrum*, (2018) [./data/20171013_XXVII_REFLETOMETRE/ReflectoPlot.ipynb](#).
- S.⁴¹ *Sourcecode of the high concentration MAPbI₃ absorption Spectrum*, (2018) [./data/20171018_XVIII_REFLEKTOMETRY/ReflectoPlot.ipynb](#).

- S.42 *Sourcecode of the MAPbI3 20degC AFM image gwyddion file*, (2018) [./data/20171019_XXIX_AFM_MAPbI3/20180709_XXIX_A.gwy](#).
- S.43 *Sourcecode of the MAPbI3 90degC AFM image gwyddion file*, (2018) [./data/20171019_XXIX_AFM_MAPbI3/20180709_XXIX_B.gwy](#).
- S.44 *Sourcecode of the MAPbI3 20degC on poly-TPD AFM image gwyddion file*, (2018) [./data/20171020_XXX_AFM_MAPbI3/20171020_XXX_B_rueck.gwy](#).
- S.45 *Sourcecode of the MAPbI3 90degC on poly-TPD AFM image gwyddion file*, (2018) [./data/20171020_XXX_AFM_MAPbI3/20171020_XXX_A_hin.gwy](#).
- S.46 *Sourcecode of the MAPbI3 90degC on poly-TPD-PbI2 AFM image gwyddion file*, (2018) [./data/20171020_XXX_AFM_MAPbI3/20171020_XXX_C_rueck.gwy](#).
- S.47 *Sourcecode of the MAPbI3 stack design illustration*, (2018) [./data/20171025_XXXI_U-I_OLED_MAPbI3/sim/OLEDsimPlot.ipynb](#).
- S.48 *Sourcecode of the MAPbI3 EL Spectrum*, (2018) [./data/20171030_XXXI_JETI_MAPbI3_1step/SpectraPlot.ipynb](#).
- S.49 *Sourcecode of the j-V-L plot of the MAPbI3 OLED*, (2018) [./data/20171025_XXXI_U-I_OLED_MAPbI3/OLEDPlot_CustomFileList.ipynb](#).
- S.50 *Sourcecode of the CsPbBr3 on glass slowly spin coated AFM image gwyddion file*, (2018) [./data/20171123_XXXV_AFM/20171122_XXXV_E_rueck_phase.gwy](#).
- S.51 *Sourcecode of the CsPbBr3 on glass AFM image gwyddion file*, (2018) [./data/20171123_XXXV_AFM/20171122_XXXV_F_rueck.gwy](#).
- S.52 *Sourcecode of the CsPbBr3 on poly-TPD AFM image gwyddion file*, (2018) [./data/20180306_XLVIII_AFM_PMMA/XLVIII_A/03060013.gwy](#).
- S.53 *Sourcecode of the CsPbBr3 on PMMA AFM image gwyddion file*, (2018) [./data/20180306_XLVIII_AFM_PMMA/XLVIII_D/0306002A.gwy](#).
- S.54 *Sourcecode of the CsPbBr3 on poly-TPD SEM image*, (2018) [./data/20180306_XLVIII_AFM_PMMA/XLVIII_A/03060013.gwy](#).
- S.55 *Sourcecode of the CsPbBr3 on PMMA SEM image*, (2018) [./data/20180306_XLVIII_AFM_PMMA/XLVIII_D/0306002A.gwy](#).
- S.56 *Sourcecode of the CsPbBr3 on poly-TPD after toluene treatement AFM image gwyddion file*, (2018) [./data/20180306_XLVIII_AFM_PMMA/XLVIII_B/03060023.gwy](#).
- S.57 *Sourcecode of the toluene treated poly-TPD layer AFM images*, (2018) [./data/20170901_XXII_AFM_HIL/20170904_XXII_F_rueck.gwy](#).
- S.58 *Sourcecode of the CsPbBr3 stack design illustration*, (2018) [./data/20180413_LX_PMMA_FINAL/sim/OLEDsimPlot.ipynb](#).
- S.59 *Sourcecode of the CsPbBr3 EL Spectrum*, (2018) [./data/20180406_LVII_HTM-MER+ELECTRONONLY/jeti/SpectraPlot.ipynb](#).

- S.⁶⁰ *Sourcecode of the j-V-L plot of the CsPbBr₃ OLED*, (2018) [./data/20180413_LX_PMMA_FINAL/OLEDPlot_CustomFileList_LX-only2.ipynb](#).
- S.⁶¹ *Sourcecode of the hole-only stack design illustration*, (2018) [./data/20180523_LXIV_holeOnly/sim/OLEDSimPlot.ipynb](#).
- S.⁶² *Sourcecode of the j-V plot of the hole-only device*, (2018) [./data/20180523_LXIV_holeOnly/OLEDPlot_CustomFileList_LX.ipynb](#).
- S.⁶³ *Sourcecode of the j-V-L plot of the CsPbBr₃ with TPBi as ETL OLED*, (2018) [./data/20180227_XLVI_TPBI/OLEDPlot_CustomFileList_XLV-Ca-only.ipynb](#).
- S.⁶⁴ *Sourcecode of the PVK-Irppy3 stack design illustration*, (2018) [./data/20180514_LXIII_Irppy/sim/OLEDSimPlot-Irppy.ipynb](#).
- S.⁶⁵ *Sourcecode of the PVK:Irppy3 EL Spectrum*, (2018) [./data/20180514_LXIII_Irppy/jeti/SpectraPlot.ipynb](#).
- S.⁶⁶ *Sourcecode of the j-V-L plot of the Irppy3 OLED*, (2018) [./data/20180514_LXIII_Irppy/OLEDPlot_CustomFileList_LXI.ipynb](#).
- S.⁶⁷ *Sourcecode of the j-V-L plot of the CsPbBr₃ solved in hexane OLED*, (2018) [./data/20180523_LXV_HEXENE/OLEDPlot_CustomFileList_LX.ipynb](#).
- S.⁶⁸ *Sourcecode of the TPD chemfig*, (2018) [./data/Other_Sources/chemfig/TPD.chemfig](#).
- S.⁶⁹ *Sourcecode of the EL Spectrum with thin poly-TPD*, (2018) [./data/20170630_XVI_JETI_SPECTRA/SpectraPlot_pTPD.ipynb](#).
- S.⁷⁰ *Sourcecode of the MAPbI₃ EL Spectrum*, (2018) [./data/20171030_XXXI_JETI_MAPbI3_1step/SpectraPlot-FakeSpectrum.ipynb](#).
- S.⁷¹ *Sourcecode of the PVK:Irppy3 EL Spectrum with fits*, (2018) [./data/20180514_LXIII_Irppy/jeti/SpectraPlotEnergy.ipynb](#).